

HZDR-072

**CYCLOTRON RESONANCE AND
PHOTOLUMINESCENCE STUDIES
OF DILUTE GaAsN IN MAGNETIC
FIELDS UP TO 62 TESLA**

Faina Eßer

Wissenschaftlich-Technische Berichte
HZDR-072 · ISSN 2191-8708

**WISSENSCHAFTLICH-
TECHNISCHE BERICHTE**

hZDR



**HELMHOLTZ
ZENTRUM DRESDEN
ROSSENDORF**

Wissenschaftlich-Technische Berichte
HZDR-072

Faina Eßer

**CYCLOTRON RESONANCE AND PHOTO-
LUMINESCENCE STUDIES OF DILUTE GaAsN
IN MAGNETIC FIELDS UP TO 62 TESLA**

HZDR

 **HELMHOLTZ**
| ZENTRUM DRESDEN
| ROSSENDORF

Druckausgabe: ISSN 2191-8708

Elektronische Ausgabe: ISSN 2191-8716

Die elektronische Ausgabe erscheint unter Creative Commons License (CC BY 4.0):

<https://www.hzdr.de/publications/Publ-24113>

<urn:nbn:de:bsz:d120-qucosa-210245>

Die vorliegende Arbeit wurde sowohl als Dissertation an der Fakultät Mathematik und Naturwissenschaften der Technischen Universität Dresden sowie als Wissenschaftlich-Technischer Bericht des Helmholtz-Zentrum Dresden – Rossendorf mit der Berichtsnummer **HZDR-072** veröffentlicht.

2016

Herausgegeben vom

Helmholtz-Zentrum Dresden - Rossendorf

Bautzner Landstraße 400

01328 Dresden

Germany

Cyclotron resonance and photoluminescence studies
of dilute GaAsN in magnetic fields up to 62 Tesla

DISSERTATION

zur Erlangung des akademischen Grades
Doctor rerum naturalium (Dr. rer. nat.)

vorgelegt

der Fakultät Mathematik und Naturwissenschaften
der Technischen Universität Dresden

von

Dipl.-Phys. Faina Eßer

geboren am 27.01.1985 in Baku



Die Dissertation wurde im Institut für Ionenstrahlphysik und
Materialforschung am Helmholtz-Zentrum Dresden-Rossendorf (HZDR)
angefertigt.

Eingereicht am: 11.05.2016

Erstgutachter: Prof. Dr. M. Helm,
Technische Universität Dresden &
Helmholtz-Zentrum Dresden-Rossendorf

Zweitgutachter: Prof. Dr. A. Patanè,
School of Physics & Astronomy
The University of Nottingham, UK

Verteidigung: 18.08.2016

Abstract

In this thesis, we investigate optical and electrical properties of dilute nitride semiconductors GaAsN in pulsed magnetic fields up to 62 T. For the most part, the experiments are performed at the Dresden High Magnetic Field Laboratory (HLD).

In the first part of this thesis, the electron effective mass of GaAsN is determined with a direct method for the first time. Cyclotron resonance (CR) absorption spectroscopy is performed in Si-doped GaAsN epilayers with a nitrogen content up to 0.2%. For the CR absorption study, we use the combination of the free-electron laser FELBE and pulsed magnetic fields at the HLD, both located at the Helmholtz-Zentrum Dresden-Rossendorf. A slight increase of the CR electron effective mass with N content is obtained. This result is in excellent agreement with calculations based on the band anticrossing model and the empirical tight-binding method. We also find an increase of the band nonparabolicity with increasing N concentration in agreement with our calculations of the energy dependent momentum effective mass.

In the second part of this thesis, the photoluminescence (PL) characteristics of intrinsic GaAsN and n-doped GaAsN:Si is studied. The PL of intrinsic and very dilute GaAsN is characterized by both GaAs-related transitions and N-induced features. These distinct peaks merge into a broad spectral band of localized excitons (LEs) when the N content is increased. This so-called LE-band exhibits a partially delocalized character because of overlapping exciton wave functions and an efficient interexcitonic population transfer. Merged spectra dominate the PL of all Si-doped GaAsN samples. They have contributions of free and localized excitons and are consequently blue-shifted with respect to LE-bands of intrinsic GaAsN. The highly merged PL profiles of GaAsN:Si are studied systematically for the first time with temperature-dependent time-resolved PL. The PL decay is predominantly monoexponential and has a strong energy dispersion. In comparison to formerly reported values of intrinsic GaAsN epilayers, the determined decay times of GaAsN:Si are reduced by a factor of 10 because of enhanced Shockley-Read-Hall and possibly Auger recombinations.

In the third part of this thesis, intrinsic and Si-doped GaAsN are investigated with magneto-PL in fields up to 62 T. A magneto-PL setup for pulsed magnetic fields of the HLD was built for this purpose. The blue-shift of LE-bands is studied in high magnetic fields in order to investigate its delocalized character. The blue-shift is diminished in intrinsic GaAsN at higher temperatures, which indicates that the interexcitonic

population transfer is only active below a critical temperature $20 \text{ K} < T < 50 \text{ K}$. A similar increase of the temperature has no significant impact on the partially delocalized character of the merged spectral band of GaAsN:Si. We conclude that the interexcitonic transfer of Si-doped GaAsN is more complex than in undoped GaAsN. In order to determine reduced masses of undoped GaAsN and GaAs:Si, the field-induced shift of the free exciton transition is studied in the high-field limit. We find an excellent agreement of GaAs:Si with a formerly published value of intrinsic GaAs which was determined with the same method. In both cases, the reduced mass values are enhanced by 20% in comparison to the accepted reduced mass values of GaAs. The determined GaAsN masses are 1.5 times larger than in GaAs:Si and match the rising trend of formerly reported electron effective masses of GaAsN.

Kurzfassung

Im Rahmen dieser Dissertation werden optische und elektrische Eigenschaften von dem verdünnten Nitrid GaAsN in gepulsten Magnetfeldern bis zu 62 T untersucht. Die meisten Experimente werden im Hochfeld-Magnetlabor Dresden (HLD) durchgeführt.

Im ersten Teil der Dissertation wird die effektive Elektronenmasse von GaAsN zum ersten Mal mit einer direkten Methode bestimmt. Hierfür wird Zyklotronresonanz (ZR) Spektroskopie an GaAsN:Si Proben mit einem Stickstoffgehalt von bis zu 0.2% durchgeführt. Für die Ausführung der Experimente werden zum Teil die Großgeräte Freie-Elektronen Laser FELBE und HLD eingesetzt. Ein leichter Anstieg der ZR Elektronenmasse mit dem Stickstoffgehalt lässt sich beobachten. Dieser Anstieg stimmt hervorragend mit Berechnungen überein, die auf dem Modell des Band Anticrossings oder der empirischen Tight-Binding-Methode basieren. Die Nicht-Parabolizität des Leitungsbandes steigt ebenfalls mit dem Stickstoffgehalt an. Dieses Ergebnis lässt sich durch unsere energieabhängigen Berechnungen der effektiven Masse rekonstruieren.

Im zweiten Teil der Dissertation wird die Photolumineszenz (PL) Charakteristik von intrinsischen und Si-dotierten GaAsN Proben untersucht. Die PL von undotiertem GaAsN mit einem extrem kleinen Stickstoffgehalt weist sowohl GaAs-verwandte Übergänge, als auch typische N-induzierte Beiträge auf. Wenn man den N-Gehalt erhöht, verschmelzen diese einzelnen Peaks jedoch zu einem breiten spektralen Band aus lokalisierten Exzitonen (LE). Dieses sogenannte LE-Band ist teilweise delokalisiert, da die Wellenfunktionen von den betroffenen LEs überlappen, was wiederum einen effizienten Transfer zwischen den einzelnen LEs im Band sicherstellt. Im Falle von Si-dotierten GaAsN Proben wird die PL durchgehend von breiten spektralen Bändern dominiert. Diese beinhalten sowohl Beiträge von freien, als auch von lokalisierten Exzitonen und sind deshalb im Vergleich zu LE-Bändern von intrinsischen Proben blauverschoben. Die spektralen Bänder von GaAsN:Si werden zum ersten Mal systematisch mit temperaturabhängiger, zeitaufgelöster PL untersucht. Die strahlenden Übergänge zerfallen hauptsächlich monoexponentiell und weisen eine hohe Energie-Dispersion auf. Die bestimmten Zerfallszeiten von GaAsN:Si sind 10-mal kleiner als in einer Veröffentlichung von vergleichbaren undotierten GaAsN Proben, was mit einem erhöhtem Aufkommen von Shockley-Read-Hall und möglicherweise auch Auger- Rekombinationen erklärt werden kann.

Im dritten Teil der Dissertation werden PL Untersuchungen, die an intrinsischen und Si-dotierten GaAsN Proben in Magnetfeldern bis zu 62 T durchgeführt wurden, vorgestellt. Hierfür wurde eine neue Experimentier Vorrichtung für PL Untersuchungen in gepulsten Magnetfeldern des HLD gebaut. Mit dieser Methode wird u.a. die Blauverschiebung von LE-Bändern in verschiedenen GaAsN Proben bei variierenden Temperaturen untersucht, um den Ursprung ihres delokalisierten Verhaltens besser zu verstehen. Intrinsische GaAsN Proben weisen eine verringerte Blauverschiebung bei höheren Temperaturen auf. Dies deutet darauf hin, dass der exzitonische Transfer nur unterhalb einer kritischen Temperatur $20\text{ K} < T < 50\text{ K}$ funktioniert. Im Gegensatz dazu weist die Blauverschiebung von der GaAsN:Si PL keine Temperaturabhängigkeit auf. Vermutlich ist ein komplizierterer exzitonischer Transfer, als bei undotiertem GaAsN, für dieses Verhalten verantwortlich. Die Magnetfeld-induzierte Verschiebung des freien Exzitons wird im Grenzfall von sehr hohen Feldern untersucht, um die reduzierte Masse von intrinsischen GaAsN und GaAs:Si zu bestimmen. Im Fall von GaAs:Si findet man eine sehr gute Übereinstimmung mit der bereits publizierten (selbe Untersuchungsmethode) reduzierten Masse von undotiertem GaAs. Jedoch liegen beide Ergebnisse 20% über dem bekannten Wert von GaAs. Die reduzierten Massen von GaAsN sind 1.5-mal so groß wie in der Referenzprobe. Dieses Ergebnis stimmt gut mit dem Anstiegstrend der effektiven Elektronenmassen von bereits publizierten Werten überein.

Contents

Abstract	iii
Kurzfassung	v
1. Introduction	1
2. Fundamentals	5
2.1. Semiconductor alloys	6
2.2. Isoelectronic impurities and traps	7
2.2.1. Virtual Crystal Approximation	7
2.2.2. Nitrogen in III-V semiconductors	8
2.3. Band anticrossing model	9
2.3.1. BAC described by the many-impurity Anderson model	10
2.3.2. BAC momentum effective mass	12
2.4. Empirical pseudopotential method	15
2.4.1. Calculation procedure	15
2.4.2. Electronic structure in the dilute regime	17
2.4.3. Evolution of electronic structure with N composition	17
2.5. Linear combination of isolated nitrogen states method	18
2.5.1. Isolated nitrogen and cluster states	18
2.5.2. LCINS electron effective mass	20
2.6. Fundamentals of cyclotron resonance	21
2.6.1. Classical cyclotron resonance: Drude model	22
2.6.2. Landau level quantization	24
3. Spectroscopic methods	25
3.1. Cyclotron resonance spectroscopy	25
3.1.1. High magnetic field generation	26

3.1.2.	Free-electron laser	28
3.1.3.	Quantum cascade laser	30
3.1.4.	Design of the experimental setup	32
3.2.	Time-resolved photoluminescence	35
3.2.1.	Experimental setup with a streak camera	36
3.2.2.	Laser system	37
3.3.	Magneto-photoluminescence in pulsed magnetic fields	39
3.3.1.	Experimental setup	39
3.3.2.	Measuring technique	42
4.	Direct determination of the electron effective mass of GaAsN	45
4.1.	Review of former results	45
4.2.	Electron effective mass determination	47
4.2.1.	Cyclotron resonance, impurity-shifted cyclotron resonance and the impact of artifacts	48
4.2.2.	THz CR absorption spectroscopy in GaAsN	49
4.3.	Energy dependence of the effective mass	51
4.3.1.	Reststrahlen effect in GaAs and GaAsN	51
4.3.2.	CR spectroscopy with different photon energies	52
4.3.3.	Increase of the electron effective mass and band nonparabolicity with N content	53
4.4.	Mobility drop with increasing N content	55
4.5.	Discussion and summary	56
5.	Photoluminescence study of GaAsN and GaAsN:Si	59
5.1.	Photoluminescence spectroscopy	59
5.1.1.	Luminescence processes in crystalline semiconductors	60
5.1.2.	Photoluminescence of gallium arsenide	61
5.2.	Radiative recombination in GaAsN alloys	63
5.2.1.	Radiative recombinations of GaAs _{1-x} N _x with $x = 0.095\%$	64
5.2.2.	PL evolution with increasing N content	69
5.3.	Luminescence of silicon-doped GaAsN	72
5.3.1.	Recombination processes in GaAsN:Si	73
5.3.2.	Discussion: LE-bands in GaAsN:Si	77

5.4.	Recombination dynamics in GaAsN:Si	78
5.4.1.	Dispersion of PL decay times	80
5.4.2.	Impact of nitrogen on the PL decay times of GaAsN:Si	82
5.5.	Summary and outlook	84
6.	Photoluminescence study of GaAsN and GaAsN:Si in high magnetic fields	87
6.1.	LE-bands in high magnetic fields	87
6.1.1.	Magneto-photoluminescence of intrinsic GaAsN	88
6.1.2.	Interexcitonic population transfer and the impact of a higher thermal energy	90
6.1.3.	Magneto-PL of GaAsN:Si	92
6.1.4.	Discussion on the interexcitonic transfer mechanism	94
6.2.	Determination of the reduced effective mass of GaAsN via magneto-PL	97
6.2.1.	Landau level approximation	97
6.2.2.	Reduced mass of GaAsN with low N content	99
6.3.	Summary and outlook	101
7.	Conclusions and outlook	103
A.	Appendix	107
A.1.	Overview of the investigated samples	107
A.2.	Experimental parameters for magneto-PL in the HLD	108
A.3.	Detailed drawings for the magneto-PL probe	109
	Bibliography	121
	List of figures	139
	List of tables	143
	Publications	145
	Acknowledgments	149

1. Introduction

The steep increase in digital interconnectivity during the last three decades has fundamentally changed our way of life. To this day, the development of communication technology continues to grow exponentially. The challenges of making new ways of data transfer accessible to the public have always been to make it as reliable, fast, efficient and affordable as possible. It was realized at an early stage that fiber-optic communication is the key to a successful implementation of these requirements. Still, a lot of effort had to be put into the fiber technology in order to reach an adequate propagation rate. It is obvious that semiconductor devices are the primary choice for signal generation and transmission in terms of size, efficiency, cost and temporal stability. The heterostructure indium gallium arsenide phosphide (InGaAsP) on indium phosphide (InP) emits inter alia at $1.3\ \mu\text{m}$ and $1.57\ \mu\text{m}$ [167, 65, 153], which correspond to the telecommunication regions. These wavelengths are most suited for information transfer with conventional optical fibers, because of their minimal damping and dispersion in comparison to other regions of the electromagnetic spectrum. Thus, InGaAsP/InP represents the most common system for telecommunication purposes [4]. Nevertheless, other semiconductor devices in the $1.6\ \mu\text{m}$ range are highly desirable. Especially lasers grown on a gallium arsenide (GaAs) substrate have several advantages compared with InP. The well-established growth of GaAs based systems results in a better fabrication performance. This can be achieved with approximately 1.5 times larger [4] substrates of GaAs in comparison to InP. Furthermore, a better electron confinement can be realized in GaAs based heterostructures, such as InGaAs/GaAs, because of an increased band offset compared to that of InP with quaternary alloys [81, 4]. This is particularly valid at high temperatures and can tremendously improve the temperature stability of a GaAs-based laser system and increase its maximum operating temperature [81]. At the same time, GaAs/AlAs Bragg mirrors can be monolithically grown on an InGaAs based active layer, which is only possible in InP with great difficulty [23]. All in all, the realization of a

GaAs-based laser system would be greatly beneficial for telecommunication purposes.

Indeed, strained InGaAs quantum well lasers were established for an emission around 1 μm [86, 87]. In order to reach the telecommunication region at 1.3 μm and beyond, a bigger indium content is required. This is accompanied by an increased lattice mismatch, which reaches an unacceptable level for 1.3 μm [33, 104]. A different approach had to be found. In fact, Weyers et al. showed 1992 that the band gap of GaAs can be efficiently reduced by the incorporation of a small fraction of nitrogen (N) [162] into the system. A decrease of about 0.2 eV per atomic percentage of N was observed. The potential for telecommunication applications of dilute nitrides like (In)GaAsN was rapidly recognized and led to a new active research area in semiconductor physics. The first $\text{In}_y\text{Ga}_{1-y}\text{As}_{1-x}\text{N}_x$ -based laser with an emission wavelength of 1.3 μm was demonstrated in 2000 by Livshits et al. [96]. Vertical cavity surface emitting lasers [148, 132] and edge-emitting devices [8, 9] for 1.5 μm were presented in subsequent years.

Besides their technological potential, dilute nitrides turned out to be very interesting from a fundamental point of view. They are built by inserting nitrogen into the group V sublattice of conventional III-V semiconductors such as GaAs, GaP or InGaAs. GaAsN is the main representative of the dilute nitride material family. In addition to the rapid band gap reduction with increasing N content, GaAsN has other unusual properties. A reduced pressure and temperature dependence of the band gap [122, 136, 77, 129], inhomogeneous broadening of radiative transitions [128, 129], a large Stokes shift between absorption and emission [26, 28] and localization effects in the carrier transport [85, 151, 129] were found in this system. A detailed overview is provided in Refs. [25, 58, 44]. Among many interesting results, the investigation of the electron effective mass m^* of GaAsN resulted in some controversial findings. Different experimental techniques have been applied to the system, including a variety of indirect approaches such as magneto-photoluminescence [101], optically detected cyclotron resonance [55], transport [169], electroreflectance [83] or Raman scattering [64]. A slow rise of the electron effective mass with nitrogen content [142] was found in addition to results indicating a steep increase of the mass followed by a decrease [2], alternating mass behavior [101] or even a decrease of the mass with N content [169]. However, no direct method to determine m^* has ever been applied on GaAsN. Nevertheless, the knowledge of the electron effective mass is essential from both the fundamental and application-related points of view. The same applies to a profound

understanding of different luminescence peaks of GaAsN and to its recombination dynamics. Especially n-doped GaAsN has rarely been in the focus of investigations. Since doping is essential for potential applications, it is very interesting to analyze the complex recombination dynamics of Si-doped material and study the impact of silicon. The same is valid for the population transfer of localized excitons in high magnetic fields. Especially the influence of a higher thermal energy on the interexcitonic transfer mechanism has never been investigated before. Consequently, a clarification of the mentioned issues in GaAsN is highly desirable.

The purpose of this thesis is a detailed magneto-optical study of GaAsN in high magnetic fields. Before going into details on the experimental results, an overview of the main theoretical models for GaAsN is provided in Chap. 2. A unique experimental configuration is available in order to apply the most direct method for effective mass determination and is presented in Chap. 3. It involves the intense, widely tunable, quasi-continuous terahertz (THz) free-electron laser FELBE and pulsed magnetic fields up to 62 T of the Dresden High Magnetic Field Laboratory (HLD). The combination of these two large-scale facilities is unique in Europe and located in the Helmholtz-Zentrum Dresden-Rossendorf. Another part of this work was to build an experimental setup for magneto-photoluminescence measurements in pulsed magnetic fields at the HLD. This task included the development of a measuring probe suitable for HLD pulsed magnets and the establishment of an appropriate measuring technique. Both are presented in Chap. 3 along other spectroscopic tools. Experimental results are divided into three main chapters. Chap. 4 is dedicated to the determination of the electron effective mass in GaAsN with terahertz cyclotron resonance absorption spectroscopy. The electron effective mass is studied in $\text{GaAs}_{1-x}\text{N}_x$ samples with different nitrogen contents at various photon energies. The experimental results are compared with calculations based on the band anticrossing model. Furthermore, electron mobilities are analyzed and compared with Hall mobilities and theoretical predictions. Si-doped and Si-free GaAsN epilayers are also investigated with continuous-wave photoluminescence, as shown in Chap. 5. The origin of distinct peaks is studied in samples with different N contents using temperature and power series. The impact of silicon is in the focus. For the first time, the recombination dynamics is systematically analyzed in silicon n-doped GaAsN with time-resolved photoluminescence at different temperatures. Chap. 6 contains our magneto-photoluminescence study of GaAsN and GaAsN:Si in magnetic fields up to 62 T. Si-doped GaAsN samples are analyzed

with magneto-photoluminescence for the first time. Another new contribution is the investigation of the population transfer of localized excitons in magnetic fields and their behavior at higher temperatures. In the last section, the electron effective mass is analyzed via magneto-photoluminescence with a field-induced blue-shift of free excitons.

2. Fundamentals

The research activity on dilute nitrides and in particular $\text{GaAs}_{1-x}\text{N}_x$ has increased significantly after the discovery of the band gap reduction of GaAs with the incorporation of a small fraction of nitrogen by Weyers et al. [162, 56]. Nitrogen introduces an impurity level ≈ 0.2 eV above the conduction band (CB) minimum of GaAs [164, 95, 120] in the ultra-dilute regime ($x \leq 0.01\%$). Higher N contents strongly disturb the GaAs lattice because of the electronegativity difference between As and N and consequently affect the electronic structure [120]. This chapter provides an overview of the most important theoretical models which have been proposed to describe this material system and presents further fundamental knowledge. The band anticrossing model [136] is very instructive in order to explain the band gap reduction of dilute nitrides. The interaction of the N impurity with the lowest CB of GaAs causes it to split into two subbands E_{\pm} within the context of the band anticrossing model. The separation between these subbands can be further influenced by the nitrogen content. The observed gap reduction of about 0.1 eV per atomic percentage of N [120] is explained within this model. Other unusual properties such as a reduced pressure and temperature dependence of the band gap [122, 136, 77, 129], inhomogeneous broadening of radiative transitions [128, 129], a large Stokes shift between absorption and emission [26, 28] and localization effects in the carrier transport [85, 151, 129] were found in this system. These observations can be described inter alia with models based on pseudopotential [14, 105, 74], first-principles [69, 160, 15] and modified $k \cdot p$ calculations [115, 94], some of which are presented in this chapter.

A broad introduction to semiconductor alloys is provided in the first section. Isoelectronic impurities and traps are discussed in the second section. They are treated within the virtual crystal approximation, which fails in case of the isoelectronic trap nitrogen. The most established models for GaAsN-like systems are introduced subsequently. The third section addresses the band anticrossing model. The empirical pseudopotential method is in the focus of the fourth section. Section five provides an

overview of the linear combination of isolated nitrogen states method. The electron effective mass is discussed in the framework of the band anticrossing model and the linear combination of isolated nitrogen states method. The fundamentals of cyclotron resonance spectroscopy are demonstrated in section six.

2.1. Semiconductor alloys

Semiconductor alloys are used to tune the material properties of elemental semiconductors and to optimize and to widen their application as devices [1]. Compound semiconductors are classified as binary (e.g. GaAs), ternary (e.g. InGaAs), quaternary (e.g. InGaAsP) and pentanary (e.g. AlGaInAsSb) alloys [1] with a large variety.

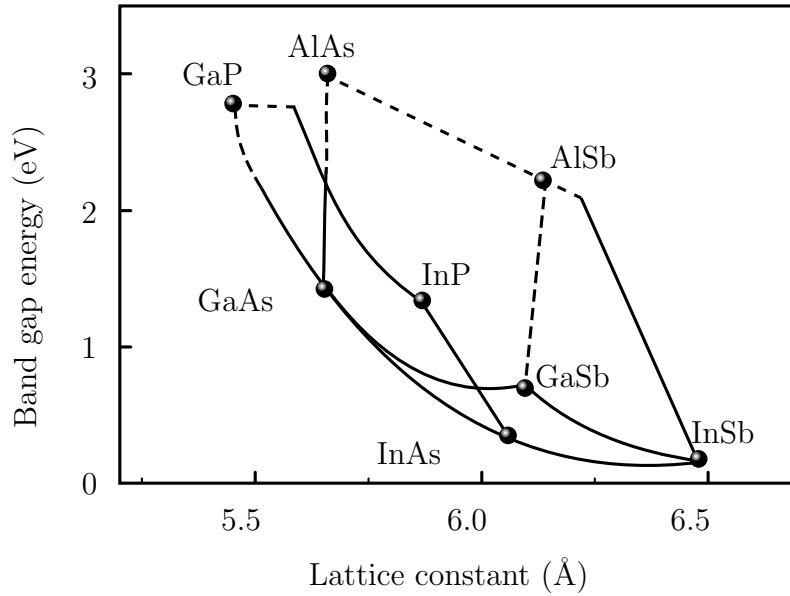


Figure 2.1.: Relationship between band gap energy and lattice parameter at 300 K for common III-V semiconductor alloys. Solid (dashed) curves represent direct (indirect) gaps. The values are adapted from the Landolt-Börnstein database [88, 12].

Optical and electronic properties are determined by the band gap of the resulting system and lattice matching is essential for band gap engineering. Fig. 2.1 illustrates the relationship between the band gap energy and lattice constant of common III–V alloys at 300 K.

2.2. Isoelectronic impurities and traps

Ternary alloys (e.g. InGaAs) emerge from binary alloys (e.g. GaAs) by replacing a few binary atoms of one kind (e.g. Ga) with a different species (e.g. In) with similar properties. Usually, the substituting atoms have the same number of valence electrons. Indium, aluminum or phosphorus are the most common representatives of these so-called isoelectronic impurities. The size of these atoms is similar to the size of the atoms they replace [152, 90]. Fig. 2.2 (a) shows the atom arrangement of $\text{In}_x\text{Ga}_{1-x}\text{As}$.

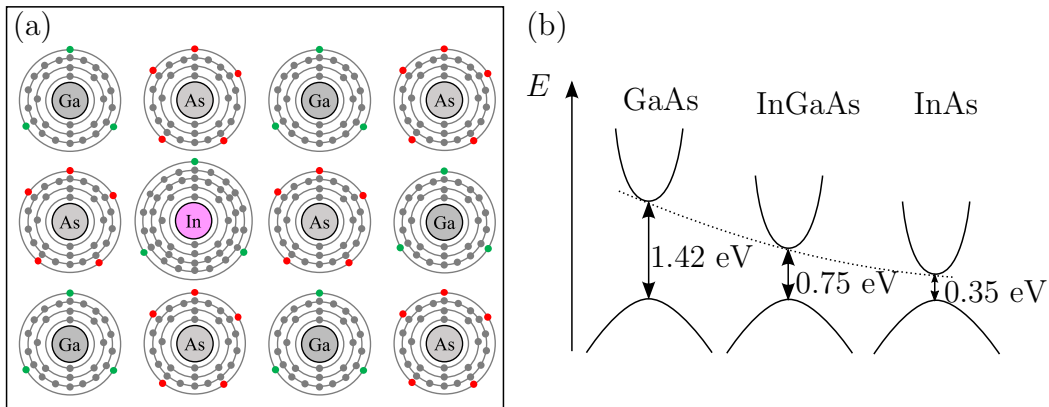


Figure 2.2.: (a) Simplified crystal structure of InGaAs. The isoelectronic impurity In has a similar size as Ga. (b) The band gap of the ternary alloy $\text{In}_{0.53}\text{Ga}_{0.47}\text{As}$ lies between GaAs and InAs. The small band gap bowing is symbolized with the dashed line.

Indium is the isoelectronic impurity and substitutes for gallium. In general, InGaAs crystallizes in zinc blende structure. The oversimplified 2D-representation only illustrates bonding partners and radii between lattice atoms. Obviously, the lattice is not crucially distorted by indium. Still, isoelectronic impurities break the translational symmetry of the host by introducing non-periodic impurity potentials.

2.2.1. Virtual Crystal Approximation

In most cases, the translational invariance is restored by the virtual crystal approximation approach [113, 107]. The impurity potentials V_A, V_B, V_C of the new alloy $\text{A}_x\text{B}_{1-x}\text{C}$ can be approximated by an average potential

$$\langle V \rangle = xV_A + (1-x)V_B + V_C, \quad (2.1)$$

weighted by the isoelectronic impurity concentration x [12]. Within the restored symmetry perspective, properties of endpoint materials are described as a linear combination of the binary compound's properties AB and AC. In particular the band gap

$$E_g^{ABC}(x) = (1 - x) \cdot E_g^{BC} + x \cdot E_g^{AC} - b \cdot x \cdot (1 - x) \quad (2.2)$$

can be determined via virtual crystal approximation by taking into account a small quadratic bowing term $b \leq 1$ eV. The band gap of $\text{In}_x\text{Ga}_{1-x}\text{As}$ decreases with increasing indium content x from GaAs towards InAs as shown in Fig. 2.2 (b) in line with virtual crystal approximation predictions.

2.2.2. Nitrogen in III-V semiconductors

Structural differences between the compounds AB and AC, and in particular size differences between B and C, can drastically increase the bowing parameter. This applies to all III-N-V systems. The isoelectronic impurity nitrogen has a significantly

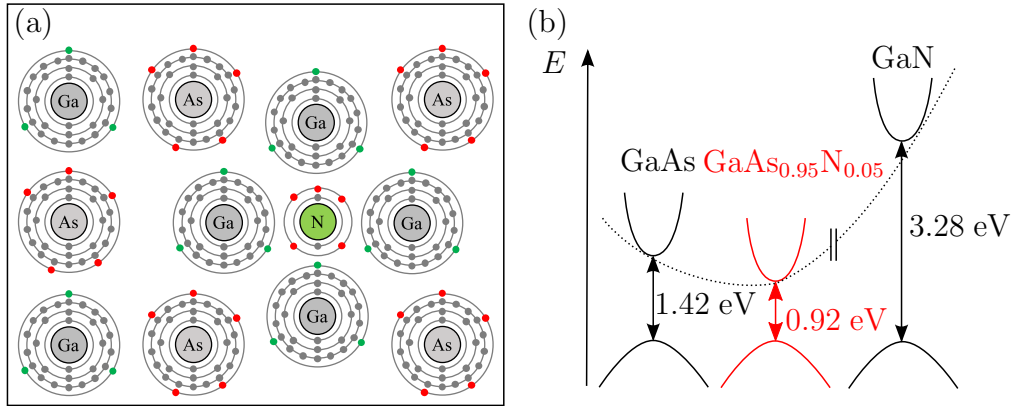


Figure 2.3.: (a) Simplified crystal structure of GaAsN. The isoelectronic trap nitrogen distorts the system. (b) The band gaps of GaAs, GaAs_{0.95}N_{0.05} and GaN are shown. GaAsN has a smaller band gap than both GaAs and GaN. This results in a huge band gap bowing, symbolized by the dashed curve.

smaller size than other group V elements. Especially in case of GaAsN the size difference leads to a greater lattice distortion, as can be seen in Fig. 2.3 (a). Distortion results in a number of unusual effects, including a huge band gap bowing $b \approx 20$ eV [18], a drop in the electron mobility [110], a reduced pressure dependence [136], etc.

Fig. 2.3 (b) illustrates the surprising band gap reduction and huge band gap bowing of $\text{GaAs}_{0.95}\text{N}_{0.05}$. Consequently, the virtual crystal approximation cannot be applied to GaAsN.

2.3. Band anticrossing model

A simple but effective two-level band anticrossing (BAC) model was developed by Shan and coworkers for GaInNAs in 1999 [136, 137]. According to this model, nitrogen introduces localized states E^d into the system GaInAs, which interact with extended CB states $E_k^c(k)$ of the host. This interaction causes a splitting of the CB into two subbands $E_{\pm}(k)$. Experimental evidence of this splitting was obtained by photomodulation spectroscopy in combination with large hydrostatic pressure [136]. These bands have an enhanced localization character because of the observed

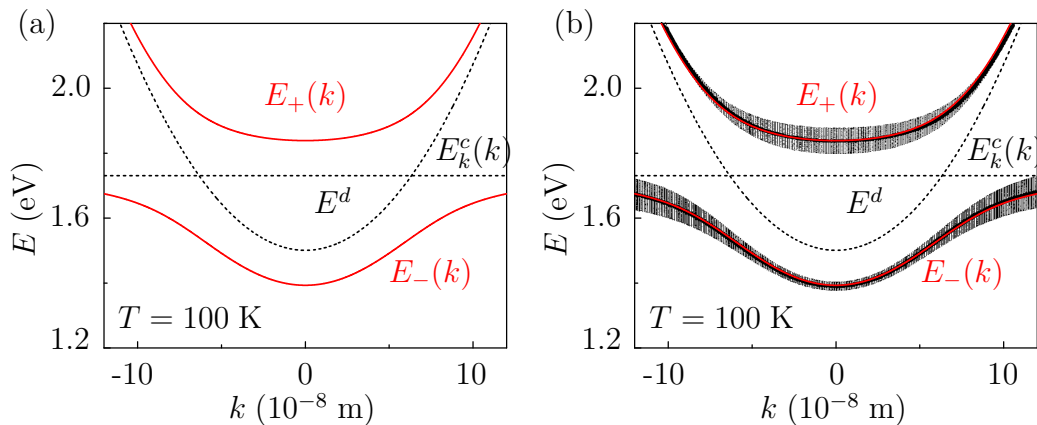


Figure 2.4.: Conduction bands $E_{\pm}(k)$ of $\text{GaAs}_{0.995}\text{N}_{0.005}$ for $V = 2.7$ eV. We use Eq. (2.7) for the BAC [136] dispersion in (a) and adapted (b) from Ref. [166], which corresponds to Eq. (2.8) with $\Gamma_d \neq 0$. The broadening of the line thickness denotes a smearing of the energy state, defined in Eq. (2.9). All energies are referenced to the top of the valence band of GaAs.

saturation of their energy blue-shift at high pressures [136]. Fig. 2.4 (a) schematically illustrates the band splitting. The BAC model explains the N-induced red-shift of the fundamental band gap and its pressure dependence. It can be deduced by means of the many-impurity Anderson model, as shown in Sec. 2.3.1. The applicability of the BAC was shown later for other III-N-V [138, 165] and II-VI [158] systems.

2.3.1. BAC described by the many-impurity Anderson model

Using the many-impurity Anderson model, the simple two-level BAC model [136, 137] is put on a firmer theoretical base [166]. The Anderson model was originally proposed to describe a single impurity atom of a transition metal or rare earth element in a nonmagnetic material [5]. The extended many-impurity Anderson model was used to calculate the electronic structure of semiconductor alloys with deep transition-metal impurities [79, 67]. It has been widely applied afterwards to treat interactions between localized and extended states. In this model, the electron system is separated into two groups. Electrons from extended host states belong to the first one and localized electrons from randomly distributed impurity levels belong to the second one. Their interaction leads to the Hamiltonian [166]

$$H = \sum_{\mathbf{k}} E_{\mathbf{k}}^c c_{\mathbf{k}}^\dagger c_{\mathbf{k}} + \sum_{\mathbf{j}} E_{\mathbf{j}}^d d_{\mathbf{j}}^\dagger d_{\mathbf{j}} + \frac{1}{\sqrt{N}} \sum_{\mathbf{j}, \mathbf{k}} \left(e^{i\mathbf{k} \cdot \mathbf{j}} V_{\mathbf{kj}} c_{\mathbf{k}}^\dagger d_{\mathbf{j}} + \text{h.c.} \right) \quad (2.3)$$

in case of a highly mismatched alloy [79, 67]. The first term describes CB electrons with an energy dispersion $E_{\mathbf{k}}^c$. The second term represents localized electrons on the \mathbf{j} th impurity site with an energy $E_{\mathbf{j}}^d$. $c^\dagger(c)$ and $d^\dagger(d)$ correspond to the conduction electron and impurity electron creation (annihilation) operator, respectively. The third term is an interaction term and takes care of the dynamic mixing between band states and localized states. The hybridization strength is characterized by the parameter [166]

$$V_{\mathbf{kj}} = \sum_{\mathbf{l}} e^{i\mathbf{k} \cdot (\mathbf{l} - \mathbf{j})} \int a^*(\mathbf{r} - \mathbf{l}) H_{\text{HF}}(\mathbf{r}) \varphi_d(\mathbf{r} - \mathbf{j}) d\mathbf{r}, \quad (2.4)$$

with Wannier functions $a(\mathbf{r} - \mathbf{j})$ and $\varphi_d(\mathbf{r} - \mathbf{j})$, which belong to the band and the impurity, respectively. $H_{\text{HF}}(\mathbf{r})$ is the energy of a single electron in Hartree-Fock approximation [5]. The Hamiltonian (2.3) can be solved for a single impurity [5]. The more general case of a dilute and finite nitrogen concentration $0 < x \leq 1$ requires a different approach. It is impossible to directly calculate eigenvalues and eigenstates of an imperfect crystal without translational symmetry [43]. The formalism of the thermodynamic Green's function gives access to important quantities without the necessity of a complete normal model solution [43]. Wu et al. [166] used the single-site coherent-potential approximation for configurational averaging. This approach can be

applied because of the random distribution of localization centers and thus negligible correlations between impurity positions [168, 43, 166]. The average Green's function partially restores the translational invariance, and thus \mathbf{k} as a good quantum number [166]. The diagonal Green's function in the coherent-potential approximation can be written as [79, 168, 43, 166]

$$G_{\mathbf{k}\mathbf{k}}(E) = \left[E - E_{\mathbf{k}}^c - \frac{V^2 x}{E - E^d - i\pi\beta V^2 \rho_0(E^d)} \right]^{-1}. \quad (2.5)$$

The energy dispersion is determined by the poles of $G_{\mathbf{k}\mathbf{k}}(E)$ in Eq. (2.5)

$$\begin{vmatrix} E_{\mathbf{k}}^c - E(\mathbf{k}) & V\sqrt{x} \\ V\sqrt{x} & E^d + i\Gamma_d - E(\mathbf{k}) \end{vmatrix} = 0, \quad (2.6)$$

which corresponds to the two-level BAC eigenvalue problem [136] with an additional broadening $\Gamma_d = \pi\beta V^2 \rho_0(E^d)$ of the energy E^d [166]. The unperturbed density of states is symbolized by ρ_0 , β is a prefactor and V is the value of $V_{\mathbf{k}\mathbf{j}}$ averaged over \mathbf{k} and \mathbf{j} . Analogous to Ref. [136], the two solutions of this problem are reduced to

$$E_{\pm}(\mathbf{k}) = \frac{1}{2} \left[(E_{\mathbf{k}}^c + E^d) \pm \sqrt{(E_{\mathbf{k}}^c - E^d)^2 + 4V^2 x} \right] \quad (2.7)$$

for $\Gamma_d = 0$ [166]. In case of a small broadening Γ_d , the analytical solution of Eq. (2.6) can be approximated using $2V\sqrt{x} \gg \pi\beta V^2 \rho_0(E^d)$ and $|E_{\mathbf{k}}^c - E^d| \gg \pi\beta V^2 \rho_0(E^d)$ as [166]

$$\tilde{E}_{\pm}(\mathbf{k}) \approx E_{\pm}(\mathbf{k}) + i\Gamma_d \frac{[E_{\pm}(\mathbf{k}) - E_{\mathbf{k}}^c]}{[E_{\pm}(\mathbf{k}) - E_{\mathbf{k}}^c] + [E_{\pm}(\mathbf{k}) - E^d]} \equiv E_{\pm}(\mathbf{k}) + i\Gamma_{\pm}(\mathbf{k}) \quad (2.8)$$

and is shown in Fig. 2.4 (b). The dispersion relation is thus equivalent to the two-level BAC dispersion [136] with an additional imaginary part, which defines the hybridization-induced uncertainty of the energy [166]. This imaginary part

$$\Gamma_{\pm}(k) = |\langle \varphi_d | E_{\pm}(\mathbf{k}) \rangle|^2 \Gamma_d \quad (2.9)$$

is proportional to the admixture of localized states with restructured wave functions in the two-state-like-perturbation picture, described by Eq. (2.6) [166].

2.3.2. BAC momentum effective mass

The direct determination of the electron effective mass of GaAsN is a major part of this work. The BAC electron effective mass m_{BAC}^* is introduced in this section. In the first part, a very general and energy dependent electron effective mass is deduced for isotropic crystals like GaAs and GaAsN. The BAC model is used in the second part in order to determine the impact of nitrogen on the electron effective mass in GaAsN.

Momentum effective mass

The effective mass is conventionally described by Eq. (2.21) with the second derivative of the carrier energy $E(k)$. However, a different expression is more relevant for transport phenomena and can be defined in terms of the susceptibility. Following this approach [147], the susceptibility is derived from the Boltzmann equation first. Its solution is given by [48, 147]

$$j_x = -\frac{2}{(2\pi)^3} \frac{e^2}{\hbar} \left(E_x \int \frac{\tau v_x}{1 + (\omega\tau)^2} \frac{\partial f_0}{\partial k_x} d\Omega_k - \frac{\partial E_x}{\partial t} \int \frac{\tau^2 v_x}{1 + (\omega\tau)^2} \frac{\partial f_0}{\partial k_x} d\Omega_k \right) \quad (2.10)$$

for crystal electrons in a variable electrical field $E_x = E_0 e^{i\omega t}$. As usual, \hbar and τ identify the Planck constant and the relaxation time, respectively. v_x is the electron velocity, f_0 is the occupation probability and $d\Omega_k = dk_x dk_y dk_z$ is a volume element. Generally, the current density can be expressed in the form

$$\begin{aligned} j_x &= \sigma E_x + i\varepsilon_0 \omega \chi_c E_x \\ &= \sigma E_x + \varepsilon_0 \chi_c \frac{\partial E_x}{\partial t}, \end{aligned} \quad (2.11)$$

with the conductivity σ , the vacuum permittivity ε_0 and the electric susceptibility χ_c . Eq. (2.11) is justified by the considered isotropic dispersion relation. Using Eq. (2.10) and Eq. (2.11), one obtains a suitable expression for the susceptibility

$$\chi_c = \frac{2}{(2\pi)^3} \frac{e^2}{\varepsilon_0 \hbar} \int \frac{\tau^2 v_x}{1 + (\omega\tau)^2} \frac{\partial f_0}{\partial k_x} d\Omega_k. \quad (2.12)$$

In the following, the high-frequency limit $\omega\tau \gg 1$ is discussed, which applies to semiconductors and dielectric materials in the visible to mid-infrared range. In these

cases, the susceptibility

$$\chi_c = \frac{2}{(2\pi)^3} \frac{e^2}{\varepsilon_0 \hbar \omega^2} \int v_x \frac{\partial f_0}{\partial k_x} d\Omega_k \quad (2.13)$$

is independent of τ and only characterized by the structure of the energy band. Using $\hbar v_x = \partial E(k)/\partial k_x$ and $v_x^2 = 1/3v^2$, Eq. (2.13) simplifies to

$$\chi_c = \frac{2}{(2\pi)^3} \frac{e^2}{3\varepsilon_0 \omega^2} \int v^2 \frac{\partial f_0}{\partial E(k)} d\Omega_k. \quad (2.14)$$

Furthermore, the volume integral can be replaced by a surface integral with

$$d\Omega_k = \left[\frac{dS_k(E)}{\nabla_k E} \right] dE. \quad (2.15)$$

$S_k(E)$ is a surface of constant energy in k -space. The susceptibility of an isotropic crystal is then defined by the spherical Fermi surface $S_k(E_F) = 4\pi k_F^2$ of the Fermi energy E_F with

$$\chi_c = -\frac{2}{(2\pi)^3} \frac{e^2}{3\varepsilon_0 \hbar \omega^2} v_F S_k(E_F). \quad (2.16)$$

Making use of the carrier concentration $N = \frac{2}{(2\pi)^3} \cdot \frac{4}{3} \pi k_F^3$ and $\hbar v_F = |\partial E/\partial k|_{E_F}$, Eq. (2.16) simplifies to

$$\chi_c = -\frac{N e^2}{k_F \varepsilon_0 \hbar^2 \omega^2} \left| \frac{\partial E}{\partial k} \right|_{E_F}. \quad (2.17)$$

The susceptibility of a free electron gas

$$\chi_c = -\frac{\omega_p^2}{\omega^2} = \frac{N e^2}{\varepsilon_0 m^* \omega^2}, \quad (2.18)$$

is defined by the plasma frequency $\omega_p = \sqrt{\frac{N e^2}{\varepsilon_0 m^*}}$ in the high-frequency limit $\omega \tau \gg 1$. Comparing Eq. (2.17) with Eq. (2.18) gives a definition for the electron effective mass

$$\frac{1}{m^*} = \frac{1}{\hbar^2 k_F} \left| \frac{\partial E(k)}{\partial k} \right|_{E_F} \quad (2.19)$$

of isotropic crystals like GaAs and GaAsN. In analogy to Ref. [170], I will refer to it as momentum effective mass. In case of a parabolic energy dispersion

$$E(k) = \frac{\hbar^2 k^2}{2\tilde{m}^*}, \quad (2.20)$$

one gets $\partial E(k)/\partial k = \hbar^2 k/\tilde{m}^*$. Inserting this expression into Eq. (2.19) yields $\tilde{m}^* = m^*$, and the electron effective mass is naturally defined as

$$\frac{1}{\tilde{m}^*} = \frac{1}{\hbar^2} \frac{\partial^2 E(k)}{\partial k^2}. \quad (2.21)$$

Eq. (2.21) is the most prominent definition of the effective mass and is equivalent to Eq. (2.19) in the parabolic case. However, Eq. (2.19) is more relevant for transport phenomena. Consequently, we will use the momentum effective mass (2.19) in the following approach.

BAC electron effective mass

In order to describe the behavior of the electron effective mass in dependence of the nitrogen content in the BAC model, we use the momentum effective mass (2.19) and the energy dispersion of the lowest CB $E_-(k)$ from Eq. (2.7) for $k = 0$. In this case,

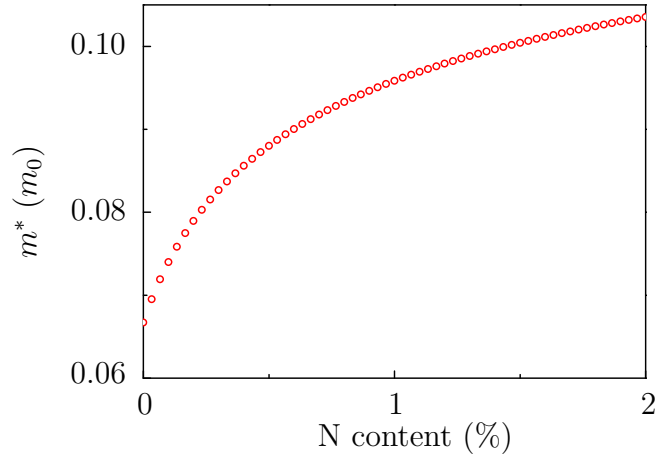


Figure 2.5.: BAC electron effective mass of $\text{GaAs}_{1-x}\text{N}_x$ with varying nitrogen content x . Equations (2.22) and (2.7) are used for the calculation.

Eq. (2.19) transforms into [165]

$$m_{\text{BAC}}^*(x) = 2m_{\text{GaAs}}^* \left(1 - \frac{E_0^c - E^d}{\sqrt{(E_0^c - E^d)^2 + 4V^2x}} \right)^{-1} \quad (2.22)$$

with the same nomenclature as in the former section. Fig. 2.5 illustrates Eq. (2.22) for 100 K, which corresponds to the temperature of our experimental studies (see Chap. 4). In particular, the energy of the GaAs CB is set to $E_0^c(100 \text{ K}) = 1.501 \text{ eV}$, according to the Varshni formula [154]. The nitrogen level and interaction strength are $E^d = E^c + 0.23 \text{ eV}$ and $V = 2.7 \text{ eV}$, respectively [157]. A smooth increase of the BAC electron effective mass m_{BAC}^* with nitrogen content x can be observed in Fig. 2.5.

2.4. Empirical pseudopotential method

Kent and Zunger [159, 74, 75] developed a model for strongly perturbed alloys based on large-scale atomistic supercell calculations and the empirical pseudopotential method, as an extended alternative to the BAC model. The principle of the method is based on the description of the micro- and nanostructure of a system by distributing cations and anions in a large supercell. The atomic ordering and intended alloy concentration have to be taken into account. The relaxation processes are described by a simple “balls and springs” Hamiltonian [72, 100] and the crystal potential $V(\mathbf{r})$ is written as a superposition of screened atomic pseudopotentials $v_\alpha(\mathbf{r})$ with $\alpha = \text{Ga, N, As}$ [74, 75]. This allows to calculate the electrical and optical properties of large supercells. The calculation procedure of the empirical pseudopotential method is introduced in the first part of this section. In the second part, the electronic structure of $\text{GaAs}_{1-x}\text{N}_x$ is discussed in the dilute regime. The third part is dedicated to the evolution of the electronic structure with increasing nitrogen content x .

2.4.1. Calculation procedure

Adding $0 \leq I \leq 20$ nitrogen atoms randomly at the anion site of GaAs into a supercell with up to $13824 - I$ GaAs pairs leads to a natural evolution of the electronic structure of GaAsN [74]. In the empirical pseudopotential method, Ga can be surrounded by

five possible configurations of As and N atoms $\text{As}_n\text{N}_{4-n}$ with $0 \leq n \leq 4$ [74]. The resulting eigenstates can be analyzed with respect to their localization degree [74]. Calculating the distance $R_j^{(i)}$ from the j th nitrogen site at which 20% of the eigenstate ψ_i is enclosed, classifies the energy levels in “localized” or “quasi-localized” [74]. Kent and Zunger [74, 75] repeated the procedure for 15 randomly selected configurations of GaAsN. Fig. 2.6 shows a selection.

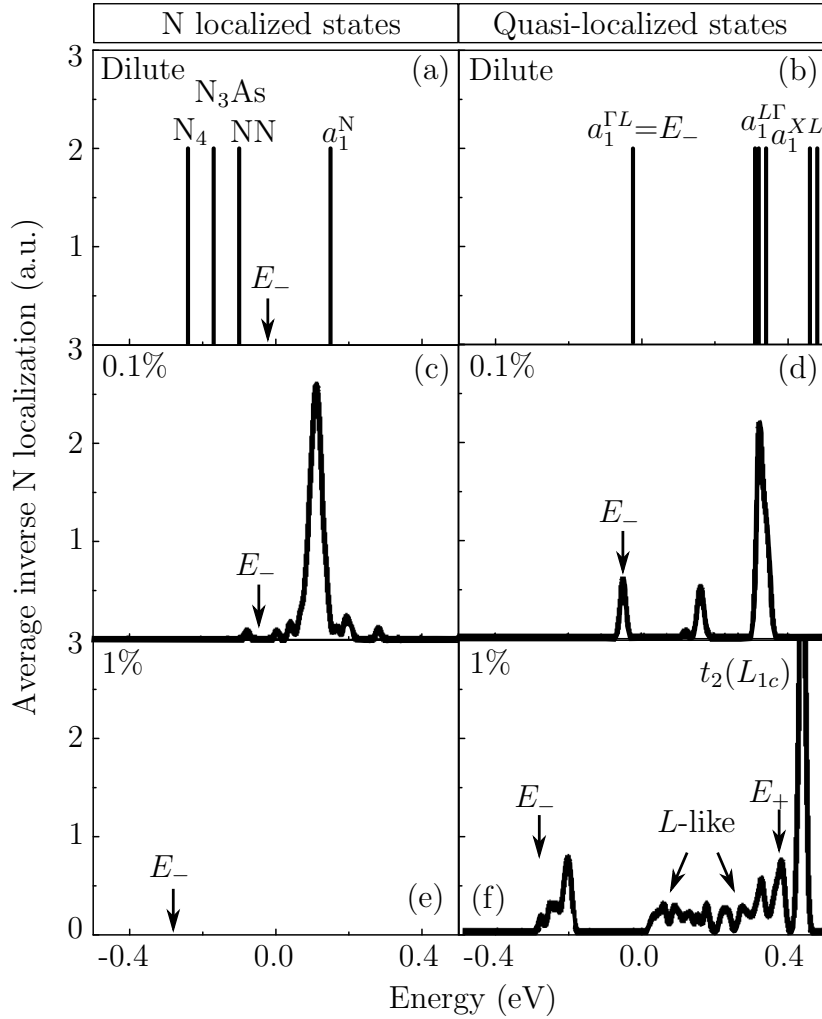


Figure 2.6.: Spectral dependence of the nitrogen localization for cluster states (left) and perturbed host states (right) of GaAsN. The nitrogen concentration is increased from dilute to 1% in the vertical direction. The CB minimum of the lowest band E_- is indicated by vertical arrows. Different energetic states are shown. The figure is adapted from Ref. [75].

2.4.2. Electronic structure in the dilute regime

Energetic states with different localization characters emerge in dilute GaAsN upon the appearance of nitrogen as isolated or bound impurity [74]. In case of the isolated impurity, Kent and Zunger observed a strong coupling with GaAs host states and the evolution of four a_1 -like states¹ from the basis $a_1(X_{1c}) + a_1(L_{1c}) + a_1(\Gamma_{1c}) + a_1(N)$ [74]. The lowest $a_1^{\Gamma L}$ level is classified as quasi-localized [74] and forms the new CB edge, as shown in Fig. 2.6 (b). In analogy to the BAC model [136], this state will be referred to as E_- . Approximately 150 meV above the CB edge, a strongly localized a_1^N state is observed in Fig. 2.6 (a), which is well known from the literature [164, 95]. The perturbed host states $a_1^{L\Gamma}$ and a_1^{XL} appear approximately 280 meV and 420 meV above the CB edge, respectively and show a much lower localization character [74]. These quasi-localized states are depicted in Fig. 2.6 (b). Furthermore, nitrogen introduces strongly localized cluster states in the band gap [60], which are shown in Fig. 2.6 (a). These levels can be associated with NN pairs, triplets N_3As and quadruplets N_4 and have a relatively low concentration in the alloy [74]. Nevertheless, they can be observed e.g. in photoluminescence measurements, caused by effective population via tunneling from perturbed host states.

2.4.3. Evolution of electronic structure with N composition

Fig. 2.6 (c) - (f) illustrate the shift of the CB edge to lower energies with nitrogen content. This behavior can be explained by anticrossing and repulsion with higher energy members of the perturbed host states [74]. The position of cluster states remains fixed in the forbidden gap, because of the high localization character and weak interaction [74]. The downward moving CB “swallows” discrete cluster states one-by-one, until the lowest cluster state is overtaken by perturbed host states at a critical concentration x_c [74]. This concentration can vary upon the degree of randomness in the samples and is equal to 0.6% in the calculation of Kent and Zunger [74]. At the same time, new virtual bound states appear in the CB of GaAsN and form bands. These bands can be associated with the E_+ band, in analogy to the BAC model [136], and a t_2 -like band¹. E_+ shifts to higher energies with increasing nitrogen content, like in the BAC model [136]. The CB minimum is formed from both localized

¹ a_1 and t_2 are two of the five irreducible representations of the point group T_d .

and delocalized states in the vicinity of the critical concentration [74]. This duality is responsible for exciton localization, slow decay times, Stokes shift between absorption and emission, etc. [27], which cannot be described by the two-level anticrossing model [136]. For nitrogen concentrations $x \gg x_c$, GaAsN shows a more conventional alloy behavior. More information can be found in Refs. [74, 75].

2.5. Linear combination of isolated nitrogen states method

The properties of dilute nitrides can be explained inter alia with two different methods, namely the empirical BAC model [136] or detailed band structure calculations [74, 75], which are introduced in Sec. 2.3 and Sec. 2.4, respectively. Lindsay and O'Reilly aimed for a unification of these models for a quantitative description of Ga(In)NAs with their approach [94, 114]. In the first part of this section, the linear combination of isolated nitrogen states (LCINS) model is presented by describing isolated nitrogen and cluster states. The LCINS effective mass is in the focus of the second part.

2.5.1. Isolated nitrogen and cluster states

Detailed sp^3s^* tight-binding calculations were performed to determine the defect-related levels due to isolated nitrogen atoms and cluster-states in large GaAsN supercells [115]. The CB edge state $|\psi_{c1}\rangle$ of a $\text{Ga}_{864}\text{As}_{863}\text{N}_1$ supercell can be written as a linear combination of the GaAs CB edge state $|\psi_{c0}\rangle$ and the isolated nitrogen state $|\psi_{N0}\rangle$, according to the BAC eigenstate problem (2.6). The isolated nitrogen state is therefore defined with $\alpha = \langle \psi_{c1} | \psi_{c0} \rangle$ [115, 93, 94] by

$$\psi_{N0} = \frac{\psi_{c1} - \alpha\psi_{c0}}{\sqrt{1 - \alpha^2}}. \quad (2.23)$$

In case of nitrogen pairs or clusters, the situation strongly depends on the statistical distribution of the N atoms [94]. In particular the number of N pairs and of the larger and less common clusters in the supercell is essential. In order to minimize statistical variations between random supercells, large $\text{Ga}_N\text{As}_{N-M}\text{N}_M$ supercells must be used (e.g. $N = 10^6$ and $M = 10^4$ for $x = 1\%$) [94]. However, tight-binding

calculations are not feasible with clusters of that size. To overcome this problem, GaAsN CB edge wave functions Φ_j are represented as a linear combination of M isolated nitrogen resonant states ψ_{Ni} with $i = 1, \dots, M$ and the GaAs CB edge wave function ψ_{c0} [93, 94]. This procedure is called linear combination of isolated nitrogen states and yields results in excellent agreement with tight-binding calculation results, as was shown on a supercell with $2N = 1000$ atoms [94, 114]. In the general case $(M + 1) \times (M + 1)$ matrix equations must be solved with $H_{ij}\Phi_j = E_{ij}\Phi_j$ in order to analyze these supercell CB states [94]. The full GaAsN Hamiltonian H is defined by

$$H_{ij} = \langle \psi_{Ni} | H | \psi_{Nj} \rangle \quad (2.24)$$

$$H_{i,M+1} = \langle \psi_{Ni} | H | \psi_{c0} \rangle \quad (2.25)$$

with $1 \leq i, j \leq M$ [94]. The matrix $S_{ij} = \langle \psi_{Ni} | \psi_{Nj} \rangle$ enables the overlap of neighboring N states. First, it is reasonable to diagonalize the $M \times M$ matrix, which links the individual Φ_{Ni} states with the energy E_i [94]. The histograms in Fig. 2.7 (a) show the distribution of the N-cluster states energies and their interaction $V_N(E) = \sum |V_l|^2 T(E - E_l)$ with the CB edge state $|\psi_{c0}\rangle$. The interaction strength is given by $V_l = \langle \Phi_{Ni} | H | \psi_{c0} \rangle$ and $T(x)$ is a top-hat function of width 2 meV and unit area [94]. In the superdilute regime (upper picture), most interactions arise from states close to the isolated nitrogen level ($E_N = 1.7$ eV at 0 K) [94]. The small features around 1.5 eV and 1.6 eV can be associated with N-N pairs and second-neighbor N atoms, respectively [94]. At higher N contents (lower picture), a considerable broadening of $V_N(E)$ can be observed [94]. Furthermore, large cluster states can be found at the low-energy side. The complete LCINS spectrum is obtained by diagonalizing the $(M + 1) \times (M + 1)$ matrix [94]. Fig. 2.7 (b) shows its projection on the unperturbed wave function ψ_{c0} for two different nitrogen concentrations. This so-called fractional Γ -character

$$f_{\Gamma c} = |\langle \Phi_j | \psi_{c0} \rangle|^2 \quad (2.26)$$

of the CB grants access to the different state types $|\Phi_j\rangle$ [94]. The new CB edge E_- is identified by the greatest Γ -character and exhibits a red-shift with increasing N content [94]. This observation is in agreement with the BAC model [136] and experimental results [77]. Furthermore, E_+ appears at $x = 0.2\%$ and shows a significant blue-shift

and a rising Γ -character when the N content is elevated [94]. The position of the CB edge with respect to N-related levels affects the interaction strength $V_i = \langle \Phi_{Nl} | H | \psi_{c0} \rangle$ and leads to a reduction of the Γ -character of E_- in the vicinity of N levels [94]. This

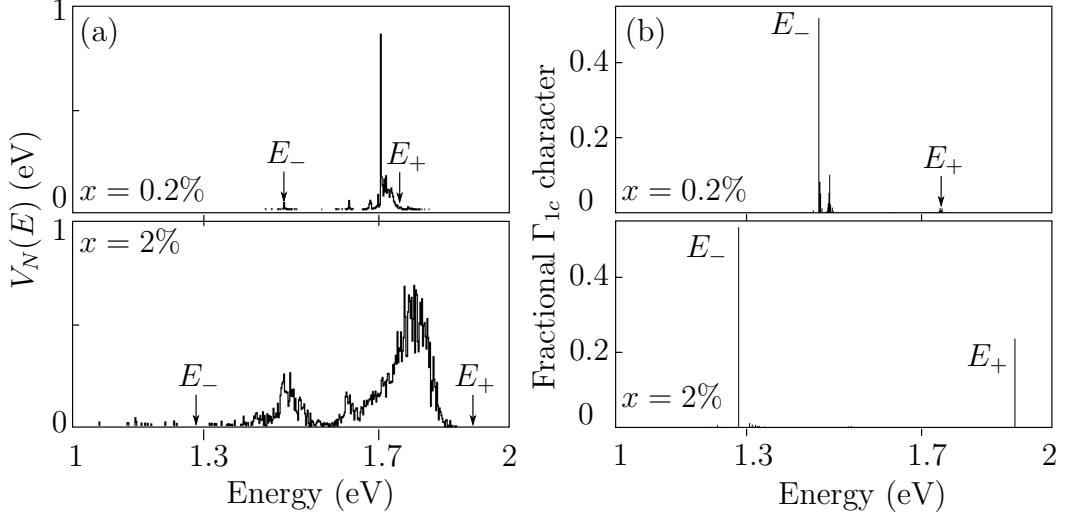


Figure 2.7.: (a) Distribution of N cluster state energies E_l weighted by the square of their interactions $|V_l|^2 = |\langle \Phi_{Nl} | H | \psi_{c0} \rangle|^2$ with the CB edge state for $\text{GaAs}_{0.998}\text{N}_{0.002}$ (upper picture) and $\text{GaAs}_{0.98}\text{N}_{0.02}$ (lower picture). (b) Projection of the LCINS spectrum onto the GaAs wave function ψ_{c0} for $x = 0.2\%$ (top) and $x = 2\%$ (bottom). The figures are adapted from Ref. [94].

observation differs from the two-level BAC model [136] predictions and is responsible for the anomalous composition dependence of the LCINS electron effective mass in GaAsN [114], which is discussed in the following.

2.5.2. LCINS electron effective mass

The BAC effective mass is discussed in Sec. 2.3.2. A smooth increase of the mass is observed with nitrogen content x . In this section, the LCINS effective mass is presented. It can be determined in the framework of the LCINS method by assuming that the valence band fractional Γ -character f_{Γ_v} varies as $1 - x$ [92, 94]. The electron effective mass of GaAsN is given by

$$m_{\text{GaAsN}}^* = \frac{m_{\text{GaAs}}^* E_-}{E_{CB} f_{\Gamma_c} f_{\Gamma_v}}. \quad (2.27)$$

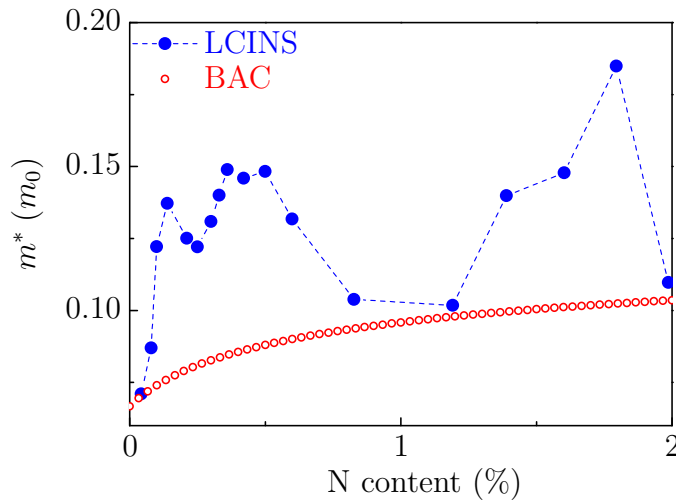


Figure 2.8.: Electron effective mass of GaAsN in dependence of the nitrogen content x . The full blue circles represent LCINS calculations, which are adapted from Ref. [94] and the open red circles stand for the BAC model calculation with Eq. (2.22), as explained in Sec. 2.3.2.

Consequently, it is proportional to the energy gap E_- and inversely proportional to the fractional Γ -character (2.26) in the $k \cdot p$ model [92, 94]. Fig. 2.8 shows the highly non-monotonic behavior of the LCINS electron effective mass as a function of nitrogen content x in comparison with much lower monotonic BAC masses. This result demonstrates that exceptionally large mass values are possible in samples with a particularly strong interaction between ψ_{c0} and Φ_{Nl} [93, 94]. These interactions result in low values of $f_{\Gamma c} < 0.25$. For more details on the LCINS method, please check the references [94, 114].

2.6. Fundamentals of cyclotron resonance

Cyclotron resonance (CR) designates the resonant absorption of electromagnetic radiation by charged carriers (typically electrons) in a static magnetic field. It was first observed by Dresselhaus et al. [39, 40] and by Lax et al. [91] in germanium and silicon, respectively. An absorption process only takes place if the radiation frequency matches the so-called cyclotron frequency $\omega_c = eB/m$, where e is the elementary charge, B the magnetic field, and m the free electron mass. The cyclotron frequency can be deduced classically, as shown in Sec. 2.6.1 or with a quantum mechanical

approach, as presented in Sec. 2.6.2. In semiconductors, the mass is replaced by the electron effective mass m^* . The latter typically corresponds to a fraction of the free electron mass and is closely related to the band structure of the system. Thus, CR spectroscopy is a direct method for effective mass determination and studying the band structure. Furthermore, it provides information on scattering times and on the free-carrier concentration. The experimental setup for CR experiments is introduced in Sec. 3.1.

2.6.1. Classical cyclotron resonance: Drude model

The electron motion in electric and magnetic fields \mathbf{E} and \mathbf{B} can be expressed by the classical equation of motion [109],

$$m^* \frac{d\mathbf{v}}{dt} + \frac{m^* \mathbf{v}}{\tau} = -e\mathbf{E} - e(\mathbf{v} \times \mathbf{B}) \quad (2.28)$$

with the electron effective mass m^* and the electron velocity \mathbf{v} . The second term on the left hand side takes into account electron scattering. We consider the magnetic field \mathbf{B} to be parallel to the z -direction and the electric field vector \mathbf{E} to be perpendicular to z in the Faraday geometry. Solving the differential equations gives the conductivity tensor [109]

$$\boldsymbol{\sigma} = \frac{\sigma_0}{\tau} \begin{pmatrix} \frac{-i(\omega-i/\tau)}{(\omega-i/\tau)^2 - \omega_c^2} & \frac{\omega_c}{(\omega-i/\tau)^2 - \omega_c^2} & 0 \\ \frac{-\omega_c}{(\omega-i/\tau)^2 - \omega_c^2} & \frac{-i(\omega-i/\tau)}{(\omega-i/\tau)^2 - \omega_c^2} & 0 \\ 0 & 0 & \frac{-i}{\omega-i/\tau} \end{pmatrix}, \quad (2.29)$$

which is defined by the relaxation time τ , the DC conductivity $\sigma_0 = ne^2\tau/m^*$, the carrier density n and the cyclotron frequency

$$\omega_c = \frac{eB_{\text{res}}}{m^*}. \quad (2.30)$$

The real part of the conductivity

$$\Re(\sigma_{xx}) = \sigma_0 \frac{1 + (\omega\tau)^2 + (\omega_c\tau)^2}{[1 - (\omega^2 - \omega_c^2)\tau^2]^2 + 4(\omega\tau)^2} = \varepsilon_0 cn_1 \alpha \quad (2.31)$$

provides a classical expression for the CR absorption coefficient α [109, 35] in case of linearly polarized radiation. Eq. (2.31) is used in Sec. 4.2 and Sec. 4.3 for data analysis.

However, at this point it is more instructive to consider a different representation of the conductivity [109, 35]

$$\sigma_{\pm} = \sigma_{xx} \mp i\sigma_{xy} \quad (2.32)$$

$$= \sigma_0 \left[\frac{1}{1 + (\omega \mp \omega_c)^2 \tau^2} - i \frac{(\omega \mp \omega_c) \tau}{1 + (\omega \mp \omega_c)^2 \tau^2} \right] \quad (2.33)$$

in terms of the left- and right-circularly polarized radiation. The signs “+” and “−” denote the right and left circular polarization, respectively. For electrons, the resonance only takes place for right-circularly polarized radiation. Thus, electrons are called CR active for σ_+ . On the other hand, holes are CR active for σ_- . This distinction originates from different signs of their charges and thus of ω_c [109]. In case of circularly polarized radiation, the CR absorption of electrons is determined by the real part of σ_+ as

$$\Re(\sigma_+) = \sigma_0 \frac{1}{1 + (\omega - \omega_c)^2 \tau^2} = \varepsilon_0 c n_1 \alpha. \quad (2.34)$$

Eq. (2.34) corresponds to a pure Lorentzian with a peak at ω_c and a half-width at half-maximum of $\gamma = 1/\tau$. Consequently, CR of electrons takes place for $\omega = \omega_c$ if the cyclotron condition

$$\omega_c \tau > 1 \quad (2.35)$$

is satisfied. The cyclotron condition implies that on average carriers have to complete one full orbit before a scattering event occurs. Using the mobility $\mu = e\tau/m^*$, Eq. (2.35) can be written as

$$\omega_c \frac{\mu m^*}{e} > 1 \quad (2.36)$$

and a new definition of the cyclotron condition

$$B \cdot \mu > 1 \quad (2.37)$$

follows from Eq. (2.30) and Eq. (2.36). Both the sample mobility and the magnetic field strength affect the applicability of the CR experiment.

2.6.2. Landau level quantization

The Hamiltonian of a free (crystal) electron in a magnetic field is given by

$$H_0 = \frac{1}{2m^*} (\mathbf{p} + e\mathbf{A})^2, \quad (2.38)$$

where \mathbf{p} is a canonical momentum operator and \mathbf{A} is the vector potential of the magnetic field $\mathbf{B} = \nabla \times \mathbf{A}$. The latter can be represented in the asymmetric Landau gauge for simplicity. Thus, the vector potential is written as $\mathbf{A} = (0, Bx, 0)$ with the position operator $\mathbf{x} = (x, 0, 0)$ and $|\mathbf{B}| = |(0, 0, B)| = B$. In this representation, the Hamiltonian is defined by

$$\begin{aligned} H_0 &= H_{\perp} + H_{\parallel} \\ &= 1/(2m^*) [p_x^2 + (p_y + eBx)^2] + 1/(2m^*) \cdot p_z^2. \end{aligned} \quad (2.39)$$

H_{\parallel} describes the electron motion in the z -direction and has the eigenstate $\frac{\hbar^2 k_z^2}{2m^*}$. H_{\perp} can be transformed to

$$H_{\perp} = \frac{p_x^2}{2m^*} + \frac{1}{2} m^* \omega_c^2 \left(x - \left(-\frac{\hbar k_y}{eB} \right) \right)^2 \quad (2.40)$$

with $\omega_c = eB/m^*$ and $p_y = \hbar k_y$. H_{\perp} corresponds to the Hamiltonian of a shifted harmonic oscillator with an orbit center coordinate $x = -\hbar k_y/eB$ in Eq. (2.40). Its eigenvalues are consequently $(N + 1/2)\hbar\omega_c$. The eigenstates of H_0 are given by a sum of the individual eigenstates of H_{\parallel} and H_{\perp} as

$$E_N(k_z) = \left(N + \frac{1}{2} \right) \hbar\omega_c + \frac{\hbar^2 k_z^2}{2m^*}, \quad (2.41)$$

because H_{\perp} commutes with H_{\parallel} . Consequently, bulk semiconductor electrons can only move freely in the z -direction when a magnetic field $\mathbf{B} = (0, 0, B)$ is applied. The xy motion is quantized in a series of one-dimensional Landau levels. Each one of these levels is degenerated with respect to k_y . Cyclotron resonance is regarded as a transition between neighboring Landau states, if the photon energy is equal to their spacing $\hbar\omega_c$. The absorption between Landau levels can be also calculated in the quantum mechanical approach but is beyond the scope of this thesis. An extensive description can be found e.g. in Ref. [109].

3. Spectroscopic methods

Cyclotron resonance and magneto-photoluminescence spectroscopy are very powerful tools for materials research. In this thesis, different spectroscopic methods are applied to the dilute nitride GaAsN in order to study the electron effective mass, electron mobility, luminescence characteristics, recombination dynamics, impact of shallow dopants, formation and evolution of cluster states and the population transfer of localized excitons. The experimental details of these methods are discussed in this chapter. The first section is dedicated to cyclotron resonance spectroscopy in pulsed magnetic fields. A general introduction on high magnetic field generation is given with a focus on pulsed magnetic fields. Afterwards, the experimental setups and applied THz laser sources are presented. In particular, the free-electron laser FELBE and quantum cascade lasers are introduced. The second section treats time-resolved magneto-photoluminescence. Photoluminescence investigations are performed with a pulsed titanium-sapphire laser. A near-infrared streak camera is used as detection system. A new magneto-photoluminescence setup for pulsed magnetic fields is built at the Dresden High Magnetic Field Laboratory (HLD). Details on this task are given in section three. This includes the development of an experimental setup and an appropriate measuring technique.

3.1. Cyclotron resonance spectroscopy

Cyclotron resonance (CR) spectroscopy is very popular for effective mass determination and studying the band structure. The method provides direct access to electronic states and electron interactions [109]. There are two ways to measure CR. In the first approach, the sample is located in a constant magnetic field and illuminated with electromagnetic radiation by either a broadband source or by a narrow and tunable source. The radiation is absorbed resonantly when the energy of the electromagnetic wave matches the cyclotron frequency $\omega_c = eB_{\text{res}}/m^*$, which is deduced in Sec. 2.6.1.

In the second approach, the sample is illuminated with monochromatic radiation, while the magnetic field is swept. The resonant absorption occurs at a certain resonant magnetic field

$$B_{\text{res}} = \frac{\omega m^*}{e}. \quad (3.1)$$

As usual, e and B designate the elementary charge and the magnetic field, respectively, and m^* represents the effective mass of charged carriers. Both principles are known as cyclotron resonance spectroscopy and can be applied successfully if the cyclotron condition in Eq. (2.37) is satisfied. In case of e.g. GaAs with $\mu = 8500 \text{ cm}^2/\text{Vs}$ at 300 K [149], it can be applied for $B > 1.2 \text{ T}$.

3.1.1. High magnetic field generation

High magnetic fields provide several advantages for CR investigations. According to Eq. (2.37), low mobility samples can only be investigated in high magnetic fields. Furthermore, the variation of the cyclotron energy $\hbar\omega_c$ gives access to interesting effects related to phonons or plasmons, which appear in different energetic ranges. In case of very high magnetic fields, one can obtain new phenomena which arise from electron-electron interactions or the breakdown of the effective mass approximation

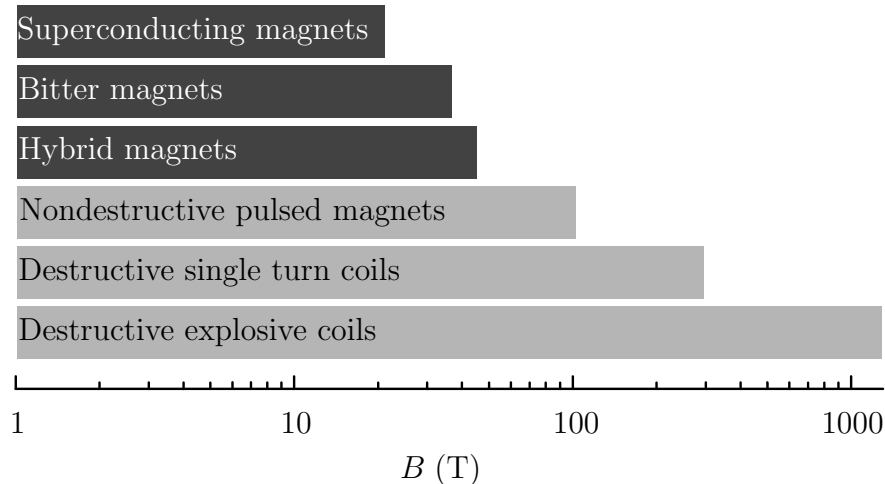


Figure 3.1.: Different methods for high field generation [35], arranged in order of maximum achievable field strength. DC and pulsed fields are shown in dark and light gray, respectively.

[109]. There are different methods to obtain high magnetic fields, as shown in Fig. 3.1. The most common principle is based on superconducting DC coils. Commercially available coils can be operated up to 22 T. Superconducting magnets need to be cooled with liquid helium below the critical temperature in order to ensure a loss-free electrical current. Fields up to ≈ 37 T can be achieved with Bitter magnets. These resistive coils are made of a conductive plate set in helical configuration and operated with large currents. A great amount of deionized water has to be pumped through the magnet in order to dissipate up to 20 MW of heating power. Hybrid magnets are built as a combination of an external superconducting coil with a Bitter magnet inside.

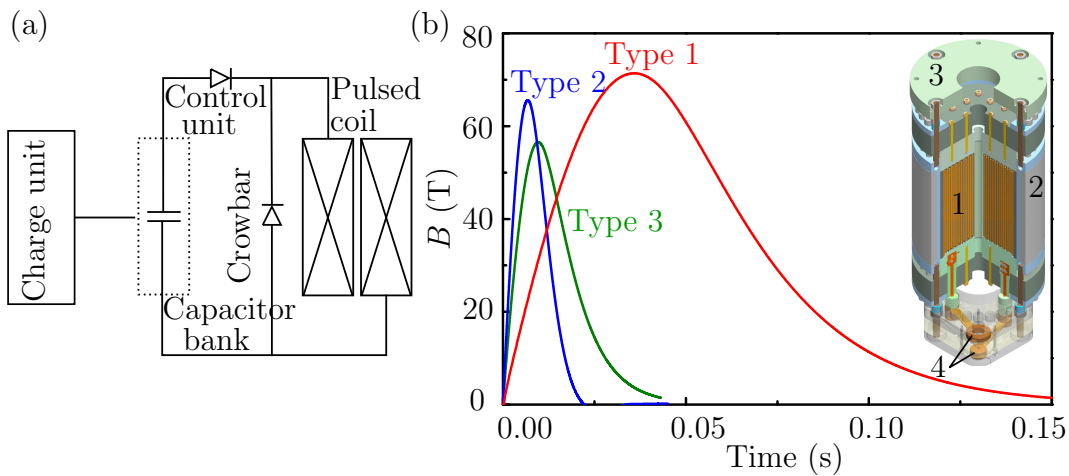


Figure 3.2.: (a) Scheme of the driving circuit for pulsed magnets, adapted from Ref. [35]. (b) Magnetic field profiles of different coil types available at the High Magnetic Field Laboratory Dresden. The inset shows a schematic view of a 8.5 MJ/70 T coil. The main parts are: 1. coil with internal reinforcement, 2. external reinforcement cylinder, 3. G-10 end flanges and 4. current leads.

Magnetic fields up to 45 T can be achieved. Above that, only pulsed magnets are available. Pulsed magnets are further distinguished into three classes: non-destructive magnets with magnetic fields up to 100 T, destructive single turn coils with fields up to 300 T and destructive explosive magnets with fields above 1000 T. In case of single turn coils, only the coil explodes during the pulse, but the sample and setup survive. However, the sample explodes together with the coil in the destructive explosive magnet. Both destructive coils can only be operated on a microsecond time-scale [35].

Our experiments are performed in non-destructive pulsed magnets at the High

Magnetic Field Laboratory Dresden (HLD), which are introduced in more detail in the following. Fig. 3.2 (a) shows the schematic LC driving circuit of a HLD pulsed magnet. The solenoid is driven by a 50 MJ/24 kV capacitor bank, which consists of 20 modules [59]. Depending on the technical requirement, the models can be operated in different combinations. Three main coil types are currently available for user operation, as shown in Fig. 3.2 (b). Each coil is installed in a liquid nitrogen bath inside of a blast-protected cave. In our experiments, a “type 1” coil is used with a maximum field strength of 63 T. The fully charged capacitor (3 modules) discharges into the coil at the time $t = 0$. During the discharging process, the electrical current rises as $\sin(t/\sqrt{LC})$. The maximum is reached at the time $t = \pi\sqrt{LC}/2$ and decays afterwards [35]. Parallel to the coil, a special crowbar-diode is installed, in order to avoid negative recharging of the coil and to increase the sweep-down time. This diode short-circuits the coil when the voltage on the capacitors becomes slightly negative and causes an exponential decay $\exp(-L/R)$ of the current, instead of the sine-like one [35]. R denotes the coil resistance. The surplus coil energy dissipates by Joule heat and increases the coil temperature from 77 K to above room temperature within milliseconds [35]. The waiting time between magnetic pulses is defined by the cooling time of the coil and lies typically between two and four hours. The Lorentz force exerts serious mechanical stress on the coil. To overcome the mentioned challenges, the so-called “exploitation of distributed internal reinforcement” [20] approach is applied at the HLD. In particular, every wire layer is individually supported by a reinforcement layer in order to homogenize the stress distribution. This reinforcement consists mainly of a high-strength fiber in an epoxy-resin matrix [173]. Apart from the internal reinforcement, the coils are reinforced externally with steel cylinders, which provide additional radial, hoop, and axial support for the coil [173]. The inset of Fig. 3.2 (b) shows a typical HLD coil for field strengths of up to 70 T.

3.1.2. Free-electron laser

Free-electron lasers (FELs) are widely tunable light sources of high brilliance, which can be operated inter alia in the desirable THz range. The active medium of the laser consists of relativistic electrons in an alternating magnetic field, which makes this laser type unique in terms of tunability. Continuous energetic states of free electrons are responsible for this extraordinary property. The emission range of the FEL is thus

only limited by technical requirements of the accelerator and undulator. In contrast to other lasers, population inversion is not required for the lasing process. The resonator is built by a cavity with two concave mirrors, as shown in Fig. 3.3. Electrons are accelerated to relativistic energies and guided into the undulator by a dipole magnet. They wiggle through alternating magnets of the undulator with a period of λ_U . Radial acceleration processes cause the emission of spontaneous synchrotron radiation, which interacts with relativistic electrons on its part. As a result, electrons oscillate through

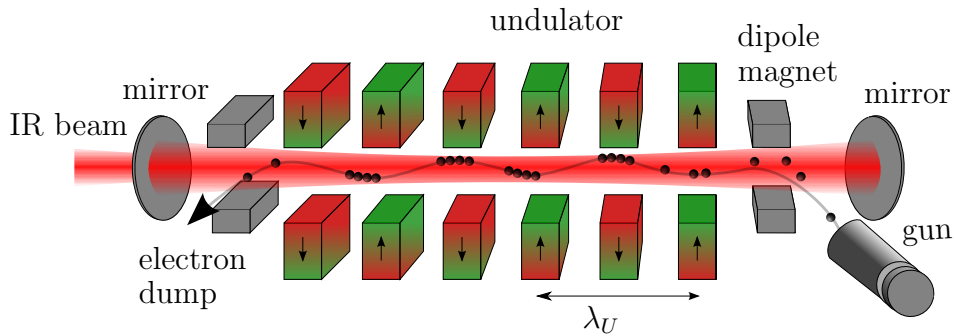


Figure 3.3.: Schematic view of a free-electron laser.

the undulator in bunches and emit coherent radiation. This leads to stimulated emission and optical gain. Cavity mirrors are responsible for the positive feedback and a small hole in one of the mirrors regulates the outcoupling of the FEL radiation. The electrons are extracted to a beam dump after the undulator. The emitted wavelength [76, 174]

$$\lambda = \frac{\lambda_U (1 + K^2)}{2\gamma^2} \quad (3.2)$$

is determined by the electron energy γ , which is given in units of the electron rest energy m_0c^2 , the undulator period λ_U and the undulator parameter

$$K = \frac{eB\lambda_U}{2\pi m_0c}. \quad (3.3)$$

The magnetic field amplitude B describes the field on the undulator axis. The experiments were performed at the FEL facility FELBE using the superconducting Electron Linear accelerator with high Brilliance and Low Emittance (ELBE) at the Helmholtz-Zentrum Dresden-Rossendorf. The laser works in the IR range between

4 μm (310 meV) and 250 μm (5 meV) inter alia in the quasicontinuous regime with 13 MHz repetition rate. The wide energy range is realized by two independent undulators U27 and U100. The former covers the high energetic range between 50 meV and 310 meV and the latter is responsible for lower energies between 5 meV and 62 meV. The average power depends on the wavelength and reaches values up to 20 W [174]. The FEL radiation can be extracted to different optical laboratories in the building or into the adjacent HLD building via a 27 m tunnel. The combination of these two large scale facilities provides a unique spectroscopic access via THz cyclotron resonance spectroscopy in pulsed magnetic fields [36, 37, 38, 45] or THz electron spin resonance in fields up to 63 T [174, 118]. More details on the FEL can be found e.g. in the Refs. [21, 76, 116].

3.1.3. Quantum cascade laser

Quantum cascade lasers (QCLs) are portable but weakly tunable laser sources for the mid-infrared or THz range. The lasing of these unipolar semiconductor lasers occurs by stimulated emission between confined subbands of multiple quantum well (QW) structures [71, 47]. The operating principle can be explained with Fig. 3.4 (a) on the first experimentally realized QCL [47]. The active region consists of three GaInAs QWs with different thicknesses and thus different energy positions of the lowest confined energetic level E_n . The first QW width is 0.8 nm and E_3 has the highest energy. The second and third QW are approximately 3 nm and $E_2 - E_1 \leq \frac{1}{10} (E_3 - E_2)$. Electrons are injected resonantly into the $n = 3$ energy state of the active area at the beginning of the operating cycle and can relax to the $n = 2$ level via photon emission. Because of the large spatial overlap, the $n = 2$ state can be efficiently depleted via the $n = 1$ level and electrons tunnel out of the active area and move to the next active region along the potential gradient. The population inversion is thus realized by the reduced spatial overlap between $n = 3$ and $n = 2$ states and the strong coupling between $n = 2$ and $n = 1$ levels. Ultra-fast, subpicosecond relaxation processes from E_2 to E_1 with a near-zero momentum transfer are responsible for an efficient depletion of the lower level, as shown in Fig. 3.4 (b). Consequently, lasing occurs between E_3 and E_2 . With time, more and more photons are emitted, as the electrons stream down the potential staircase. Additional cladding layers confine the radiation propagation parallel to the layers and cleaved facets provide the resonator mirrors. Thus, the heterostructure

crystal acts additionally as a resonator and is responsible for the optical amplification. The spacing of the lasing subbands define the radiation frequency and it can be tuned by material engineering in the same heterostructure [47, 80]. In principle, arbitrarily long wavelengths are possible. However, the fabrication of a lasing THz device with a QCL scheme is challenging. In particular, THz radiation is strongly absorbed by free carriers in THz range QCL waveguides [80]. Furthermore, the population inversion for laser transition energies above the Reststrahlen band is conventionally achieved by an efficient depletion of E_2 with longitudinal optical phonons. Moving to longer wavelengths requires novel designs. Köhler et al. [80] presented the first THz QCL, operating below the longitudinal optical phonon band.

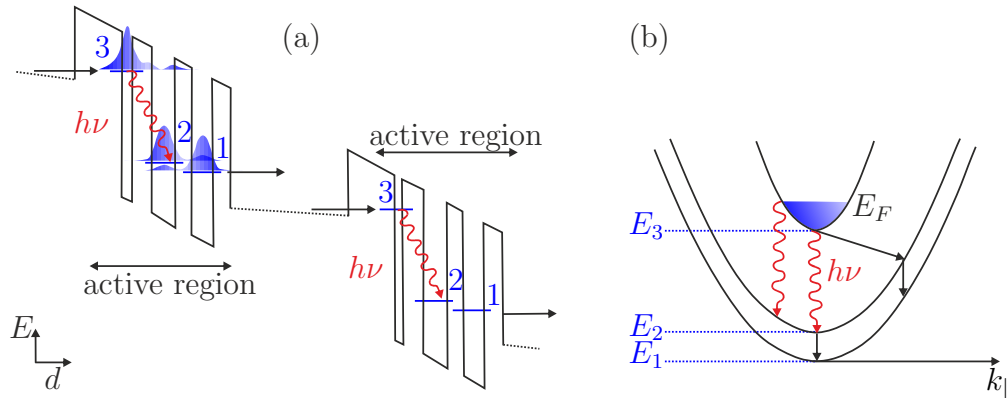


Figure 3.4.: Operating principle of a quantum cascade laser: (a) CB energy diagram of an AlInAs/GaInAs QCL with electron probability density functions. The CB edges are shown as dashed lines. (b) Energy dispersion of the three relevant states E_1 , E_2 and E_3 . The red wavy arrows indicate radiative transitions and the straight arrows represent intersubband optical-phonon scattering events. The figure is adapted from Ref. [47].

Mid-infrared and THz QCLs are applied in magnetic fields within the framework of this thesis. Magnetic fields have different impacts on the band structure of a QCL, regarding the application direction. Fields parallel to the QW plane affect the electronic band structure and the emitting wavelength [31]. A changing wavelength during the magnetic pulse is very inconvenient and precludes this field configuration [38]. A perpendicular magnetic field, on the other hand, quantizes the in-plane carrier motion into Landau-levels. Due to intersubband dipole transition selection rules and thus the conservation of the Landau-level number, the wavelength of the QCL is not dependent on the perpendicular magnetic field in the parabolic approximation.

Hence, this field configuration was chosen in our experimental setup [38]. Furthermore, the emission efficiency of QCLs can be significantly affected by high magnetic fields [143, 144, 13, 156, 38]. In particular, intersubband magnetophonon resonance causes giant oscillations of the emission intensity [144, 38]. Consequently, QCLs should be kept as far as possible from the field center during the magnetic pulse. For more information on QCLs, please check out the review papers [163, 53].

3.1.4. Design of the experimental setup

Cyclotron resonance THz spectroscopy is performed in pulsed magnetic fields at the HLD with two different setups. The first setup is a compact magnetospectrometer based on infrared QCLs or FEL and was developed by Drachenko et al. [38]. The second setup was originally created for electron spin resonance (ESR) THz spectroscopy by Zvyagin et al. [174], but can be equally utilized for CR THz spectroscopy. In both cases, THz radiation from an external or internal light source is guided into a cryostat, which is located in a pulsed magnet. The light is then focused onto the sample and the transmitted radiation is subsequently directed towards a photodetector. In the following both setups are introduced. The compact magnetospectrometer is presented first and the ESR spectrometer is treated in the second part.

Compact magnetospectrometer based on infrared quantum cascade lasers

The compact magnetospectrometer [38] is shown in Fig. 3.5 (a) and can be operated with removable QCLs (see Sec. 3.1.3) emitting at 103 μm , 75 μm , 70 μm or 15 μm . Alternatively, the external light source FELBE (see Sec. 3.1.2) can be utilized. The custom-designed variable temperature insert (VTI) is located in a He-cryostat (Cryo-Vac: KONTI-IT-Cryostat), which is placed in the bore of a HLD pulse magnet with a bore diameter of 24 mm. THz radiation propagates through a stainless-steel oversized multimode waveguide, which is divided into two equivalent channels. The sample is located in the field center of the sample channel in close proximity of the sample heater, temperature sensor (LakeShore: DT-621-HR silicon diode) and pick-up coil. The CR experiment can be performed in a temperature range between 4.2 K and 200 K without affecting the QCL and the detectors. The second channel functions as a reference. The transmitted radiation is measured by two similar detectors, which are located at the very bottom of the probe. A set of Si:B blocked impurity band

photodetectors, sensitive from $4\ \mu\text{m}$ up to $35\ \mu\text{m}$ [61, 131, 38] can be used on the detector side. Alternatively Ge:Ga detectors can be utilized for the far-infrared spectral region above $30\ \mu\text{m}$. Both detector-types exhibit a significant magnetic field dependence and must be kept as far as possible from the field center. The detector location lies $30\ \text{cm}$ below the field maximum in our setup, which is enough to not

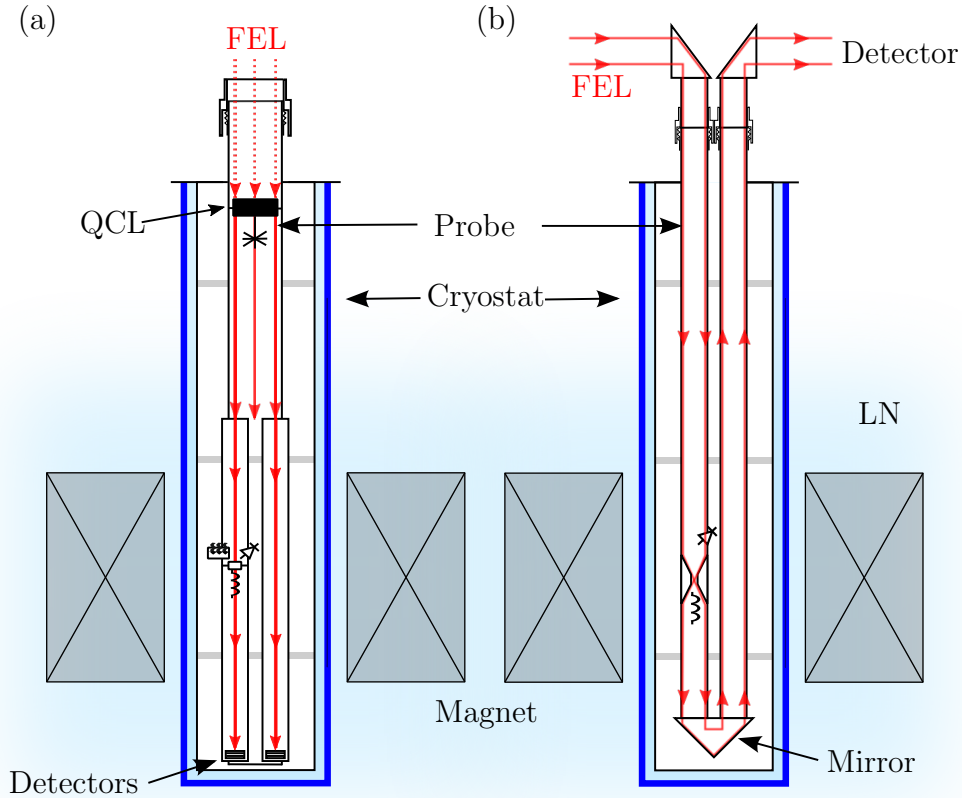


Figure 3.5.: (a) Compact magnetospectrometer based on infrared QCLs [38] and (b) THz-range ESR spectrometer [174]. Both probes are tailored to fit the cryostat, which is located in the bore of a HLD pulsed magnet. The coil is surrounded by liquid nitrogen. The sample is located in the field center in close proximity of a temperature sensor and pick-up coil.

be affected [38]. Nevertheless, Ge:Ga detectors exhibit very large magnetoresistance effects in the low field limit, which can only be compensated by renormalization with the chosen two-channel design. More details on the compact magnetospectrometer can be found in Ref. [38].

THz-range free-electron laser electron spin resonance spectrometer

The operating principle of the THz-range ESR spectrometer [174] can be explained with the schematic representation of the components in Fig. 3.5 (b). External FEL radiation (see Chap. 3.1.2) is introduced into the VTI and propagates through an oversized multimode cylindrical brass waveguide with an inner diameter of 5.6 mm. A cylindrical cone focuses the THz light onto the sample, which is located in the field center of the pulse magnet (see Fig. 3.2 (b)). A standard CernoxTM temperature sensor and pick-up coils for the magnetic field strength are installed in the vicinity. The transmitted radiation is reflected by plane gold-coated mirrors into a parallel waveguide at the end of the pipe and spreads towards the outcoupling window. The emerging radiation propagates through another 10 mm waveguide, outside of the magnet, towards the detector. In order to cover the broad frequency range, different detectors with high sensitivity and fast response have to be used. A helium-cooled Ge:Ga detector (QMC Instrument Ltd.) is suitable for 30 μm – 200 μm and is utilized in our experiments. For shorter wavelengths below 30 μm , a nitrogen-cooled HgCdTe photovoltaic detector (Teledyne Judson Technologies: J15D26-M204-S01M-60) can be applied. The VTI is installed in a suitable cryostat inside of a pulse magnet, which allows to perform the ESR and CR experiments in a temperature range of 1.4 K – 300 K. The FEL wavelength can be monitored with a Bruker VERTEX 80v Fourier-spectrometer before and after the magnetic pulse. Please see Ref. [174] for more details on the THz-range FEL ESR spectrometer.

Measuring procedure and data acquisition

The measuring procedure and data acquisition principle is equivalent in both CR transmission setups. Magnetic field changes are measured by a pick-up coil. Detector signals indicate the transmitted THz radiation. All electrical signals are fed to a fast oscilloscope, which is triggered by an optical signal at the beginning of a magnetic pulse. The temporal distribution of the magnetic field and of the transmitted radiation can be observed. Fig. 3.6 illustrates CR transmission curves of both spectrometers. The results of the compact magnetospectrometer are shown in (a) and (c). The THz-range ESR spectrometer results can be found in (b) and (d). Obviously, the results are in excellent agreement for both QCL and FEL measurements. In case of the FEL, vibrational artifacts appear in the spectra.

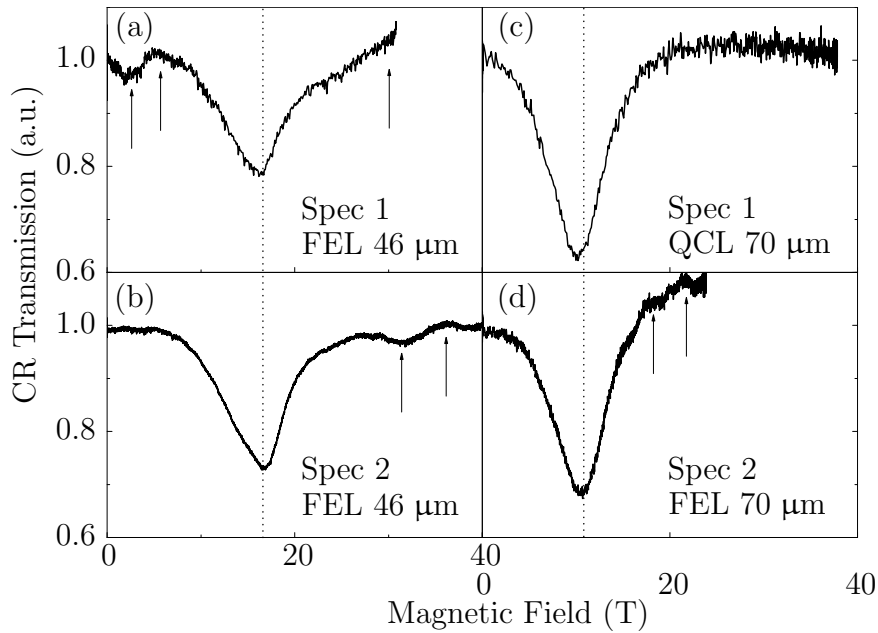


Figure 3.6.: CR transmission spectroscopy on GaAs at 100 K. The measurement is performed with the compact magnetospectrometer (Spec 1) in (a) and (c) and with the THz-range ESR spectrometer (Spec 2) in (b) and (d) with the FEL and QCLs. The results are in excellent agreement. Arrows indicate vibrational artifacts in FEL measurements.

3.2. Time-resolved photoluminescence

Photoluminescence (PL) was first applied by Haynes and Briggs in the early 1950s to investigate the optical properties of germanium [57]. It became a common method only ten years later, when different laser sources became available. Ever since it has been one of the most popular material science techniques. This non-destructive method provides information on the sample composition and allows to study transitions on a femtosecond time scale. The investigation of the temporal behavior of luminescence signals grants a unique access to the identification of the recombination processes and of the microscopic nature of the relevant luminescence centers [121]. This section covers the experimental details on time-resolved photoluminescence (PL) measurements, which are performed with a pulsed titanium-sapphire laser (Spectra Physics: Tsunami 3960). The detection unit consists of a Bruker Chromex 250is/is spectrograph, a Hamamatsu C5680-27 streak camera and a Hamamatsu ORCA-ER C4742-95 charge-coupled device (CCD). In the first part of this section, the experimental setup

and the operating principle of the streak camera is discussed. More details on the functionality of the laser system is given in the second part.

3.2.1. Experimental setup with a streak camera

Figure 3.7 schematically shows the experimental setup of our time-resolved PL investigation. The sample is located in a cryostat and illuminated by a picosecond titanium-sapphire laser (see Sec. 3.2.2). The PL is collected in back-reflection geometry by a set of lenses and focused on the slit of a monochromator. A Czerny-Turner type grating spectrograph (Bruker Chromex 250is/is), whose f-number is $f/4$, serves as dispersion element. Three different gratings with 100, 300 and 1200 lines/mm and a nominal resolution of 1.8 nm, 0.6 nm and 0.15 nm, respectively, are available. As a result, the radiation is divided into quasi-monochromatic fractions, which propagate into the streak camera (Hamamatsu ORCA-ER C4742-95) towards the photocathode.

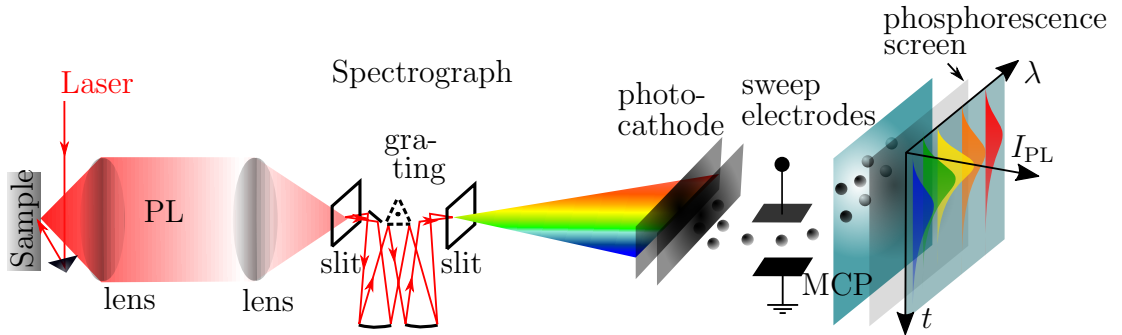


Figure 3.7.: Time resolved PL spectroscopy setup with a streak camera.

The impinging light creates photoelectrons, which are accelerated towards sweeping electrodes. These electrodes constantly deflect the carriers in the vertical direction. The electrode-sweeping is controlled in the manner of an oscilloscope by the synchronization with the titanium-sapphire laser frequency [121]. Photoelectrons thus inject a trace on the phosphorescent screen with a spatial distribution, which correspond to the temporal fingerprint of the PL signal [121]. This signal is digitized by a CCD detector and can be further processed by a computer. A microchannel plate detector (MCP) is employed for signal amplification. In our time-resolved PL experiments, a Hamamatsu C5680-27 streak camera is used. The vertical electrode-sweeping is triggered by the titanium-sapphire laser signal with a Hamamatsu C6878 delay unit.

3.2.2. Laser system

The laser system is introduced in this subsection. In the first part, the titanium-sapphire (Ti:Sa) laser is presented. The neodymium-doped yttrium aluminum garnet (Nd:Y₃Al₅O₁₂ or Nd:YAG) laser is discussed in the second part.

Titanium-Sapphire laser

Ti:Sa lasers are the most popular representatives of pulsed solid-state lasers, which are mainly operated in the femtosecond regime. A Ti³⁺ doped Al₂O₃ crystal serves as the active medium. Interactions with the sapphire host lead to a splitting of the Ti³⁺ 3d shell into ²E and ²T₂ states. These states, on their part, broaden by electron-phonon interactions, as shown in Fig. 3.8 (a). This makes the Ti:Sa system tunable in the near-infrared regime between 670 nm and 1070 nm. A frequency doubled Nd:YAG

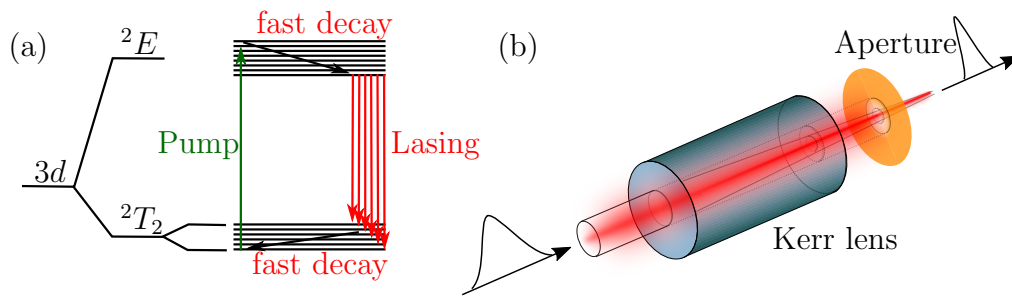


Figure 3.8.: (a) Four-level scheme of a Ti:Sa laser. (b) Passive mode-locking with a Kerr lens. The nonlinear optical Kerr-effect causes an intensity-dependent self-focusing of the laser beam. Fig. 3.8 (a) and Fig. 3.8 (b) are adapted from Ref. [78] and Ref. [73], respectively.

laser (see next section) serves as pump laser. Population inversion can be realized by fast non-radiative transitions within the ²E and ²T₂ bands in combination with a much longer lifetime of the lowest ²E state. The experiments were performed in the picosecond regime on a Spectra Physics Tsunami 3960 [146] with pulse lengths of 3–4 ps and a repetition rate of 78 MHz. This system works with passive mode-locking in the gain medium by the nonlinear optical Kerr lens effect. Fig. 3.8 (b) illustrates the working principle of a Kerr-lens by intensity-dependent self-focusing of the laser beam. Mode-locking can be achieved with a resonator design that favors pulsed regime over continuous-wave (cw) radiation. Usually a “soft aperture” is used as selective element. Within this approach, high-intensity pulses have a bigger overlap with the

pump beam because of the nonlinear optical Kerr-effect. An average output power of 2 W can be achieved at 750 nm. The actual laser wavelength and pulse widths are monitored by a spectrometer (APE Berlin: WaveScan) and an autocorrelator (APE Berlin: PulseScope), which are fed continuously by a fraction of the near-infrared radiation. A frequency doubled Spectra Physics Millennia Pro Nd:YAG laser [145] is used for pumping. More details on the Ti:Sa laser can be found e.g. in Ref. [78].

Nd:YAG laser

Nd:YAG lasers [52] are the most prevalent solid-state lasers. Their application area ranges from medical and production to safety and military operation. The active medium is formed by replacing approximately 1% of Y^{3+} ions with Nd^{3+} ions in the YAG crystal. The four level system has an energy schema that corresponds to energetic levels of a neodymium ion in a YAG host as shown in Fig. 3.9. Nd^{3+} can be excited into several pumped level (1.5 – 1.8) eV above the ground state $^4I_{9/2}$. This

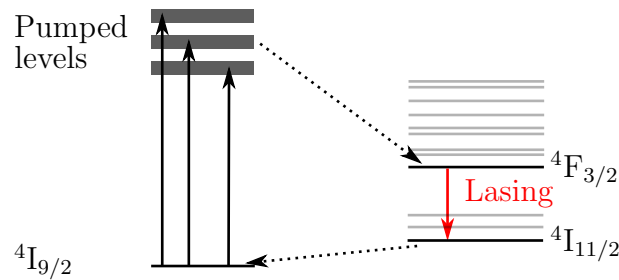


Figure 3.9.: Four level lasing system of a Nd:YAG laser. The figure is adapted from Ref. [78].

can be achieved most easily with diode lasers, which are available in this energy range. The pumped levels are depleted efficiently via non-radiative transitions into the meta-stable $^4F_{3/2}$ -state. Population inversion can be realized with the long life time of the $^4F_{3/2}$ -level and the fast decay times of the ground and pumped states. The most dominant laser transition occurs between $^4F_{3/2}$ and $^4I_{11/2}$ levels with a wavelength of 1060 μm . Besides its function as a pump laser, the frequency doubled Nd:YAG laser is used for photoluminescence investigations in pulsed magnetic fields, which is in the focus of the next section. More details on the Nd:YAG laser can be found e.g. in Ref. [78].

3.3. Magneto-photoluminescence in pulsed magnetic fields

Using external magnetic fields in PL investigations allows one to acquire further knowledge on the band structure of a system. In particular electronic states and the optical band gap can be studied. The magnetic field affects the position and lifts the degeneracy of certain energetic levels upon the relative strength of the perturbation with respect to the electron-hole Coulomb interactions [124]. In this section, PL in pulsed magnetic fields is introduced. One part of this work was to build an experimental setup for magneto-PL measurements in pulsed magnetic fields at the HLD. This task included the development of a measuring probe suitable for HLD pulsed magnets (see Sec. 3.1.1) and the establishment of an appropriate measuring technique. The biggest challenge regarding the equipment was to meet the size and material stability requirements of the probe. The achievement of an acceptable spectral resolution was the biggest technological task. The implementation of the experimental setup, in particular the probe design, is discussed in the first part of this section. The second part is dedicated to the measuring technique and the timing issues.

3.3.1. Experimental setup

The realization of an experimental setup for magneto-PL measurements is mostly limited by the dimensions of the pulsed magnet, as shown in Fig. 3.10. The sample is located in the field center, which lies roughly 1.15 m below the bath cryostat aperture with a diameter of 16.1 mm. Sample holder, optics and detectors thus have to fit into a tube with an inner diameter of 10 mm due to the necessity of an outer shield in a bath cryostat and because of stability requirements on the pipe. In order to effectively collect weak PL signals, we use adjustable lenses in non-magnetic lens holders, which are located in a plastic cylinder as shown in Fig. 3.11. Special polymer parts are designed and built of polyaryletherketone (PEEK) in cooperation with the HZDR workshop. Detailed drawings are attached in appendix A.3. The center of the probe contains a PEEK cylinder tube A with an inner thread. This thread fits perfectly to the outer thread of the lens holders B, which allows to move them into the optimal positions with respect to the sample and fiber. A special tool C

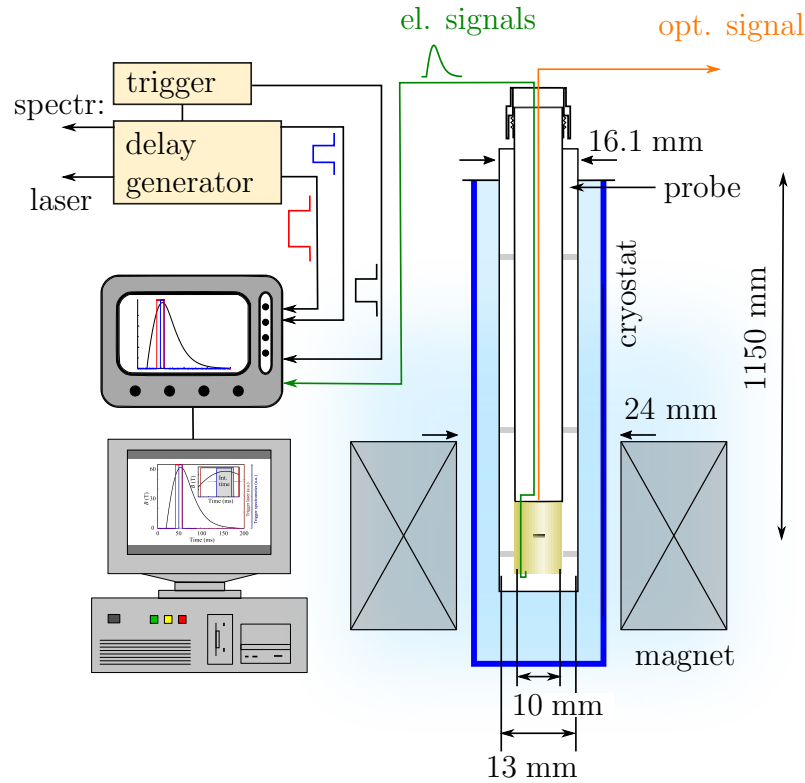


Figure 3.10.: Part one of the experimental setup for magneto-PL at the HLD.

is built as counterpart to the small holes in the lens holders in order to move them in the vertical direction. Slots in the cylinder A give access to the lens holders B. Part D is manufactured to hold two small coils and seal the cylinder A with part G. The heater coil E is made of a brass body with a manganin wrapping and the PEEK coil F is wrapped with a standard thin enameled wire and operates as pick-up. The integrated pick-up signal gives direct access to the magnetic field strength in case of a proper calibration. The sample is directly glued to the heating coil E on the lens side. A LakeShore DT-621-HR miniature silicon diode can be attached on the inner side of the coil, as shown in Fig. 3.12, and works as temperature sensor. On the backside of part G, contact patches connect the pick-up coil, heater and temperature diode with wires from the top of the probe, where they are soldered to a LEMO connector. The temperature is monitored with a LakeShore model 350 temperature controller using the four-point measurement technique and the pick-up signal is recorded with a Yokogawa DL750 digital oscilloscope. On the upper part of the cylinder A, a fiber holder H can be screwed into the cylinder. This part is

designed to hold a 2.5 mm ceramic ferrule, which is chosen as one of the connectors of the custom fiber optic patch cable. A multimode Thorlabs FG050LGA fiber with a length of 1800 mm, a diameter of 50 μm and without tubing is used. On the side of the vacuum feedthrough (outside of the magnet), we select a standard FC/PC connector. All parts are removable and can be replaced in case of a mechanical failure. The main parts A - G of the probe are attached to a 1300 mm long metal

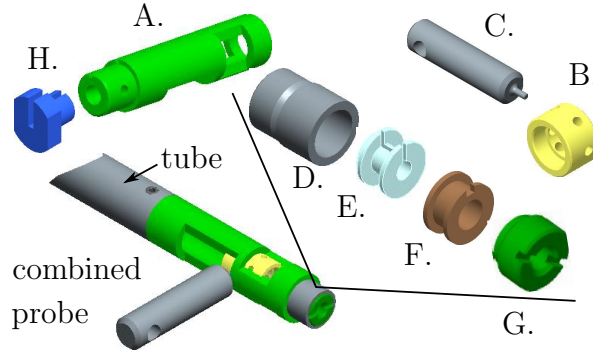


Figure 3.11.: Manufactured probe for magneto-PL measurements in pulsed magnetic fields. A cylinder body A houses two lens holders B, which can be moved with the tool C. Part D is built to hold the heater E and the pick-up F and can be attached to the body A and sealed with the part G. On the other side, a fiber ferrule holder H can be screwed into the cylinder. The body A is connected to a stainless steel tube with two grub screws.

tube made of the stainless steel 1.4571 [41]. The outer shield is manufactured of the same material and has a length of 1500 mm. A vacuum cone is glued with an adapter to the top of the inner tube and sealed with a custom-built blind flange. The flange is equipped with a vacuum feedthrough (Vacom 3IVM-16KF-VV-S) for the fiber and with a vacuum connector (LEMO HGP.3S.314.CLLSV) for electrical signals. Most optical components are located outside of the blast-protected cave on an optical table (see Fig. 3.12) and are linked to the probe via a 5 m fiber through a small hole in the wall. A frequency doubled diode pumped solid state (DPSS) Nd:YAG laser (Laser 2000: CNI-532-500-5-FN-FDA-A1) is used as cw laser source. More details on the Nd:YAG laser can be found in Sec. 3.2.2. The laser light is coupled into the fiber by a microscope objective, as shown in Fig. 3.12, to propagate to the probe. Inside the probe, the radiation is focused on the sample by a set of lenses (Thorlabs: 352330-B with $f = 3.1$ mm on the sample side and 354560-B with $f = 13.86$ mm on the fiber side), which are also responsible for the collection of the PL radiation. All

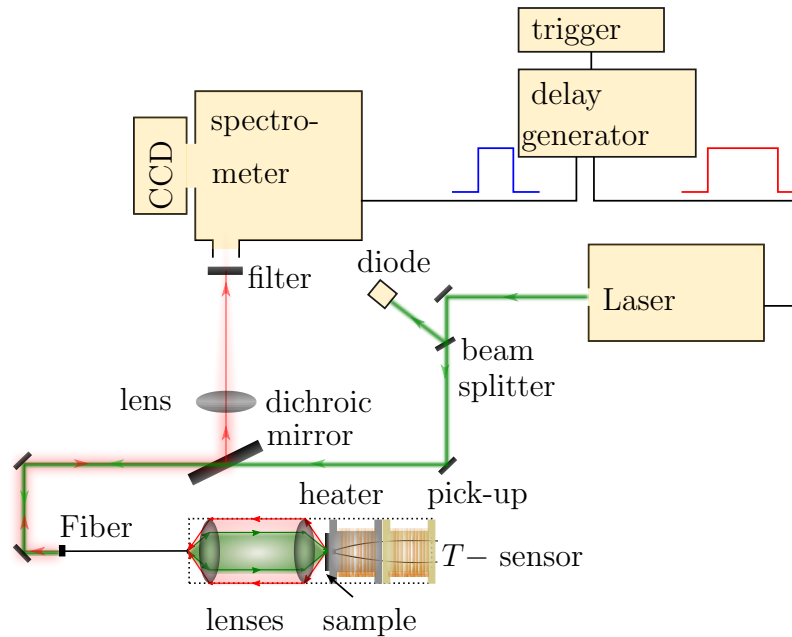


Figure 3.12.: Part two of the experimental setup for magneto-PL at the HLD.

optical components are selected for ideal PL propagation and focusing in the range of 800 – 900 nm. The PL signal is guided through the internal fiber to the external fiber outside of the probe and further to the optical table. On the detection side, a Princeton Instruments spectrometer Acton Spectro2500i [66], whose f-number is $f/6.5$, serves with a nitrogen cooled silicon CCD (Princeton Instruments: Spec-10 system). A shortpass dichroic mirror deviates the radiation towards the spectrometer and a 2" lens focuses the PL on the slit of the spectrograph. Additionally, a longpass filter blocks the remaining laser radiation. The laser power is monitored with a photodiode during the magnetic pulse.

3.3.2. Measuring technique

In principle, the whole magnetic field dependency of the PL can be measured by taking many spectra during one magnetic pulse. However, the finite spectral acquisition time tremendously limits the magnetic field resolution due to the fast field variation in the vicinity of the field maximum (see Fig. 3.13). In fact, in order to obtain an acceptable spectral resolution, it is necessary to take only one spectrum per magnetic pulse. The magnetic field dependency of the PL can be realized by iterating PL

experiments with varying maximum field strengths. The temporal field profiles are carefully investigated, as shown in Tab. A.2. The field variation $\Delta B/\Delta t$ increases linearly with the peak magnetic field. Thus, we have to find a compromise between

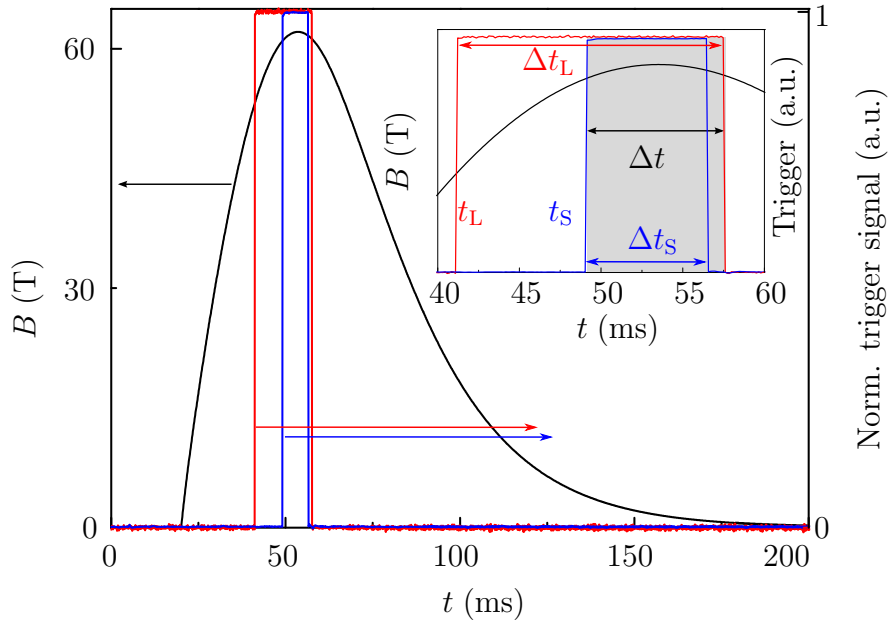


Figure 3.13.: Temporal profile of the magnetic field and the trigger signals of the laser and spectrometer. The acquisition window is opened by the spectrometer trigger $t_S = t_1$ (blue) and closed by the laser trigger $t_L + \Delta t_L = \Delta t + 8$ ms (red). The PL signal is thus recorded for a time Δt symmetrically around the field maximum. The inset shows an enlarged version of the region of interest.

a suitable integration time $\Delta t = t_2 - t_1$ and an acceptable field variation ΔB for high magnetic fields. The resulting times t_1 and t_2 are chosen symmetrically around the field maximum and are also shown in the appendix in Tab. A.2. The temporal synchronization between the magnetic pulse and the detection unit can be realized with a four channel digital delay pulse generator (Stanford Research Systems model DG535). In order to collect the PL signal only during a predefined time window Δt of a few milliseconds, the CCD is operated in a so-called Continuous Cleans regime, which replaces a too slow mechanical shutter. Continuous Cleans removes any charge from the CCD array until the external trigger signal is received. Once the trigger pulse is received, the charge is acquired for a preprogrammed time Δt and read

out afterwards. If the trigger signal is still active at the end of the readout time, the hardware will interpret this as a second trigger pulse. Thus, the length of the spectrometer trigger signal Δt_S has to be shorter than the acquisition and readout time. To be on the safe side, we choose $\Delta t_S = \Delta t - 1$ ms. As for the laser trigger, we select a warm up time of 8 ms and thus $t_L = t_1 - 8$ ms as starting point. To avoid the illumination of the CCD during the readout process, we pick $\Delta t_L = \Delta t + 8$ ms for the length of the laser pulse. The acquisition window is thus opened by the spectrometer trigger $t_S = t_1$ and closed by the laser trigger $t_L + \Delta t_L = \Delta t + 8$ ms, as shown in Fig. 3.13.

4. Direct determination of the electron effective mass of GaAsN

Cyclotron resonance (CR) absorption spectroscopy is a powerful method to investigate electrical properties of semiconductor materials. In particular, it is the most direct method for electron effective mass determination and allows to study the mobility and relaxation times of free carriers inside a system. Even though different experimental techniques have been applied on GaAsN in order to determine the electron effective mass, no direct method has ever been used. We perform a systematic CR absorption spectroscopy study on a series of GaAsN alloys with different nitrogen concentrations for the first time. Our goal is to determine the electron effective masses in dependence of the N content. Moreover, we want to resolve the long-standing controversy (see Sec. 4.1). In this chapter, a review of former results is provided in the first section. The second section is dedicated to our electron effective mass study via CR absorption spectroscopy. An energy dependent analysis of the electron effective mass is presented in section three. The electron mobility drop of nitrogen containing samples is investigated in the fourth section. The results are discussed and summarized in section five. Parts of this chapter were published previously in Ref. [45].

4.1. Review of former results

Because of a significant difference in the size and electronegativity of nitrogen and arsenide atoms in GaAsN, the system has several characteristic properties. In particular, GaAsN exhibits a huge band gap bowing [18], a drop in the electron mobility [110] and a reduced pressure dependence of the band gap [136]. Different theoretical models which describe these features of GaAsN are presented in Chap. 2. It is possible to explain the band gap reduction and its pressure dependence within the band

anticrossing (BAC) model [136, 166], which is introduced in Sec. 2.3. The effective mass is also calculated in the framework of the BAC model [165] in Sec. 2.3.2. The BAC electron effective mass m_{BAC}^* smoothly increases with the N content x . A similar behavior of the electron effective mass up to 1.5% of nitrogen was found with an empirical tight-binding model by Shtinkov et al. [141]. Lindsay and O'Reilly [94] proposed a unification of the BAC model and the empirical pseudopotential method,

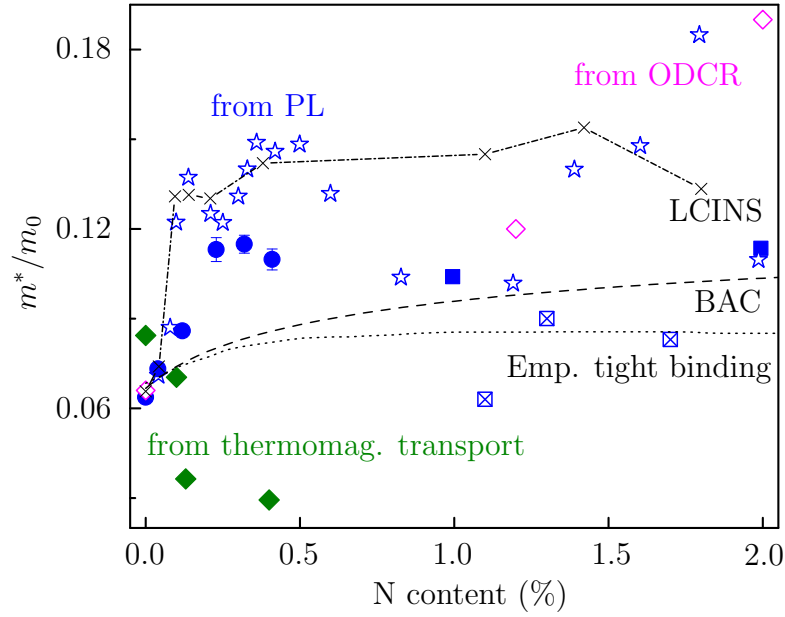


Figure 4.1.: Overview of different indirect experimental and theoretical results of the electron effective mass m^* in $\text{GaAs}_{1-x}\text{N}_x$. Calculations based on the BAC model [136, 165] are shown with a dashed line. The empirical tight-binding [141] and the LCINS model [94] calculations are presented with a dotted and dash-dotted line, respectively. PL and magneto-PL results are shown in blue with circles [2], stars [101], full squares [142] and empty squares [161]. Pink diamonds represent ODCR results [55] and the green full diamonds stand for thermomagnetic transport measurements [169].

which is in the focus of Sec. 2.5. They predicted a strong increase of the electron effective mass for $x \leq 0.1\%$, followed by a non-monotonic composition dependence for bigger N contents due to N-clustering. Besides different theoretical predictions, different experimental approaches have been applied on GaAsN in order to determine the electron effective mass. In the past, photoluminescence (PL) and magneto-PL

have been the most popular methods. This includes the publication of Skierbiszewski et al. on GaAs_{1-x}N_x/GaAs quantum well (QW) samples with $0.9\% \leq x \leq 4\%$ [142]. A smooth increase of the mass with nitrogen content was observed. Masia et al. [101] and Alberi et al. [2] used magneto-PL on GaAs_{1-x}N_x films. However, they found a steep increase of m^* with nitrogen content below the concentration limit of $x = 0.2\%$. For higher nitrogen contents, the results diverge. The electron effective mass decreases in case of Alberi et al. [2] and shows a non-monotonic compositional dependence in case of Masia et al. [101] above 0.2%. The latter is consistent with the LCINS model by Lindsay and O'Reilly [94]. Besides PL and magneto-PL, other techniques also provided contradicting results. A steep increase of m^* with N content was found with optically detected cyclotron resonance (ODCR) in GaAsN/GaAs QWs with a nitrogen concentration of 1.2% and 2% [55]. This method detects microwave-induced photoluminescence changes versus magnetic field and should not be mistaken for the direct cyclotron resonance absorption spectroscopy, which is introduced in Sec. 3.1. The decrease of the electron effective mass with increasing nitrogen content was also observed e.g. with a transport technique [169]. Fig. 4.1 illustrates the discrepancy between the different experimental results and theoretical calculations of the electron effective mass. However, cyclotron resonance absorption spectroscopy has never been applied before on GaAsN bulk material for effective mass determination.

4.2. Electron effective mass determination

We investigate the electron effective mass in epitaxially grown GaAsN:Si samples with low nitrogen concentrations of 0%, 0.1% and 0.2%. The samples were grown on a semi-insulating GaAs substrate by molecular beam epitaxy at a lowered growth temperature of 500° C. A detailed overview of the investigated samples is given in the appendix A.1. THz cyclotron resonance spectroscopy is measured in Faraday geometry with the free-electron laser FELBE at the Dresden High Magnetic Field Laboratory. Some experiments are carried out with a quantum cascade laser with 17.7 ± 0.5 meV. A Ge:Ga detector is used on the detection side. A detailed description of the experimental setup can be found in Sec. 3.1.4.

Cyclotron resonance is compared to impurity-shifted cyclotron resonance in the first part of this section. Furthermore, the impact of artifacts is discussed. Our THz

cyclotron resonance spectroscopy results are presented exemplarily for 41 meV in the second part on this section. The impact of nitrogen is studied.

4.2.1. Cyclotron resonance, impurity-shifted cyclotron resonance and the impact of artifacts

In general, CR occurs at a certain resonant magnetic field B_{res} , as shown in Sec. 3.1. Free carriers resonantly absorb the THz radiation of a certain frequency at this magnetic field. Analyzing the intensity of the transmitted THz radiation gives direct access to B_{res} , which corresponds to the lowest position of the transmission curve. At

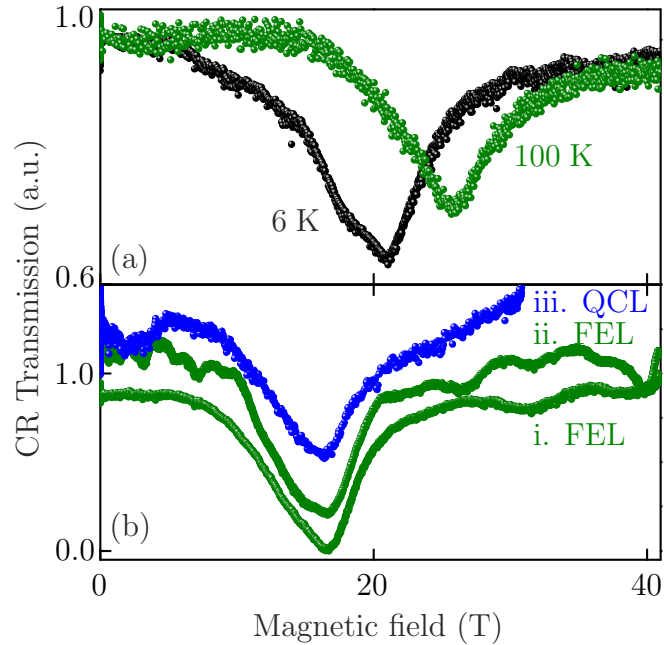


Figure 4.2.: Normalized CR transmission spectra with a photon energy of (a) 41.4 ± 0.5 meV and (b) 26.7 ± 0.5 meV at 100 K. (a) CR (green) and ICR (black) of our reference sample taken at 6 K and 100 K, respectively. (b) The sweep-up (i) and sweep-down (ii) signals of the FEL measurement are shown in green. The QCL curve (iii) is represented in blue. Fig. 4.2 (a) was previously published in Ref. [45].

low temperatures, a similar phenomenon appears in moderately doped samples and should not be mistaken for CR. Hydrogen-like impurity transitions occur between the $1s$ ground state and the $2p_+$ excited state at a certain resonant magnetic field $B_{\text{res}}^{\text{ICR}}$,

caused by carrier freeze-out [6, 106, 68, 171]. This effect is called impurity-shifted cyclotron resonance (ICR) and takes place at lower resonant magnetic fields than the CR of free carriers, as shown in Fig. 4.2 (a). We perform our experiments at 100 K in order to ionize the impurities and to be able to observe CR of free carriers and the CR electron effective mass with

$$m^* = \frac{e}{\omega_{\text{FEL}}} B_{\text{res}}. \quad (4.1)$$

The distinction between the real CR signal and possible overlapping mechanical noise is a major issue of the data analysis in case of the FEL measurements. In fact, the coil undergoes a mechanical and thermal shock during the magnetic pulse, which leads to vibrations of the magnet and affects the coupling of the FEL radiation. Fig. 4.2 (b) shows artifacts due to these oscillations, which are more pronounced in later times of the sweep-down (ii) signal. QCL measurements are not affected, because both laser and detector are installed inside the measuring probe (see Sec. 3.1.4). Comparing the sweep-up and sweep-down signals of one magnetic pulse is a reliable method to distinguish between the real signal and artifacts. Only the peak at 16.6 T in Fig. 4.2 (b) can be associated with CR absorption.

4.2.2. THz CR absorption spectroscopy in GaAsN

CR transmission spectra of GaAsN samples with different N contents are shown in Fig. 4.3 exemplarily for a FEL photon energy of 41.4 ± 0.5 meV. The second minimum at ≈ 45 T in (b) is one of the mentioned artifacts that originates from mechanical vibrations. Only the main minimum at approximately 25 T is related to the real CR signal. As the N content increases to 0.2%, B_{res} shifts only slightly to a higher magnetic field in (c). Consequently, the electron effective mass is not significantly affected by nitrogen content up to $x = 0.2\%$, as can be seen with Eq. (4.1). The transmitted THz radiation intensity T can be described with the Beer-Lambert law as

$$\frac{T}{T_0} = \frac{(1 - R)^2}{T_0} e^{-\alpha d} = \frac{(1 - R)^2}{T_0} \exp\left(-\frac{\Re(\sigma_{xx})}{\varepsilon_0 c n_1} d\right), \quad (4.2)$$

with the reflectivity R , the intensity of the incident THz radiation T_0 , the absorption coefficient α , the thickness of the active layer d , the vacuum permittivity ε_0 and

the refractive index $n_1(\omega)$. Eq. (2.31) is used for the CR absorption coefficient α of linearly polarized radiation in Eq. (4.2), which is introduced in Sec. 2.6.1. This classical description of the CR absorption is applied as a fitting function to our experimental results and is shown with red curves in Fig. 4.3. Eq. (4.2) gives direct

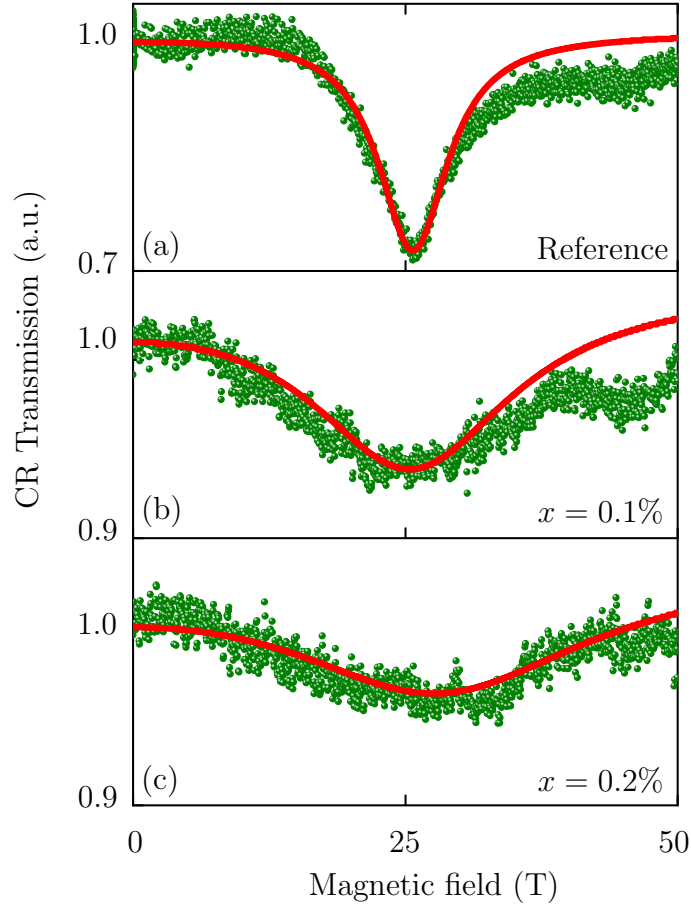


Figure 4.3.: CR transmission spectra of GaAs_{1-x}N_x samples with (a) $x = 0\%$, (b) $x = 0.1\%$ and (c) $x = 0.2\%$ taken with a FEL photon energy of 41.4 ± 0.5 meV at 100 K. Green bullets represent the experimental results and the red line is a classical CR absorption fit to the data using Eq. (4.2). The artifact at ≈ 45 T in (b) can be associated with mechanical noise. This figure was previously published in Ref. [45].

access to the carrier density n , the scattering time τ , the cyclotron frequency ω_c and thus the electron effective mass m^* . Fitting parameters are summarized in Tab. 4.1. The electron effective mass indeed only increases from $0.071m_e$ to $0.08m_e$ when the nitrogen content rises from $x = 0\%$ to $x = 0.2\%$ in GaAs_{1-x}N_x:Si.

4.3. Energy dependence of the effective mass

In order to study the energy dependence of the electron effective mass m^* , we perform CR spectroscopy experiments with different photon energies around the Reststrahlen band of GaAs. In the first part of this section, the Reststrahlen band is briefly presented in GaAs and GaAsN. CR spectra are shown in the second part. The increase of the electron effective mass and nonparabolicity with N content is discussed in part three.

4.3.1. Reststrahlen effect in GaAs and GaAsN

The Reststrahlen band is defined as the region between the transverse and longitudinal optical phonon frequencies at $k = 0$. A semiconductor almost totally reflects radiation that lies inside the electromagnetic spectrum of this band. In case of GaAs and GaAsN, the Reststrahlen band can be found between 33.3 meV and 36.8 meV, as

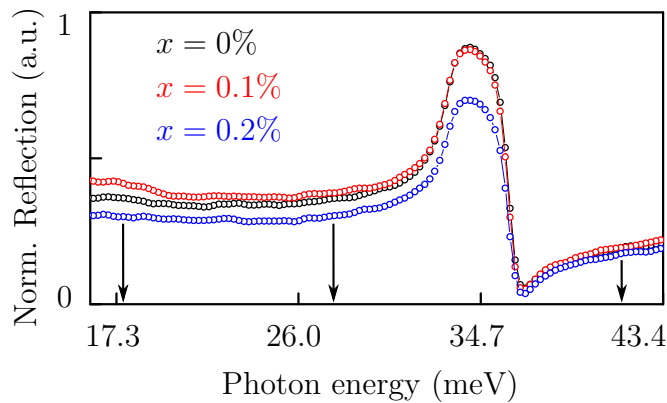


Figure 4.4.: Normalized room-temperature Fourier transform infrared spectroscopy reflection spectra of GaAsN with different N content x . All samples exhibit a region of high reflection in the typical Reststrahlen band (33.3 – 36.8) meV of GaAs. Vertical arrows indicate the photon energies of the performed CR absorption experiments, which lie outside of this area.

shown in Fig. 4.4. We choose photon energies with a minimal characteristic reflection for our CR measurements, namely 17.7 meV, 26.7 meV and 41.4 meV. These energies are indicated with vertical arrows in Fig. 4.4. The corresponding CR transmission spectra are shown in Fig. 4.3 (41.4 ± 0.5 meV) and Fig. 4.5 (26.7 ± 0.5 meV and 17.7 ± 0.5 meV).

4.3.2. CR spectroscopy with different photon energies

The comparison of the CR profiles in Figs. 4.5 (a) - (c) and 4.5 (d) - (f) indicates once again that m^* is not significantly affected by the nitrogen content up to $x = 0.2\%$ in agreement with the 41.4 ± 0.5 meV measurement. The fitting results support this

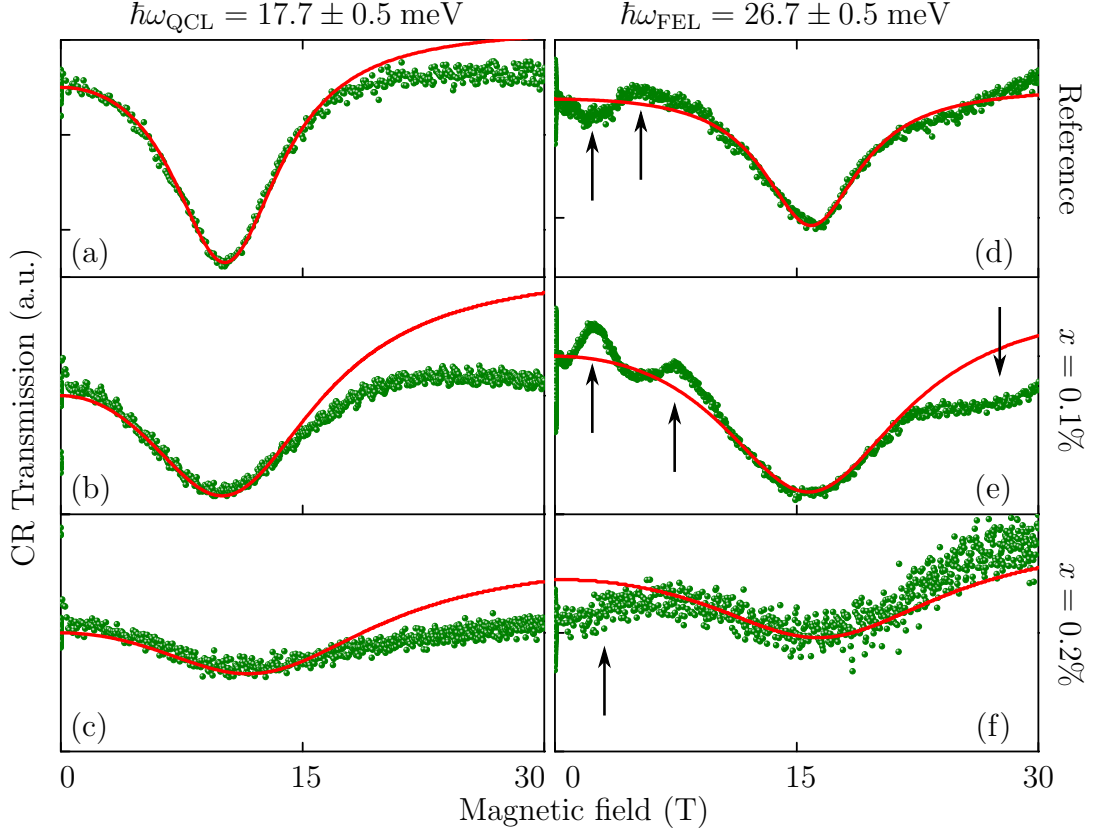


Figure 4.5.: CR transmission spectra of $\text{GaAs}_{1-x}\text{N}_x$ with a QCL photon energy of 17.7 ± 0.5 meV (left panel) and a FEL photon energy of 26.7 ± 0.5 meV (right panel). (a) and (d) show the reference sample with $x = 0\%$, (b) and (e) represent the $x = 0.1\%$ sample and (c) and (f) indicate the 0.2% sample. Green bullets originate from experimental results and the red line stands for the classical CR fit with Eq. (4.2). Artifacts due to mechanical vibrations are highlighted with vertical arrows.

observation, as presented in Tab. 4.1. The effective mass of the reference sample is $0.067m_e$ ($0.069m_e$) and increases to $0.069m_e$ ($0.072m_e$) in case of the $x = 0.2\%$ sample for 17.7 ± 0.5 meV (26.7 ± 0.5 meV). These results also imply a small nonparabolicity increase with nitrogen content, which is further investigated in the following.

Table 4.1.: Fit results for CR electron effective masses m^* , relaxation times τ and mobilities μ , which are determined with Eq. (4.2). The underlying CR absorption spectroscopy study is performed with the photon energies 17.7 ± 0.5 meV, 26.7 ± 0.5 meV and 41.4 ± 0.5 meV. This table was previously published in Ref. [45].

N content	$h\omega_{\text{QCL}} = 17.7 \pm 0.5$ meV			$h\omega_{\text{FEL}} = 26.7 \pm 0.5$ meV		
	0%	0.1%	0.2%	0%	0.1%	0.2%
$m^* (m_0)$	0.067 ± 0.002	0.067 ± 0.003	0.069 ± 0.007	0.069 ± 0.001	0.069 ± 0.002	0.072 ± 0.004
τ (fs)	100 ± 20	68 ± 11	43 ± 31	114 ± 10	59 ± 10	45 ± 20
μ (cm ² /Vs)	2800 ± 600	1500 ± 300	1100 ± 400	2900 ± 200	1500 ± 200	1100 ± 400
	$h\omega_{\text{FEL}} = 41.4 \pm 0.5$ meV					
	0%	0.1%	0.2%			
	0.071 ± 0.001	0.072 ± 0.003	0.08 ± 0.005			
	110 ± 15	36 ± 11	36 ± 10			
	2800 ± 200	900 ± 100	600 ± 200			

4.3.3. Increase of the electron effective mass and band nonparabolicity with N content

Figs. 4.6 (a) - (c) show the energy dependence of the electron effective mass in the range of the investigated photon energies. The triangles represent fit results of the electron effective masses, which are summarized in Tab. 4.1. Comparing (a) with (b) and (c) elucidates a moderate increase of m^* in the investigated energy range. For a quantitative analysis, we calculate the energy dependence of the momentum effective mass

$$m^*(k) = \hbar^2 k \left| \frac{d}{dk} \frac{1}{2} \left[(E_{\mathbf{k}}^c(k) + E^d) - \sqrt{(E_{\mathbf{k}}^c(k) - E^d)^2 + 4V^2 x} \right] \right|^{-1}, \quad (4.3)$$

which was introduced in Eq. (2.19) [147, 170]. We use the BAC model [136] for the energy dispersion of the lowest CB $E_-(k)$ of GaAsN, which is presented in Eq. (2.7). In analogy to Sec. 2.3.1, $E_{\mathbf{k}}^c(k)$ describes the unperturbed GaAs CB and $E^d = E_{\mathbf{k}}^c(0) + 0.23$ eV = 1.732 eV depicts the energy of the nitrogen level. Both are defined relative to the top of the valence band for 100 K. The interaction term is once

again $V = 2.7$ eV [157]. In Sec. 2.3.2, the momentum masses are obtained for $k = 0$. In the current approach, we want to investigate particularly the k -dependence of the momentum effective mass. This can be realized with two different treatments of the GaAs energy dispersion $E_{\mathbf{k}}^c(k)$. First, we assume that the CB of GaAs is perfectly

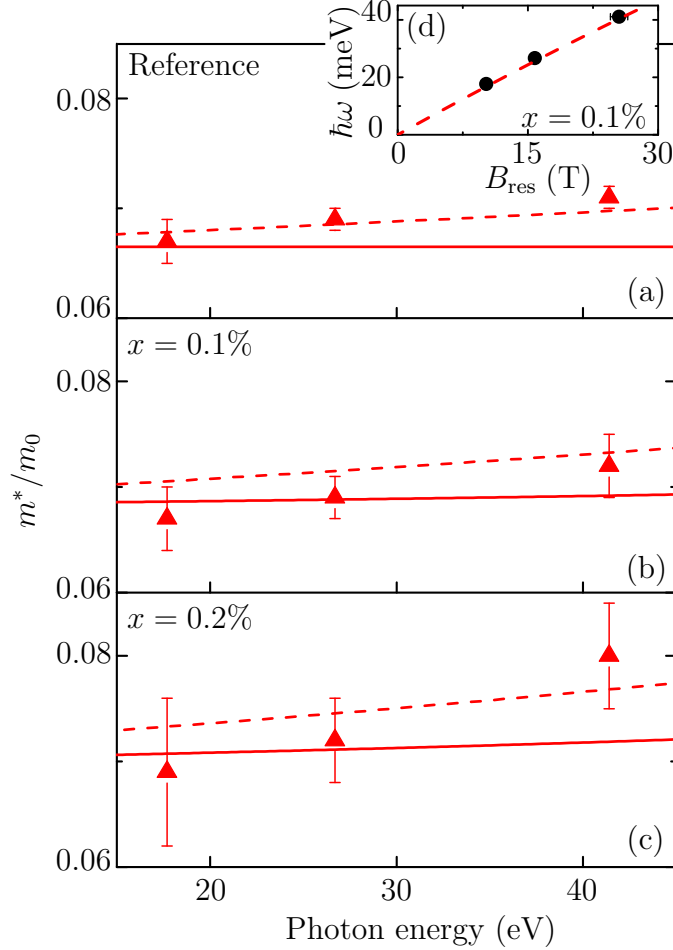


Figure 4.6.: Energy dependence of the electron effective mass of $\text{GaAs}_{1-x}\text{N}_x$ with (a) $x = 0\%$, (b) $x = 0.1\%$ and (c) $x = 0.2\%$. CR electron effective masses are determined for different photon energies and shown as triangles. Momentum masses [147, 170] are calculated with Eq. (4.3) using the BAC model [136] for the lowest CB $E_-(k)$ of GaAsN. The CB of GaAs is treated in the parabolic approximation (solid lines) and with a $k \cdot p$ approximation for the nonparabolicity (dashed lines). The inset (d) depicts B_{res} in dependence of the photon energy for $x = 0.1\%$. The experimental values are represented by circles and the BAC fit is shown as a dashed line. This figure was previously published in Ref. [45].

parabolic. The calculated values are shown in Fig. 4.6 by a solid line. In the second approach, we use a $k \cdot p$ approximation [19] with

$$E_{\mathbf{k}}^c(k) \cong \frac{\hbar^2 k^2}{2m_{\text{GaAs}}^*} - \frac{0.824}{E_0^c} \left(\frac{\hbar^2 k^2}{2m_{\text{GaAs}}^*} \right)^2 \quad (4.4)$$

in order to describe the band nonparabolicity with a small negative nonparabolicity coefficient -0.824 . The calculation is illustrated in Fig. 4.6 by a dashed line. The experimental cyclotron masses can be well described by the calculated BAC momentum masses using the $k \cdot p$ approximation method. The observed increase of the nonparabolicity with increasing nitrogen content is also depicted by the second treatment. However, the nonparabolicity is relatively small in the shown energy range. This is why we obtain an almost perfectly linear behavior of B_{res} in the inset (d) of Fig. 4.6, which can be well described by the BAC model (dashed line) [136] as well. In the proximity of the nitrogen impurity level ($\hbar\omega > E_0^c + 100$ meV), the nonparabolicity is expected to increase significantly. Nevertheless, the experimentally observed CR effective mass and band nonparabolicity increase can be well explained in the framework of the BAC model.

4.4. Mobility drop with increasing N content

The line broadening of the CR transmission curves in Fig. 4.3 (b) - (c) is probably the most striking feature. A tremendous mobility loss in nitrogen containing systems causes this characteristic behavior, which is accompanied by a decrease in relaxation time τ . The CR mobilities can be deduced from the CR transmission curve fits with Eq. (2.31), Eq. (4.2) and

$$\mu = \frac{e\tau}{m^*}. \quad (4.5)$$

The fit results are summarized in Tab. 4.1 and shown in Fig. 4.7 by red triangles. The determined values are in a good agreement with Hall mobilities [119], which are shown with blue diamonds. Both CR and Hall measurements are performed on the same sample set at 100 K. However, Hall measurements have a weaker sensitivity to forward-scattering [35] in comparison to CR spectroscopy and yield slightly higher mobility values. Furthermore, tight-binding calculations [46] and Anderson's many-impurity model calculations [155] were used for theoretical predictions of the mobility

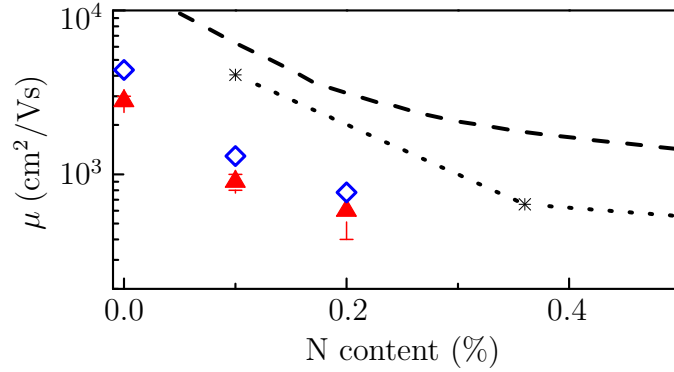


Figure 4.7.: Mobility decrease of GaAsN with increasing N content. Red triangles and blue diamonds represent CR and Hall [119] mobilities, respectively. The dashed and dotted lines illustrate mobility calculations by Ref. [155] and Ref. [46], respectively, for n-doped (10^{17} cm^{-3}) GaAsN at room temperature. The shown CR mobilities are taken at $41.4 \pm 0.5 \text{ meV}$ and 100 K and Hall measurements were performed on the same samples at 100 K [119]. This figure was previously published in Ref. [45].

and are shown in Fig. 4.7 by a dotted and dashed line, respectively. The theoretical values are much higher than the experimentally observed ones. This is due to the neglect of several possible scattering mechanisms in the calculation procedure. Even though N related alloy scattering can be recognized as the main scattering mechanism, scattering by interstitial nitrogen atoms, ionized impurities (neglected by Ref. [46]) or NN-clusters (neglected by Ref. [155]) have also to be considered. The mobility might be further diminished by additional structural defects in samples grown at 500 K (see App. A.1).

4.5. Discussion and summary

Our cyclotron resonance (CR) absorption spectroscopy study shows a moderate increase of the electron effective mass in GaAsN samples with a low nitrogen content. This result is in agreement with the band anticrossing (BAC) model [136, 165] and empirical tight-binding [141] calculations, as can be seen in Fig. 4.8. Magneto-photoluminescence (magneto-PL) investigations [2, 101] on the other hand, yield much higher mass values (see blue symbols in Fig. 4.8), which are to some extent consistent with the linear combination of isolated nitrogen states (LCINS) model [94].

As the name suggests, the LCINS model prioritizes cluster formation and predicts a tremendous impact of these structures on the effective mass. This issue is in the focus of Sec. 2.5 and the calculated LCINS masses are also shown in Fig. 4.8. At the same time, photoluminescence is very sensitive to carrier localization by disorder effects and clusters, which explains the agreement between LCINS masses [94] and magneto-PL masses [101]. CR is only sensitive to delocalized states and thus in agreement with models that neglect cluster formation, namely BAC [136, 165] and empirical tight-binding [141]. Consequently, CR probes delocalized states and measures the average mass at the Fermi energy whereas magneto-PL is dominated by emission from localized states in regions with higher N. This explains the difference between our CR absorption and other magneto-PL results. The CR effective masses are the relevant ones for transport and electronics. The utilization of different indirect methods [101, 2, 142, 161, 55, 169] with different sensitivity to carrier localization effects is responsible for the discrepancy.

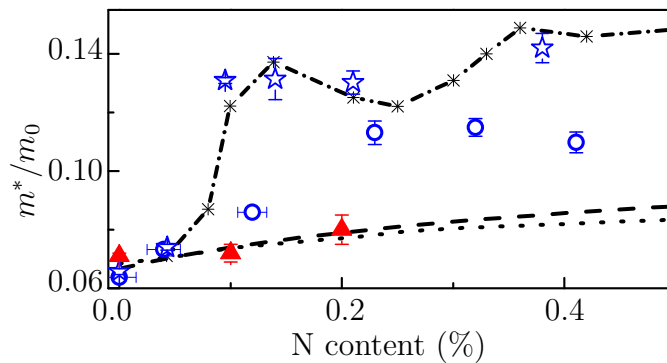


Figure 4.8.: Impact of increasing N content on the electron effective mass. Cyclotron resonance effective masses (triangles) are compared with calculations based on the band anticrossing model [136, 165] (dashed line), the empirical tight-binding [141] (dotted line) and the LCINS model [94] calculations (dash-dotted line). Magneto-photoluminescence results on m^* are shown with circles [2] and stars [101], respectively. The cyclotron resonance effective masses are taken at 41.4 ± 0.5 meV and 100 K. This figure was previously published in Ref. [45].

In summary, we performed detailed cyclotron resonance (CR) absorption spectroscopy investigations in bulk silicon doped GaAsN samples with low nitrogen concentrations. We used the unique combination of the large-scale facilities free-electron laser FELBE and the Dresden High Magnetic Field Laboratory for our THz

spectroscopy study in pulsed magnetic fields up to 62 T. A slight increase of the CR electron effective mass with N content is observed, which is in excellent agreement with calculations based on the band anticrossing (BAC) model [136, 165] and the empirical tight-binding predictions [141]. The band nonparabolicity increases with increasing N concentration. Our calculations of the energy dependent momentum effective mass [147, 170] based on the BAC model [136] and a $k \cdot p$ approximation of the GaAs conduction band [19] deliver results in good agreement with the experimentally observed values. The electron mobility strongly decreases in nitrogen containing samples and matches the decrease of Hall mobilities [119]. Deviations between different results [101, 2, 142, 161, 55, 169] on the electron effective mass in GaAsN are explained with the utilization of different indirect methods and different sensitivity to carrier localization effects. The consideration of N clustering is also responsible for different theoretical predictions [165, 141, 94].

5. Photoluminescence study of GaAsN and GaAsN:Si

Photoluminescence (PL) is a very powerful method to investigate optical properties of semiconductor materials near the band edge. We use continuous-wave (cw) and time-resolved PL in order to study optical transitions and the recombination dynamics of different GaAsN samples. The experimental setup is introduced in Sec. 3.2. Our sample series consists of Si-doped GaAsN samples with various N content and is named VN-series. The same series is used for our cyclotron resonance study in Chap. 4. It was grown by molecular beam epitaxy (MBE) at the University of Sheffield by M. Hopkinson and coworkers. Furthermore, we investigate two intrinsic GaAsN samples with a nitrogen concentration of 0.095% (K105) and 0.21% (K106), respectively. The K-samples were grown by metalorganic vapour phase epitaxy (MOVPE) by W. Stolz and coworkers at the Philipps-Universität Marburg [77]. An overview of all investigated samples is provided in appendix A.1. The physical principle of PL spectroscopy is introduced in the first part of this chapter. Luminescence processes in crystalline semiconductors are discussed very generally and then particularly for GaAs. Low-temperature PL spectra of all investigated samples are shown in the second part. The impact of nitrogen and silicon is studied with temperature- and power-dependent PL-series. The last section is dedicated to the recombination dynamics. Time-resolved PL measurements on Si-doped GaAsN samples are presented.

5.1. Photoluminescence spectroscopy

Every semiconductor can be optically, thermally or electrically pumped to an excited state. After a certain time, the so-called lifetime, the system relaxes back to its ground state. The surplus energy is released via radiative or non-radiative channels.

Photoluminescence spectroscopy analyzes the radiative part of the emission in case of an optical excitation. In analogy to that, electroluminescence and thermoluminescence can be applied after electrical and thermal excitation, respectively. In case of a non-resonant excitation above the band edge of a direct semiconductor, an electron-hole pair is created in the conduction and valence band (VB). Both particles relax very fast towards the minimum of the particular band by phonon emission. The subsequent radiative recombination strongly depends on the material properties and the number of excited electrons (holes) per unit area, also known as excitation density. Different luminescence processes in crystalline semiconductors are presented below.

5.1.1. Luminescence processes in crystalline semiconductors

A simplified overview of possible luminescence processes for a weak continuous-wave excitation ($0.01 - 10 \text{ W/cm}^2$) is given in Fig. 5.1 [121]. The band-to-band transition (e-h) represents the simplest case. The emitted photon energy $h\nu = E_g$ reveals the band gap energy E_g and is shown in Fig. 5.1 (a). A free exciton (FE) has a slightly smaller photon energy $h\nu = E_g - E_X$. The difference corresponds to the binding energy

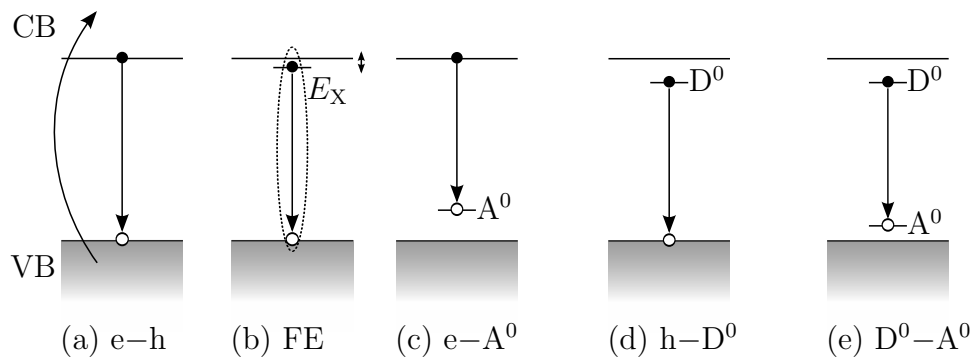


Figure 5.1.: Overview of luminescence processes in crystalline semiconductors: (a) band-to-band (e-h), (b) free exciton (FE), (c) free electron to a neutral acceptor (e- A^0), (d) free hole to a neutral donor (h- D^0) and (e) neutral donor to neutral acceptor (D^0-A^0).

E_X of the quasi-particle, as illustrated in 5.1 (b). The other processes in Fig. 5.1 have even smaller photon energies, which depend on the involved localization centers. For instance, the excited electron can recombine with a neutral acceptor A^0 , as shown in 5.1 (c). In analogy, radiative transitions can imply an exciton bound to a neutral

(A^0-X) or ionized acceptor (A^-X). Further possible recombination channels are a free hole with a neutral donor ($h-D^0$) (see Fig. 5.1 (d)), an exciton bound to a neutral (D^0-X) or ionized donor (D^+X), and a donor-acceptor pair transition (D^0-A^0), as shown in Fig. 5.1 (e). Excitons can be also bound to a variety of impurities, caused by alloy fluctuations, lattice or point defects, vacancies, clusters etc. PL spectra of highly disturbed systems like GaAsN usually contain a variety of different contributions. The transitions appear as sharp PL peaks [135, 99, 139, 103, 82] or blend into a broad asymmetrical PL profile [51, 26, 29, 98], depending on the nitrogen content, sample quality and resolution. Diverse relaxation processes behave differently under varying temperature or illumination power and have different lifetimes. These characteristic properties can be used to analyze the PL spectrum and to investigate the origin of the peaks. Possible strategies are discussed below.

5.1.2. Photoluminescence of gallium arsenide

In order to understand the impact of nitrogen on GaAs, it is necessary to understand the PL spectrum of pure GaAs first, which is one of the best-known semiconductor systems. The same is valid for Si-doped GaAs. The first report on a MBE-grown GaAs with silicon doping was published by Cho and Hayashi [32]. Many photoluminescence investigations (e.g. [140, 126, 22, 111]) have followed in subsequent years. Silicon is an amphoteric dopant, which acts as a donor at the gallium site and as an acceptor at the arsenic site. Nevertheless, MBE-grown GaAs:Si behaves as n-type material in the doping range $1 \cdot 10^{15} - 5 \cdot 10^{18} \text{ cm}^{-3}$ [32]. Acting as a donor, Si forms a shallow impurity level with a binding energy of $\approx 6 \text{ meV}$ and increases the Fermi energy of GaAs. Fig. 5.2 shows a typical low-temperature PL spectrum of GaAs. It is obtained from our reference sample (VN463), which is doped with silicon to a level of nominally $1 \cdot 10^{17} \text{ cm}^{-3}$. The observed peaks are well-known from the literature and are discussed from top to bottom on the energy scale. The free exciton (FE) transition is located at the high-energy side of the spectrum. The recombination principle is illustrated in the inset. The observed transition corresponds to the dominant $n = 1$ state. Below the FE, small features can be found around 1.5 eV. These transitions are attributed to defect-induced localized excitons (LEs), involving carbon impurities [22]. Furthermore, three impurity-related transitions are resolved below in Fig. 5.2. (e,C^0) is the most consistent feature in the literature and can be associated with a

transition from the CB to the neutral acceptor carbon (C) [133, 7, 140, 111], as shown in the lower inset. Carbon has a ionization energy of ≈ 26 meV [7] in GaAs and is usually introduced into the system unintentionally during the growth process. The 1.491 eV peak originates from neutral donor to neutral acceptor transitions (D^0-A^0) [140, 111] and the 1.488 eV peak is identified as another transition from the CB to a neutral acceptor ($e-A^0$) [111]. The acceptor state can be formed by a gallium antisite

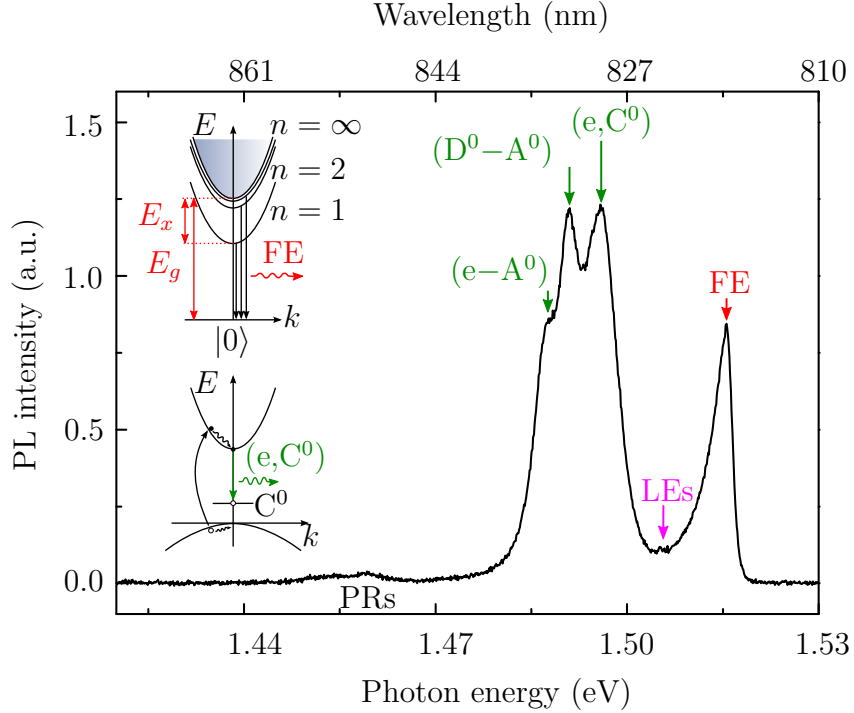


Figure 5.2.: Low-temperature PL of GaAs:Si. The experiment is performed with a frequency-doubled Nd:YAG laser at 4.5 K with an average power density of 1.15 W/cm^2 . The resolved peaks are labeled as in Sec. 5.1.1. The inset shows the principles of the free exciton (FE) and electron to neutral acceptor ($e-A^0$) transition.

defect and is not present in very pure semi-insulating GaAs films [150] or can be compensated by growth conditions [63]. Finally, phonon replicas (PR) are present at the low-energy side of the spectrum. In summary, the PL spectrum of GaAs:Si features all the identified transitions, known from undoped GaAs and no additional peaks from the doping. Thus, the PL spectrum of VN463 can act as a reference for both the Si-doped VN-series and the undoped K-series. In the following, the focus returns to GaAsN.

5.2. Radiative recombination in GaAsN alloys

GaAsN samples are characterized with cw PL spectroscopy using the measuring principle described in Sec. 3.2.1. Instead of a pulsed Ti:Sa laser, we utilize the frequency-doubled Nd:YAG laser in cw-mode and a spectrometer with a nitrogen cooled silicon CCD on the detection side. The Princeton Instruments detection unit is discussed in detail in Sec. 3.3.1. Fig. 5.3 shows the characteristic low-temperature cw PL spectra of n-doped GaAsN samples (VN-series) in (a) and undoped GaAsN samples

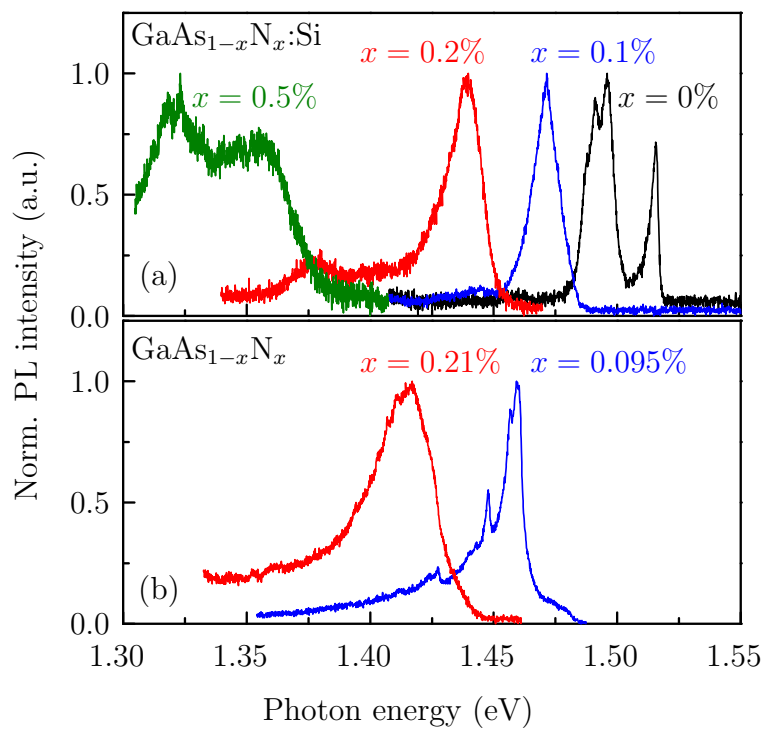


Figure 5.3.: Low-temperature PL of (a) the Si-doped and (b) intrinsic $\text{GaAs}_{1-x}\text{N}_x$ sample series with $x = 0\% - 0.5\%$. The experiment is performed at 4.5 K with an averaged power density in the range of $0.3 - 5.7 \text{ W/cm}^2$.

(K-series) in (b). The PL spectra illustrate several typical features of GaAsN. First of all, the main transition peaks systematically shift to lower energies when the nitrogen content is elevated. The observed red-shift of the PL indicates the typical band gap reduction of the dilute nitride and was discovered by Weyers et al. [162] in 1992. Many others (e.g. [51, 26, 16, 130]) have confirmed this observation in subsequent years. The red-shift is accompanied by a progressive line width broadening, which

indicates a reduced crystal quality of the N containing samples. This is especially valid in case of the $x = 0.5\%$ sample, which is consequently not part of the following investigations. Furthermore, the line shape significantly differs among the samples. In order to understand the impact of nitrogen on GaAs, very dilute GaAsN is compared to the N-free reference GaAs:Si in the first part of this section. The PL evolution with increasing N content is studied in the second part.

5.2.1. Radiative recombinations of GaAs_{1-x}N_x with $x = 0.095\%$

It is possible to distinguish between typical GaAs transitions (see Sec. 5.1.2) and N-induced features in luminescence spectra of very dilute GaAsN samples. Thus, we start the investigation with cw PL spectra of intrinsic GaAs_{1-x}N_x with $x = 0.095\%$ (K105), which are shown in Fig. 5.4. The temperature is elevated from 4.5 K (top spectrum) to 100 K (bottom spectrum). The solid line and blue area are taken with an average power density of 34 W/cm² and 6 W/cm², respectively. The low-temperature PL is dominated by an asymmetric spectrum with several distinct features, which are indicated by vertical lines. Increasing the temperature to 20 K does not crucially affect the line shape. A single peak arises at ≈ 1.48 eV in the 50 K spectrum and dominates the PL at 100 K. This peak is designated as FE/EHP in the figure and is discussed first.

Free exciton/electron-hole plasma transition: FE/EHP

The free exciton/electron-hole plasma (FE/EHP) peak has a high-energy tail and significantly red-shifts when the temperature is elevated. The power dependence of the transition is shown exemplarily for 50 K in Fig. 5.5 (a) on a double-logarithmic scale. The luminescence varies superlinearly with the excitation intensity, which is typical for intrinsic recombinations of electron-hole pairs or excitons [121]. The fit of the PL intensity

$$I_{\text{PL}} = c \cdot I_{\text{ex}}^k \quad (5.1)$$

shows that it depends almost quadratically ($k = 1.9$) on the excitation power I_{ex} . The full width at half maximum (FWHM) is presented in Fig. 5.5 (b). Its mean value corresponds to $1.2k_B T = 5.08$ meV. These observations prove that the 1.48 eV

peak originates from FEs or (e-h) transitions with contributions of the EHP on the high-energy side of the spectrum [121].

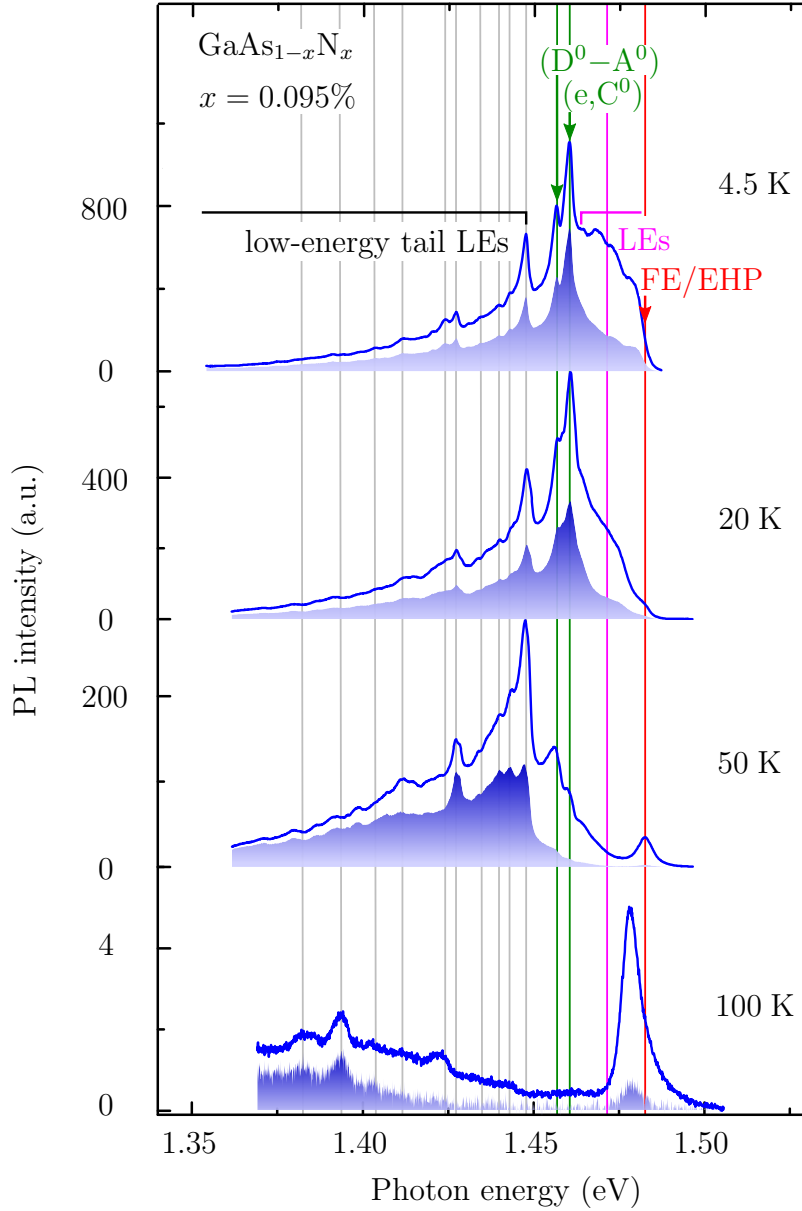


Figure 5.4.: Temperature series of intrinsic GaAs_{1-x}N_x with $x = 0.095\%$. The upper solid curves are taken at 34 W/cm^2 and the lower area corresponds to an average power density of 6 W/cm^2 (multiplied by 3). Grey vertical lines mark cluster features. Note the different scaling on the vertical axis.

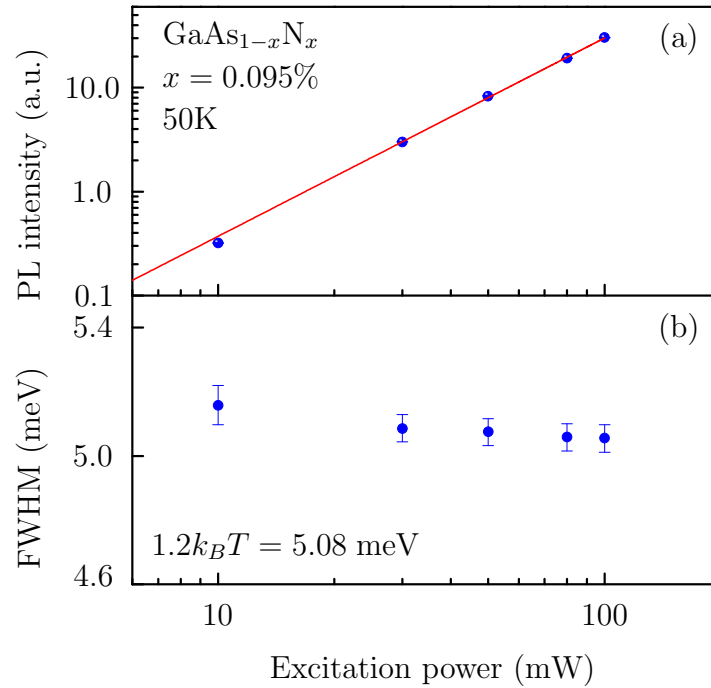


Figure 5.5.: Power dependence of the 1.48 eV peak in intrinsic GaAs_{1-x}N_x with $x = 0.095\%$ (K105) at 50 K. (a) PL intensity increases with excitation power. The blue circles indicate the experimental values and the red line shows the fit with Eq. (5.1). The FWHM is shown in (b). The blue circles result from a Gauss fit of the 1.48 eV peak.

GaAs related transitions: (e, C^0) and $(D^0 - A^0)$

Another peak appears 23 meV below the FE/EHP. Similarly to the reference, it dominates the low-temperature and low-power PL and is designated as a (e, C^0) transition [130]. The same is valid for the 1.457 eV peak, which is located 3.8 meV below (e, C^0) and thus connected with $(D^0 - A^0)$ transitions. Further transitions cannot be associated with GaAs (see Fig. 5.4 and Fig. 5.3) and must be related to the nitrogen incorporation.

Localized excitons on the high-energy side of the spectrum: LEs

The low-temperature PL is characterized by a broad spectral feature on the high-energy side, which is indicated by a pink vertical line. In analogy to the reference sample, it is associated with LEs. The FE/EHP transition emerges from a high-energy shoulder of this broad peak. The position of LEs indicates that the corresponding localization

centers lie just below the CB minimum. Their origin has been extensively studied in the past. Deep donor-like states were found mainly responsible for the localization in case of GaAsN and InGaAsN [84, 89, 82]. Alternatively, they were attributed to compositional fluctuations [26, 108, 103] in N content. Such fluctuations usually create regions with a locally reduced band gap and lead to PL emission at lower energies. Semiconductor quantum dots [108] usually exhibit a similar behavior. The observation of sharp distinct peaks in near-field spectroscopy [108, 103] of (In)GaAsN supports this interpretation. According to the empirical pseudopotential and the LCINS method (see Sec. 2.4 and Sec. 2.5), nitrogen pairs and clusters create localization potentials in the vicinity of the CB minimum E_- of GaAsN. Despite the different semantics, alloy fluctuations and nitrogen clusters both describe localization potentials due to a non-uniform N distribution [24].

Interexcitonic population transfer of LEs

LEs on the high-energy side of the spectrum exhibit a redistribution towards higher energies with increasing illumination power (see Fig. 5.4 at 4.5 K). This redistribution indicates that high-energy side LEs are efficiently transferred. The mechanism of this

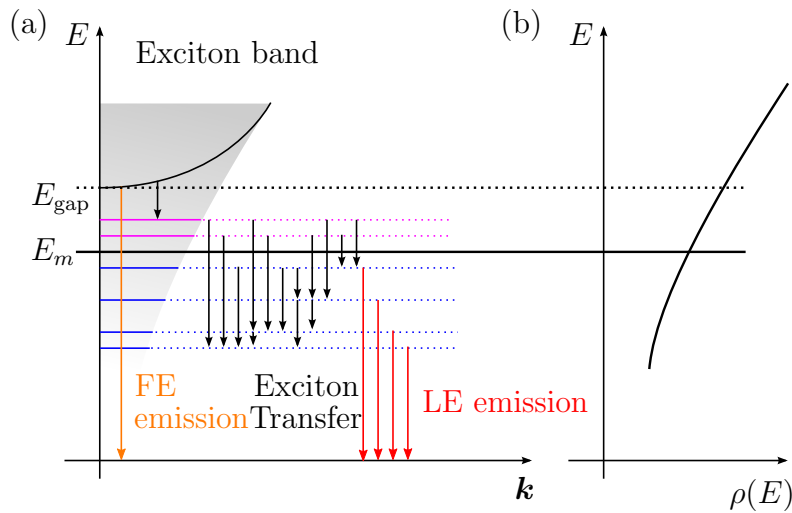


Figure 5.6.: Schematic representation of localized excitonic states and recombination processes after optical excitation of GaAsN. (a) E represents the energy of an excitonic state and (b) $\rho(E)$ is the density of localized states. The so-called mobility edge E_m corresponds to an energy with an equal recombination and transfer rate. The figure is adapted from Ref. [117].

interexcitonic population transfer is in the focus of this paragraph. In case of low temperatures and moderate excitation powers ($< \text{kW}/\text{cm}^2$), excitons are created in the system GaAsN after interband laser excitation. Fig. 5.6 illustrates possible subsequent recombination processes. As mentioned above, GaAsN has a variety of shallow cluster states just below the CB minimum (pink and blue horizontal lines). These localization centers can efficiently trap excitons. Thus, the luminescence largely consists of LE transitions (red arrows). Baranowski et al. proposed the so-called model of hopping excitons [11] in order to explain the observed behavior. According to this model, a trapped exciton can recombine radiatively (red arrow) or hop to another localization center (black arrow). This interexcitonic transfer (here exciton hopping) is realized by overlapping LE wave functions. At low temperatures, excitons preferentially hop several times to lower energies (exciton transfer) before they recombine. For a quantitative description of the hopping transport a characteristic energy E_m is introduced. This so-called mobility edge corresponds to an equal recombination and transfer rate [117]. The transfer dominates for $E > E_m$ and the recombination dominates for $E < E_m$. Raising the temperature pushes E_m to lower values and transfers excitons from localized into delocalized states. Simultaneously, the FE/EHP (orange arrow) transition emerges from the high-energy shoulder of the LE-band.

Low-energy tail-LEs

The low-energy tail of the PL is also characterized by LEs. The underlying states are associated with N clusters of higher binding energies [50] and thus of larger sizes [50, 112]. They can be attributed to deeper lying cluster states in Fig. 5.6 (a). Since the formation of similar-sized large clusters is less likely in very dilute GaAsN samples, the spatial overlap of cluster exciton wave functions decreases with cluster size [42, 3]. Consequently, low-energy tail-LEs are less efficiently transferred than those on the high-energy side. This is revealed by PL series at varied excitation power, shown in Fig. 5.4 and Fig. 5.7 (a). In contrast to high-energy LEs, tail-LEs exhibit no redistribution towards higher energies with increasing excitation power.

Temperature dependence of the PL

GaAs_{1-x}N_x with $x = 0.095\%$ behaves like GaAs with a small amount of impurities. The low-temperature PL is dominated by LEs and GaAs related transitions (e,C⁰)

and (D^0-A^0). High-energy LEs merge to a spectral band with an efficient population transfer. Tail-LEs are less efficiently transferred and gain spectral weight at higher temperatures ($T > 50$ K). They can be attributed to deeper lying cluster states in Fig. 5.6 (a). An enhanced thermal energy increases the contribution of non-radiative relaxation. High-energy LEs are more affected by these processes. Simultaneously, the FE/EHP peak appears on the high-energy side (ionization of LEs) and dominates the PL for $T \geq 100$ K.

5.2.2. PL evolution with increasing N content

The PL spectrum of $\text{GaAs}_{1-x}\text{N}_x$ with $x = 0.095\%$ exhibits a variety of distinct peaks. They can be attributed to both GaAs-like transitions and typical GaAsN cluster features. Increasing the N content to $x = 0.21\%$ dramatically changes the line-shape of the PL, as can be seen in Fig. 5.3 (b) and Fig. 5.7. Besides the well-understood red-shift (see Sec. 2.3), the distinct features of the $x = 0.095\%$ sample merge into a broad and asymmetric PL spectrum of $\text{GaAs}_{1-x}\text{N}_x$ with $x = 0.21\%$.

Formation of a LE-band

The number of different cluster states increases with increasing N content. These cluster states trap excitons after optical excitation and create numerous LEs with adjacent energetic positions. Because of the energetic proximity, distinct LE peaks cannot be resolved in undoped $\text{GaAs}_{1-x}\text{N}_x$ with $x = 0.21\%$ (K106) and a merged band of LEs evolves. Fig. 5.7 illustrates the formation of this so-called LE-band in K106. Vertical arrows mark the energy positions of the band gap E_g , which are determined with the BAC model [136]. The calculated energy is in excellent agreement with the FE/EHP shoulder of intrinsic $\text{GaAs}_{1-x}\text{N}_x$ with $x = 0.095\%$ (K105) in Fig. 5.7 (a). On the other hand, no PL feature is observed at E_g for K106 in Fig. 5.7 (b). The LE-band dominates the low-temperature PL for all applied power densities.

Partially delocalized character of the LE-band

The energetic proximity of individual LEs to each other affects the localization character of the LE-band. Fig. 5.7 illustrates a low-temperature PL series at varied excitation power of $\text{GaAs}_{1-x}\text{N}_x$ with (a) $x = 0.095\%$ and (b) $x = 0.21\%$. Equal

LEs contribute to the PL of both N-containing samples, as highlighted with gray vertical lines in the regions A - B. Thus, the energy of LEs is independent of the N content and the band gap energy. However, the LE-band exhibits a power-induced blue-shift in Fig. 5.7 (b), whereas the position of LEs (region B) remains fixed in

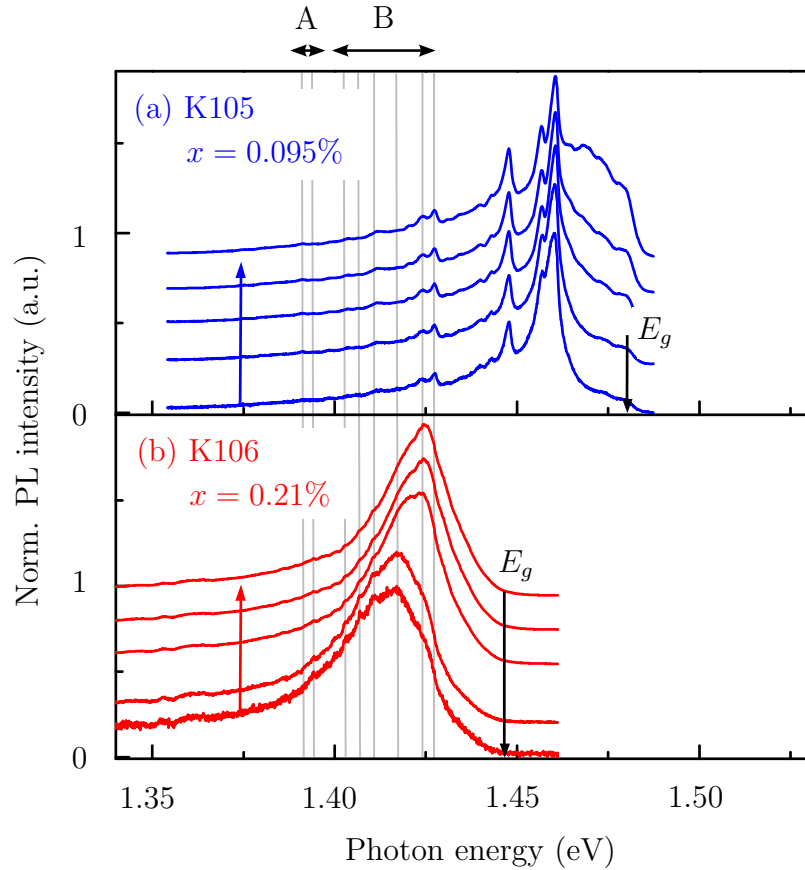


Figure 5.7.: Power series of intrinsic GaAs_{1-x}N_x with (a) $x = 0.095\%$ (K105) and (b) 0.21% (K106) taken at 4.5 K. The average power density is increased from 0.6 W/cm^2 to 34.4 W/cm^2 in (a) and from 5.7 W/cm^2 to 114.8 W/cm^2 in (b) from bottom to top. Vertical arrows indicate the band gap energy E_g according to the BAC model [136] for 0 K. Common cluster features of K105 and K106 are marked with vertical lines. The PL spectra for different pump intensities are shifted vertically for clarity.

Fig. 5.7 (a). Consequently, the LE-band has a higher degree of delocalization in comparison to the corresponding LEs in Fig. 5.7 (a). Besides the energetic proximity, the actual interexcitonic population transfer is most crucial (see Fig. 5.6). In particular, LE-bands differ from real delocalized transitions, like FEs. In contrast to the CB that

is composed of Bloch states and therefore features a well-defined dispersion relation, the LE-band is rather a fusion of discrete LEs with an efficient interexcitonic transfer. Consequently, the observed power-induced blue-shift of the LE-band is caused by

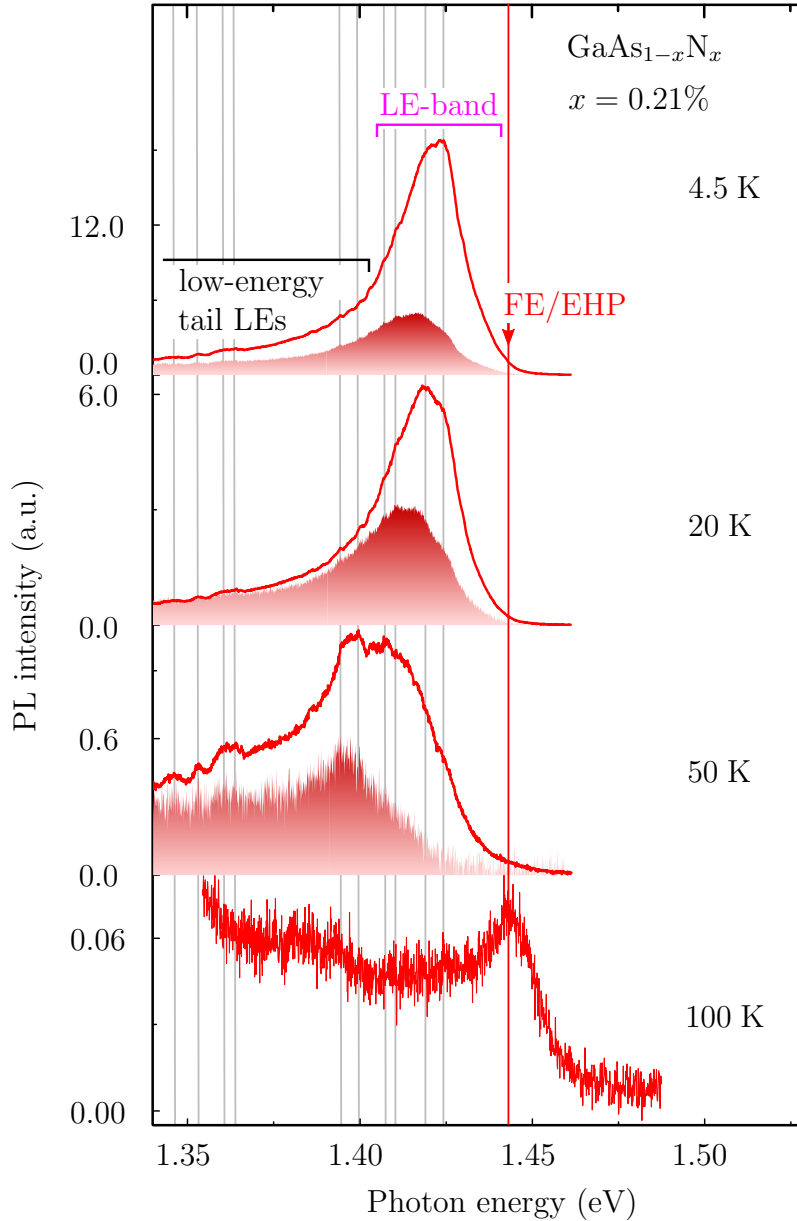


Figure 5.8.: Temperature series of GaAs_{1-x}N_x with $x = 0.21\%$. The upper solid curves are taken at 34 W/cm² and the lower area corresponds to an average power density of 6 W/cm² (multiplied by 10). Grey vertical lines mark cluster features. Note the different scaling on the vertical axis.

a redistribution towards higher LEs inside the LE-band: First of all, the amount of created excitons increases with illumination power. Subsequently, most of these excitons are captured by different cluster states (see Fig. 5.6). Since many cluster states are occupied simultaneously, the excitonic transfer towards lower lying cluster states is partially suppressed. Consequently, the LE-band maximum shifts to higher energies when the illumination power increases.

Activation of tail-LEs, FE/EHP and non-radiative relaxation channels

Besides the LE-band formation, GaAs_{1-x}N_x samples with higher N content behave similar to those with $x = 0.095\%$ (K105). Fig. 5.8 shows a temperature series of intrinsic GaAs_{1-x}N_x with $x = 0.21\%$ (K106). In analogy to Fig. 5.4, the solid line and red area are taken with an average power density of 34 W/cm² and 6 W/cm², respectively. The low-temperature PL is discussed above and applies equally to the 20 K case. The LE-band red-shifts at higher temperatures, which is characteristic for delocalized transitions. However, the underlying mechanism of the shift is not related to the typical band gap reduction. It results from a carrier redistribution [49] towards lower lying cluster states at higher temperatures. Tail-LEs dominate the PL spectrum at 50 K, especially at lower average power densities. Furthermore, non-radiative relaxation processes considerably decrease the radiation yield in comparison to the PL of intrinsic GaAs_{1-x}N_x with $x = 0.095\%$ (K105). Note that the decrease in PL intensity (factor 6 for temperature increase from 20 K to 50 K) is twice as large in K106 than observed for K105. This indicates that the increased lattice disorder results in a stronger contribution of non-radiative recombination channels. Simultaneously, the band gap related FE/EHP appears also in intrinsic GaAs_{1-x}N_x with $x = 0.21\%$ (K106) at 100 K. Lower lying cluster states contribute equally to the PL, as can be seen in the pronounced low-energy plateau. Furthermore, the (e,C⁰) and (D⁰-A⁰) transitions cannot be resolved anymore.

5.3. Luminescence of silicon-doped GaAsN

Our PL study reveals fascinating optical properties of GaAsN with increasing N content. GaAs-like transitions and typical cluster features are observed in the spectrum of intrinsic GaAs_{1-x}N_x with $x = 0.095\%$. When the N content is increased, the spectrum

merges to a broad and asymmetric band with a large set of LEs. These LEs exhibit an efficient interexcitonic population transfer. Consequently, the LE-band shows a partially delocalized character even though it comprises localized transitions. But how does silicon incorporation for n-type doping change the picture? Recombination processes of GaAsN:Si with low N content are studied in the first part of this section. They are compared to the processes of intrinsic GaAsN. A discussion on different LE-bands is presented in the second part.

5.3.1. Recombination processes in GaAsN:Si

Because of the nearly identical N content, n-type GaAs_{1-x}N_x samples with $x = 0.1\%$ (VN459) and $x = 0.2\%$ (VN460) are compared to undoped GaAs_{1-x}N_x with $x = 0.095\%$ (K105) and $x = 0.21\%$ (K106), respectively. An overview of all samples is provided in App. A.1. PL spectra of samples with a comparable N content are shown in Fig. 5.3 with the same color. Obviously, the K-series sample peaks are located at a lower photon energy as the corresponding VN-series sample peaks. This observation is not related to the small N content difference between the samples. Otherwise, the spectrum of the $x = 0.095\%$ sample would have to be blue-shifted with respect to the $x = 0.1\%$ one. Furthermore, the undoped samples show a more pronounced asymmetric line shape [26, 29] and low-energy tail in comparison to the Si-doped ones. In the first part of this subsection, the high-energy side of the peaks is in the focus. The low-energy tail is discussed in the second part.

Continuous-wave PL measurements are performed under the same conditions as in Sec. 5.2. Fig. 5.9 illustrates a temperature series of the Si-doped GaAs_{1-x}N_x with $x = 0.1\%$ (VN459). The solid lines and areas represent an average power density of 34 W/cm² and 6 W/cm², respectively. For comparison, the corresponding PL curves of the intrinsic GaAs_{1-x}N_x with $x = 0.095\%$ (K105) are shown with dotted lines. Besides the energy position, the line shape of VN459 shows similarities to the shape of the undoped GaAs_{1-x}N_x sample with $0.095\% < x \leq 0.21\%$. The low-temperature PL is dominated by a broad peak on the high-energy side.

“Localized” LE-band and the high-energy part of the luminescence

The energy position of the dominant PL peak suggests that a LE-band evolved from distinct LEs already at $x = 0.1\%$. This peak shows no signs of redistribution towards

higher states with illumination power increase, as observed in intrinsic GaAs_{1-x}N_x with $x = 0.095\%$ (K105) and $x = 0.21\%$ (K106) in Fig. 5.4 and Fig. 5.8, respectively.

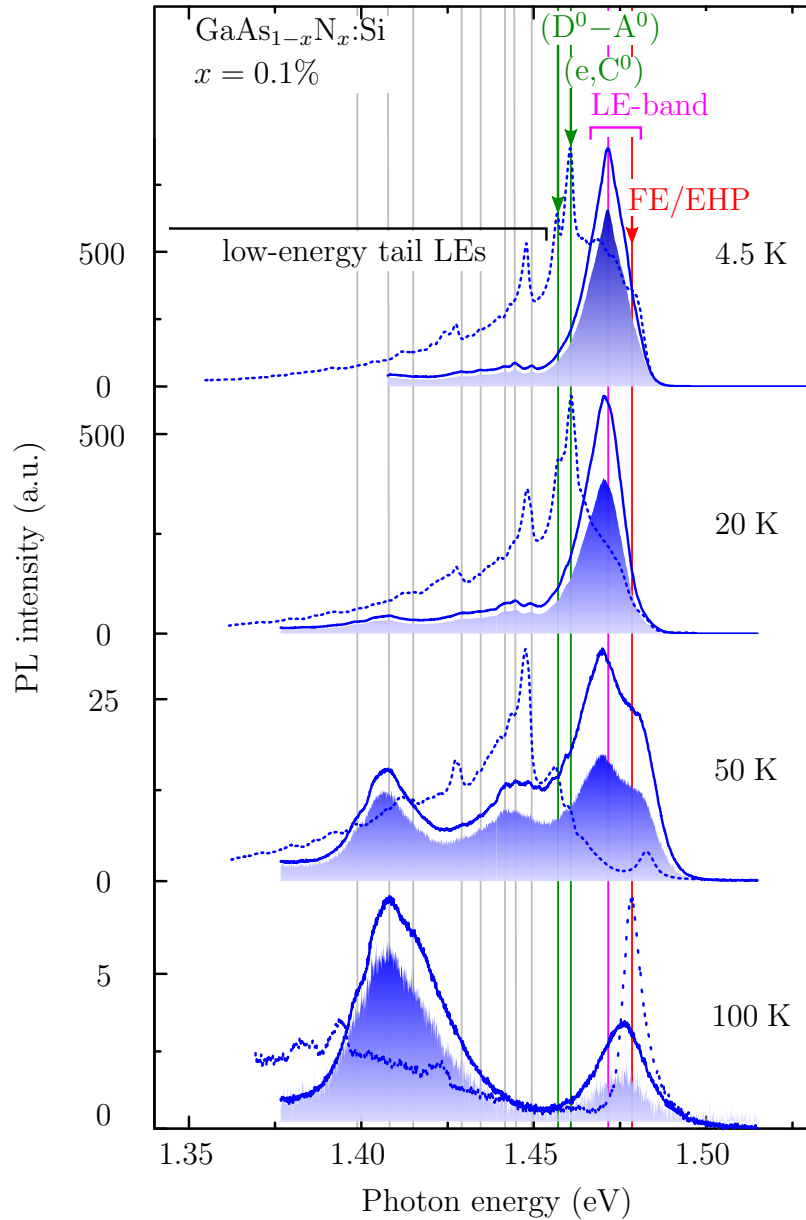


Figure 5.9.: Temperature series of the Si-doped GaAs_{0.999}N_{0.001} sample (VN459). The upper solid curves are taken at 34 W/cm² and the lower area corresponds to an average power density of 6 W/cm² (multiplied by 5). The dotted curves belong to the PL of undoped GaAs_{1-x}N_x with $x = 0.095\%$ (K105), which are shown for comparison with 34 W/cm². Grey vertical lines mark cluster features of VN459. Note the different scaling on the vertical axis.

Consequently, Si contributes to an apparent increase of the localization character of the LE-band. The underlying mechanism is discussed below. Furthermore, GaAs-like (e, C^0) and (D^0-A^0) transitions are not resolved in the Si-doped $\text{GaAs}_{1-x}\text{N}_x$ with $x = 0.1\%$ (VN459). Small features appear at 50 K, which might be associated with these peaks (see positions of green vertical lines at 50 K). Increasing the temperature to 50 K slightly red-shifts the peak maximum of the LE-band. Simultaneously, a high-energy shoulder evolves at 50 K and dominates the 100 K spectrum in analogy to intrinsic $\text{GaAs}_{1-x}\text{N}_x$ with $x = 0.095\%$ (K105). This transition originates from the FE or unbound ($e-h$) pairs with contributions of a dense EHP. However, the FE/EHP transition is most probably still coupled to LEs. Only a merged FE/EHP/LE-band peak is observed in the 100 K spectrum of Si-doped $\text{GaAs}_{1-x}\text{N}_x$ with $x = 0.1\%$ (see Sec. 6.1.3).

Emergence of a second LE-band on the low-energy side

Low-energy tail-LEs are less dominant in the low-temperature PL of the Si-doped sample. This behavior seems to be characteristic for LE-band formation (see Sec. 5.2.2). The PL emission from deep cluster states gains spectral weight at higher temperatures, similarly to intrinsic $\text{GaAs}_{1-x}\text{N}_x$ with $x = 0.21\%$ (K106). However, low-energy tail-LEs form two radiative bands around 1.4 eV and 1.44 eV in the Si-doped $\text{GaAs}_{1-x}\text{N}_x$ with $x = 0.1\%$ (VN459), as can best be seen in the 50 K spectrum of Fig. 5.9. The 1.44 eV band is also pronounced in the 50 K PL spectrum of intrinsic $\text{GaAs}_{1-x}\text{N}_x$ with $x = 0.095\%$ (see Fig. 5.4). LEs around 1.4 eV, on the other hand, have a much smaller contribution in K105. They merge into a second LE-band and dominate the PL at higher temperatures in VN459. The second LE-band probably appears in the PL of GaAsN:Si because more free carriers are available in the system. Consequently, more LEs are created and more deep cluster states are occupied. In order to prove the origin of the second LE-band, a sample series with the same N content but varying Si-doping should be studied. The investigation of such a series is beyond the scope of this thesis.

Comparison of LE-bands in Si-doped and intrinsic GaAsN samples

A LE-band develops in the low-temperature PL of $\text{GaAs}_{1-x}\text{N}_x\text{:Si}$ with $x = 0.1\%$ (VN459) just below the band gap. The situation is very similar in case of $\text{GaAs}_{1-x}\text{N}_x\text{:Si}$

with $x = 0.2\%$ (VN460), as shown in Fig. 5.10. Once again, solid curves and full areas represent the high- and low-power PL of VN460, respectively. The dotted lines belong

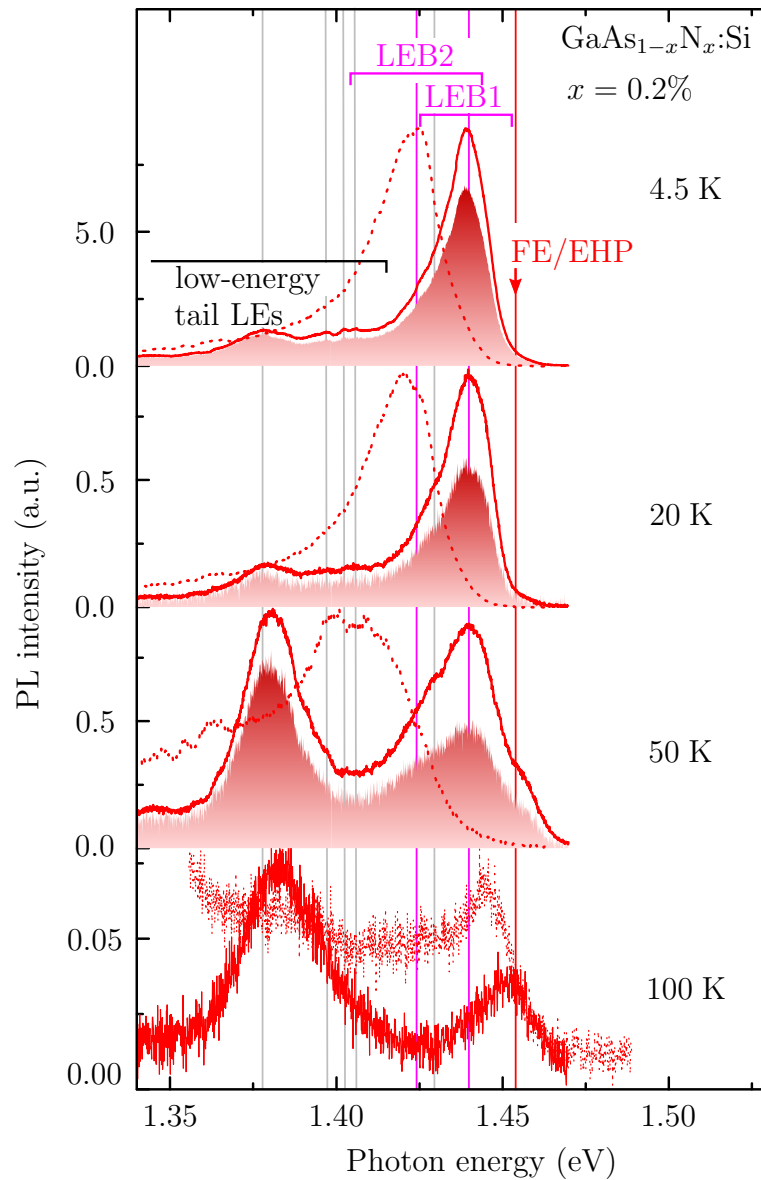


Figure 5.10.: Temperature series of the Si-doped $\text{GaAs}_{0.998}\text{N}_{0.002}$ sample (VN460). The upper solid curves are taken at 34 W/cm^2 and the lower area corresponds to an average power density of 6 W/cm^2 (multiplied by 5). The dotted curves belong to the PL of undoped $\text{GaAs}_{0.9979}\text{N}_{0.0021}$ (K106), which are shown for comparison with 34 W/cm^2 . Grey vertical lines mark cluster features of VN460. Note the different scaling on the vertical axis.

to the PL of intrinsic GaAs_{1-x}N_x with $x = 0.21\%$ (K106). The LE-band of VN460 is designated LEB1 and the one of K106 LEB2. Interestingly, LEB1 evolves at 1.44 eV and LEB2 has its maximum 20 meV below that value. Furthermore, LEB1 has the same temperature and power response as the LE-band of the Si-doped GaAs_{1-x}N_x with $x = 0.1\%$ (VN459). In particular, LEB1 appears to be more localized than LEB2. The latter significantly shifts with increasing temperature and illumination power (see also Sec. 5.2.2). The positions of the FE/EHP shoulders of K106 and VN460 are located only 8 meV apart from each other at $50 \text{ K} \leq T \leq 100 \text{ K}$. Thus, a potential band gap difference cannot be responsible for the red-shift between LEB1 and LEB2 at lower temperatures. The origin of the red-shift is in the focus of Sec. 5.3.2.

5.3.2. Discussion: LE-bands in GaAsN:Si

Several novel features are obtained in Si-doped GaAsN samples in comparison to undoped GaAsN. First, a LE-band evolves in the low-temperature PL of GaAs_{1-x}N_x:Si already in the $x = 0.1\%$ (VN459) sample. Second, this band exhibits no redistribution towards higher energies with increasing illumination power. Third, because of an enhanced coupling between the FE/EHP transition and the LE-band, only a merged FE/EHP/LE-band is obtained on the high-energy side of the 100 K PL spectrum. The same behavior is observed in GaAs_{1-x}N_x:Si with $x = 0.2\%$ (VN460). Fourth, the LE-band of the Si-doped GaAsN sample is blue-shifted with respect to the LE-band of undoped GaAsN with $x = 0.2\%$ at low temperatures. This subsection provides a possible explanation for the enhanced localization character of GaAsN:Si LE-bands and the blue-shift of LE-bands between Si-doped and undoped GaAsN.

As discussed in Sec 5.1.2, Si acts as a donor in GaAs and forms a shallow impurity level $\approx 6 \text{ meV}$ below the CB edge. This behavior is expected to be similar in GaAsN. Unlike nitrogen cluster states, the energetic position of silicon impurities remains fixed with respect to the CB edge when the N content increases. Thus, shallow cluster states can be partially occupied by carriers from the Si-level. Consequently, more cluster states are occupied simultaneously below the CB minimum, similarly to the behavior at elevated excitation power. The formerly efficient interexcitonic population transfer towards lower lying cluster states (overlap of cluster-exciton wave functions) is partially suppressed by silicon. Thus, less non-radiative recombination processes occur in the PL before a radiant event takes place at low temperatures. Mostly

higher lying cluster states contribute to the low-temperature PL in VN samples and a red-shift occurs between low-temperature PL spectra of Si-doped and undoped samples (see Figs. 5.3, 5.9 and 5.10). Since LE-bands of GaAsN:Si are located just below the CB edge, a blue-shift cannot be achieved as easily as in intrinsic GaAsN. Only in case of strong pulsed excitation, a shift is observed (not shown here). Thus, LE-bands appear to be more localized in Si-doped samples. The actual localization character is investigated in Chap. 6.

5.4. Recombination dynamics in GaAsN:Si

Nitrogen incorporation significantly changes typical properties of GaAs, as shown in Chap. 4 and 5. Continuous-wave luminescence spectra have different appearances, depending on the N content, sample quality and resolution and are discussed in Secs. 5.2 - 5.3. Nevertheless, the underlying recombination dynamics is similar in all (In)GaAsN epilayers [98, 27, 10, 49]. We saw in the previous section that GaAsN:Si has

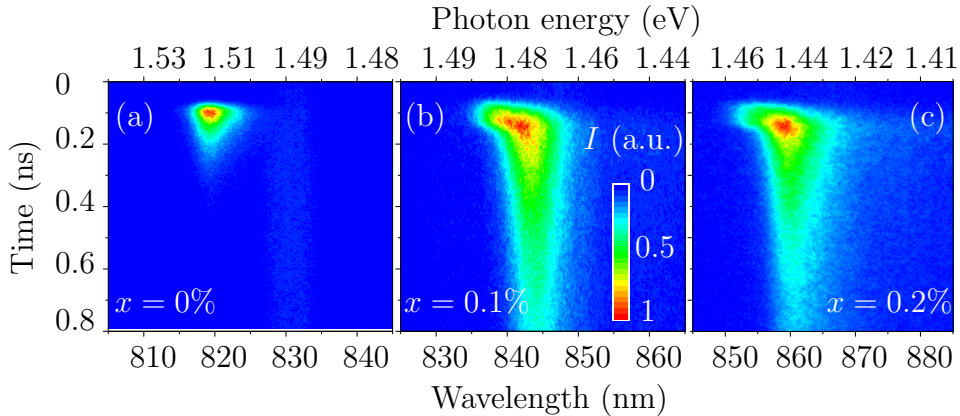


Figure 5.11.: Streak camera images of the PL decay from GaAs_{1-x}N_x:Si with (a) $x = 0\%$, (b) $x = 0.1\%$ and (c) $x = 0.2\%$ and an average power density of 9.5 W/cm^2 at 10 K. The intensities are normalized for better comparison between samples.

some additional PL-features in comparison to intrinsic GaAsN samples. Considering possible applications, it is essential to know if the underlying recombination dynamics also differs in Si-doped samples. We apply a systematic time-resolved PL study on Si-doped GaAs_{1-x}N_x with $x = 0\% - 0.2\%$ for the first time. Parts of this section are currently under review for publication in Applied Physics Letters. The experimental

setup is introduced in Sec. 3.2 and an overview of the samples can be found in A.1. Fig. 5.11 shows low-temperature streak camera images of the time-resolved PL. Several characteristic features of the N-containing samples in 5.11 (b) - 5.11 (c) are conspicuous. In particular, the PL decay of GaAsN exhibits a strong energy dispersion in comparison to the reference sample in 5.11 (a). Similar observations were made in undoped InGaAsN [98, 10] and GaAsN quantum-wells and epilayers [29, 27]. The decay times of GaAsN are obviously shorter on the high-energy side than in the reference and much longer on the low-energy side of the LE-band luminescence.

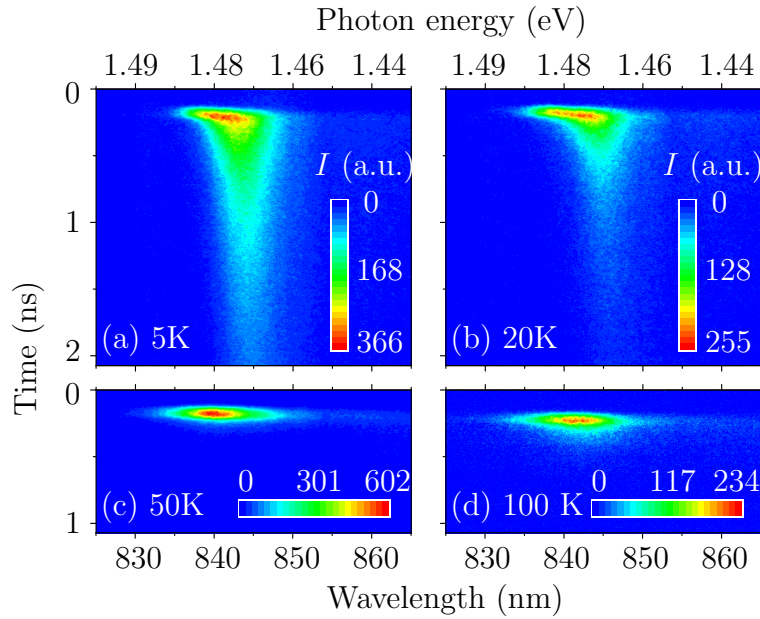


Figure 5.12.: Streak camera images of the PL decay from $\text{GaAs}_{1-x}\text{N}_x:\text{Si}$ with $x = 0.1\%$ at (a) 5 K, (b) 20 K, (c) 50 K and (d) 100 K taken at different power densities.

Furthermore, the line width significantly broadens and smears out with increasing N content, as already observed in cw PL in Sec. 5.2. Fig. 5.12 shows streak camera images of $\text{GaAs}_{1-x}\text{N}_x:\text{Si}$ with $x = 0.1\%$ at four different temperatures. The PL decay considerably shortens with increasing temperature and decreases the energy dispersion of the decay. A similar temperature behavior was found in undoped (In)GaAsN [98, 10, 70].

The energy dispersion of the decay times is studied in the first part of this section. The temperature dependence of the decay times is discussed. The second part is dedicated to the impact of the N content on the decay times.

5.4.1. Dispersion of PL decay times

The asymmetric streak camera images of GaAsN:Si in Fig. 5.11 and Fig. 5.12 illustrate qualitatively the energy dispersion of the PL decay times. A quantitative analysis is performed in this subsection. Three neighboring low-temperature decay line profiles are shown in Fig. 5.13 (a) - (c). The underlying time-resolved PL measurement is taken at 5 K and 9.5 W/cm^2 and corresponds to the streak camera image in Fig. 5.12 (a). The decay dynamics is characterized by a monoexponential function with an offset,

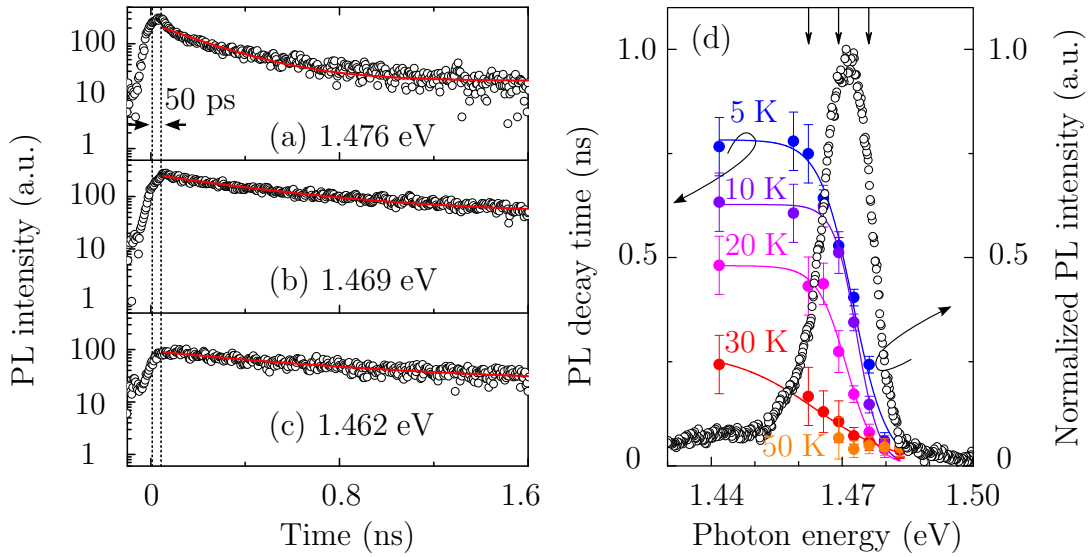


Figure 5.13.: (a) - (c) PL decay line profiles of different energy positions of time-resolved PL in GaAs_{1-x}N_x:Si with $x = 0.1\%$ (VN459) at 5 K and 9.5 W/cm^2 . Circles represent experimental data points and red lines illustrate monoexponential fit functions. (d) Temperature dependence of the decay time dispersion is shown with full circles. Solid lines correspond to a fit from Eq. (5.2). The normalized PL intensity of the 5 K spectra is shown for comparison (empty circles). The energy positions of the shown PL line profiles in (a) - (c) are indicated with vertical arrows in (d).

as shown with red curves. The offset accounts for recombination processes with ultra-long decay times, which originate from efficiently trapped carriers, as observed e.g. in n-type InGaAs/GaAs quantum dots [17]. The monoexponential function mainly describes the decay of localized excitons. Another decay feature appears in the first 100 ps in Fig. 5.13 (a) - (c) shortly after laser excitation. This ultra-short PL decay is mostly pronounced on the high-energy side of the spectrum, as shown in

Fig. 5.13 (a). While this fast decay is related to carrier cooling, we now focus on the PL decay after this thermalization. We use the monoexponential decay function after a certain thermalization time of 50 ps for our data analysis. The PL decay time of localized excitons decreases by a factor of 3.1 in a small energy interval of 14 meV.

The resulting PL decay times are summarized in Fig. 5.13 (d). They correspond to different PL energies in a temperature range of 5 K - 50 K. For a better overview, the time-integrated low-temperature PL spectrum of GaAs_{1-x}N_x:Si with $x = 0.1\%$ is also displayed. At low temperatures, the mentioned energy dispersion of the PL decay times $\tau(E)$ is very pronounced in this representation. It can only be explained by the existence of an additional non-radiative energy transfer channel. The energy dependent PL decay of localized excitons can be fitted by [117, 98]

$$\tau(E) = \frac{\tau_R}{1 + \exp(\alpha(E - E_m))}, \quad (5.2)$$

with a maximum decay time τ_R , an energy E_m corresponding to the mobility edge (see also Fig. 5.6) and an energy scaling factor α with $1/\alpha$ in the order of 2.59 meV – 9.55 meV. According to Eq. (5.2), excitons with an energy E can recombine radiatively or be transferred non-radiatively towards deeper lying cluster states. The non-radiative transfer can be regarded as an exciton hopping process and was introduced in Sec. 5.2.1 (see Fig. 5.6). After optical excitation, excitons preferentially hop several times to lower energies before they recombine radiatively [11]. Consequently, the non-radiative transfer dominates on the high-energy side of the PL spectrum, which corresponds to all energies $E > E_m$. The observed radiative transitions are either delocalized or slightly localized excitons, which can be easily transferred out or their sites [98]. Thus, they have extremely short decay times: e.g. $\tau(1.476 \text{ eV}) = 0.24 \text{ ns}$ for 5 K. On the other hand, most transitions are radiative below E_m and correspond to strongly localized excitons with longer decay times. In case of GaAs_{0.999}N_{0.001}:Si, slow recombination processes dominate for $E < 1.47 \text{ eV}$. Thus, the so-called mobility edge [117] E_m corresponds to an energy with equal recombination and transfer rates [98]. Furthermore, the non-radiative transfer rate scales exponentially with the energy difference. An overview of the fitting results is provided in Tab. 5.1.

We now turn to the temperature dependence of the PL decay times. It is evident that the energy dispersion of the PL decay rapidly decreases in the investigated temperature range, as shown in Fig. 5.13 (d). A similar behavior was observed in

undoped (In)GaAsN [98, 70, 10]. Increasing the temperature enhances the diffusion of excitons towards lower lying cluster states. Furthermore, some LEs are ionized into delocalized states. Both reduces the PL decay time τ_R of LEs. A strong reduction of the PL decay time by more than one order of magnitude occurs in GaAs_{1-x}N_x:Si with $x = 0.1\%$ in the range of 5 K - 50 K. This observation matches cw PL results in Fig. 5.9, where the FE/EHP transition is recognized as a high-energy shoulder of the 50 K PL. On the other hand, α and E_m show no significant temperature dependence in the investigated range (see Tab. 5.1).

	VN459				VN460	
Temperature	5 K	10 K	15 K	20 K	30 K	10 K
E_m (eV)	1.472	1.473	1.472	1.471	1.464	1.445
τ_R (ns)	0.78	0.63	0.63	0.48	0.27	0.44
$1/\alpha$ (meV)	3.8	2.6	2.8	3.3	9.5	3.6

Table 5.1.: Fit results for the decay time dispersion with Eq. (5.2) for VN459 with $x = 0.1\%$ and VN460 with $x = 0.2\%$.

5.4.2. Impact of nitrogen on the PL decay times of GaAsN:Si

Localized excitons of GaAs_{1-x}N_x:Si with $x = 0.2\%$ can be similarly described by Eq. (5.2), as shown in Fig. 5.14. In analogy to Fig. 5.13 (d), energy dependent decay times and fits are presented with time-integrated PL curves. The reference sample (VN463) has a negligible dispersion in the investigated range, as shown in Fig. 5.14 (a). The decay times are almost constant with $73.9 \text{ ns} \leq \tau \leq 75.4 \text{ ps}$, as shown in the inset of Fig. 5.14 (a). The reference sample has a better lattice quality in comparison to nitrogen containing samples. Thus, exciton hopping is insignificant and the PL decay exhibits practically no energy dispersion. The apparent low decay time values are caused by a reduced growth temperature of the samples under study. Low-temperature growth is known to strongly reduce the PL decay time [54] by a higher amount of non-radiative recombination processes.

As mentioned before, the decay time dispersion is very pronounced in both N containing samples in Fig. 5.14 (b) - (c). Furthermore, the maximum decay time τ_R is reduced in the $x = 0.2\%$ sample in comparison to $x = 0.1\%$, as shown in Tab. 5.1.

This observation is attributed to a more efficient exciton transfer (hopping) because of an enhanced defect density in the $x = 0.2\%$ sample in comparison to the $x = 0.1\%$ sample. The mobility edge energy E_m continuously decreases with the N content and α only varies within the margin of error (see Tab. 5.1).

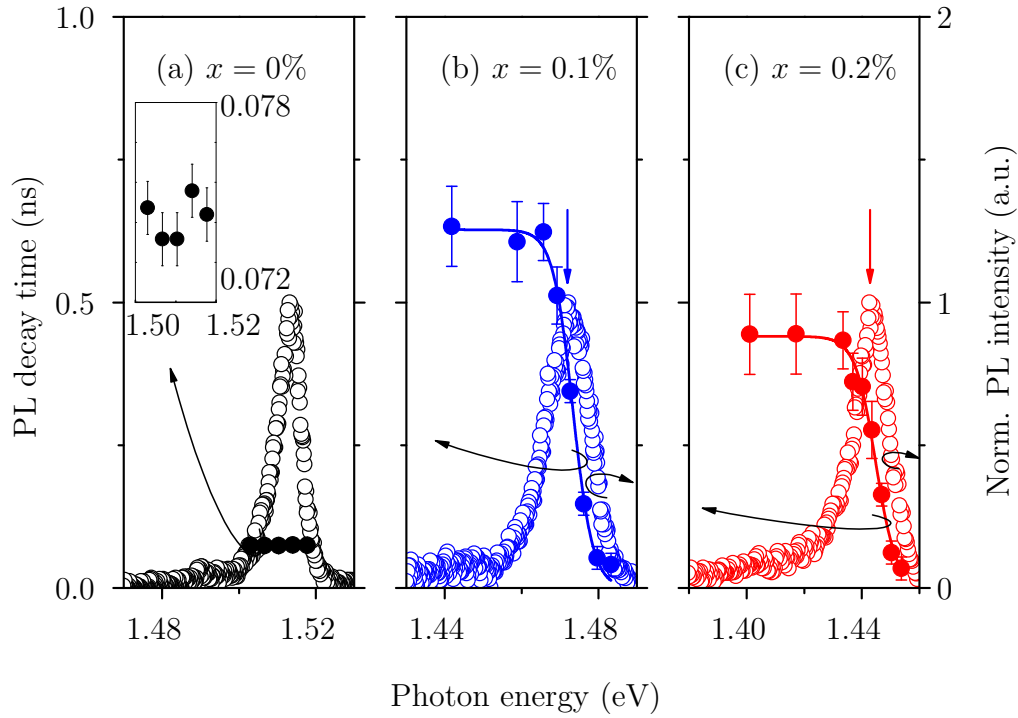


Figure 5.14.: Energy dispersion of the decay time (full circles) in GaAs_{1-x}N_x:Si with (a) $x = 0\%$, (b) $x = 0.1\%$ and (c) 0.2% at 10 K. Solid lines correspond to a fit from Eq. (5.2). The normalized PL spectra are shown for comparison (empty circles). The time-resolved PL is performed at 10 K with 9.5 W/cm^2 . The inset zooms in on the smaller energy dispersion of the reference in (a).

A similar decay time asymmetry was observed in intrinsic GaAsN epilayers before [29, 27]. However, our determined maximum decay time values are significantly shorter than the reported values of $\tau_R \approx 5 - 8 \text{ ns}$ [27] in the intrinsic material. This can be explained by a higher contribution of non-radiative Auger and Shockley-Read-Hall recombinations, as was observed in n-type GaAs [97]. The emitted energy of an electron-hole pair is directly absorbed by a third particle in case of Auger recombination. This particle relaxes by phonon-emission or diffusion on its part. The excited electron is transferred non-radiatively to an impurity level and subsequently relaxes

radiatively in case of Shockley-Read-Hall recombination. It resembles the interexcitonic transfer via exciton hopping [11], which is discussed in Sec. 5.2.1. However, the Shockley-Read-Hall recombination describes single electrons and holes in contrast to the exciton hopping, which applies to excitons. Nevertheless, in case of n-doped GaAs [62, 30] the impact of the doping is insignificant below 10^{18} cm^{-3} . We conclude that the contribution of Shockley-Read-Hall and possibly Auger recombinations is higher in n-type GaAsN in comparison to n-type GaAs and intrinsic GaAsN. Especially Shockley-Read-Hall recombinations significantly increase with the defect density. This behavior has a substantial impact on possible applications.

5.5. Summary and outlook

We performed continuous-wave photoluminescence (PL) in GaAsN and GaAsN:Si. Furthermore, we studied the PL dynamics of GaAsN:Si. The PL of the intrinsic $\text{GaAs}_{1-x}\text{N}_x$ with $x = 0.095\%$ has GaAs-related transitions and typical N-induced cluster features. In particular, the low-temperature PL is dominated by localized excitons (LEs) and GaAs related transitions (e, C^0) and (D^0-A^0). High-energy LEs emerge in a LE-band at low temperatures and tail-LEs only gain spectral weight for $T > 50 \text{ K}$ because of a lower interexcitonic population transfer. The latter ones can be attributed to deeper lying cluster states. The free exciton/electron-hole plasma (FE/EHP) transition emerges from the high-energy shoulder of the LE-band and dominates the PL for $T \geq 100 \text{ K}$. By increasing the N content of undoped GaAsN, distinct PL features merge into a broad and asymmetric spectral band. This band consists of sharp LEs with adjacent energetic positions, which cannot be resolved in our PL study. Despite the localized character of individual LEs inside the LE-band, it exhibits a partially delocalized character. This is achieved by an efficient interexcitonic transfer mechanism of high-energy LEs and the underlying overlap of exciton wave functions. Tail-LEs dominate the PL spectrum at $T \geq 50 \text{ K}$ and the FE/EHP transition emerges at $T = 100 \text{ K}$. Furthermore, non-radiative relaxation processes considerably decrease the radiation yield in comparison to the $x = 0.095\%$ sample.

Si-doped $\text{GaAs}_{1-x}\text{N}_x$ samples show novel properties in comparison to undoped GaAsN. In particular, merged spectral bands dominate the PL spectra for $x \geq 0.1\%$. These bands exhibit a diminished shift with excitation power or temperature increase.

Consequently, they have an apparent higher localization character in comparison to intrinsic GaAsN LE-bands. The actual localization character is analyzed in Chap. 6. Furthermore, the LE-band of the Si-doped GaAs_{1-x}N_x sample is blue-shifted with respect to the LE-band of intrinsic GaAs_{1-x}N_x with $x = 0.2\%$ at low temperatures. This can be explained with a partially suppressed interexcitonic transfer towards lower lying LEs in GaAsN:Si. The incorporation of shallow dopants has a similar effect on the PL as the increase of the illumination power. In both cases, more cluster states are occupied simultaneously and the interexcitonic population transfer is partially suppressed.

A temperature-dependent time-resolved PL investigation was performed on Si-doped GaAsN for the first time. The PL decay is predominantly monoexponential and exhibits a strong energy dispersion with ultra-short decay times on the high-energy side and long decay times on the low-energy side. This asymmetry can be explained by the existence of an additional non-radiative energy transfer channel. The recombination is predominantly non-radiative on the high-energy side of the spectral band and LEs are mainly transferred towards lower lying cluster states. The radiative transitions mainly correspond to FE/EHP transitions with extremely short decay times. Transitions are predominantly radiative on the low-energy part of the PL and have longer decay times. An increase of the thermal energy transfers excitons towards lower lying cluster states and consequently reduces the PL decay time of LEs. Even though a similar decay time asymmetry and temperature dependence was observed in GaAsN epilayers before [27, 29], the determined maximum decay times of GaAsN:Si are significantly reduced in comparison to undoped GaAsN. This can be explained by a higher contribution of Shockley-Read-Hall and possibly Auger recombinations in GaAsN:Si in comparison to undoped GaAsN. In order to find a quantitative relationship between the decay time reduction of GaAsN:Si and the Si-doping, a GaAsN:Si sample series with a constant N content and varying Si-doping should be investigated. Such a study could be part of a follow-up project.

6. Photoluminescence study of GaAsN and GaAsN:Si in high magnetic fields

In this chapter, photoluminescence properties of GaAsN are investigated in high magnetic fields up to 62 T. We study both intrinsic as well as Si-doped GaAsN epilayers. While the former type of samples has previously been investigated by Alberi et al. [2], the latter system has not been studied with magneto-PL. The analysis of the interexcitonic transfer of GaAsN in high magnetic fields and its temperature dependence is another new contribution. A new magneto-PL setup is built for this task, which works in pulsed magnetic fields of the HLD. The experimental details are shown in Sec. 3.3.1 and App. A.3. In the first section, the PL characteristics of LE-bands is studied in high magnetic fields. Section two is dedicated to a magneto-PL study for electron effective mass determination. All results are summarized in section three.

6.1. LE-bands in high magnetic fields

Incorporating nitrogen into GaAs reduces the band gap of the system. In addition, nitrogen forms clusters of different sizes. The empirical pseudopotential method [74, 75] and the LCINS model [94, 114] describe the formation and its consequences on the band structure from a theoretical perspective, as shown in Chap. 2. Clusters have a strong impact on the PL characteristics, as shown in Chap. 5. However, only assumptions are made concerning the actual localization character of LE-bands. Only delocalized or partially delocalized transitions exhibit a field-induced blue-shift in a magnetic field. Consequently, high magnetic fields grant access to the localization

character. Furthermore, the formation and evolution of LE-bands can be studied in high magnetic fields. Increasing the N content pushes the CB edge to lower energies [136] but the energy levels of highly localized clusters remain fixed. Consequently, the CB hybridizes with cluster states. The magnetic field reverses this trend, lifts the CB edge and reveals formerly hybridized cluster states [2].

It is instructive to start the PL investigation with intrinsic GaAsN samples. They exhibit a more obvious separation between the FE transition, the LE-band and LEs of the low-energy tail, as shown in Secs. 5.2.1 - 5.2.2. Consequently, this chapter is structured in the same manner. Undoped samples are presented in the first section and Si-doped ones in the third section. The second section is dedicated to the population transfer of LEs in intrinsic GaAsN. The influence of a higher thermal energy is studied. The interexcitonic transfer is discussed in GaAsN and GaAsN:Si in section four.

6.1.1. Magneto-photoluminescence of intrinsic GaAsN

Fig. 6.1 shows magneto-PL results of undoped GaAs_{1-x}N_x samples with (b) $x = 0.095\%$ (K105) and (c) $x = 0.21\%$ (K106). Common cluster features are highlighted with vertical lines A - J. The reference sample is shown in (a) for comparison. We perform the experiments in the HLD at 20 – 30 K, using the setup that is introduced in Sec. 3.3.1. The origin of the individual transitions is discussed in Sec. 5.2. However, the spectral weight slightly differs from Fig. 5.4 and Fig. 5.8 at 0 T. A higher illumination power might be responsible for this observation.

The FE/EHP transition is the most dominant contribution of the reference sample in (a) and continuously blue-shifts with increasing magnetic field. This is because of a field-induced shift of the CB and VB edges to higher and lower energies, respectively. Consequently, the band gap increases proportionally to the applied magnetic field, which leads to the continuous blue-shift of the FE/EHP in the high-field limit (see also Fig. 6.5). The same transition can be found in (b) - (c) on the high-energy side. However, it exhibits a diminished blue-shift and vanishes at around 30 T in case of N containing samples. This observation is discussed in Sec. 6.1.4. The high magnetic field behavior of LEs and LE-bands of intrinsic GaAsN is in the focus of this subsection. Both the LE-band of K106 with $x = 0.21\%$ (area B at 0 T) and the envelope of high-energy LEs of K105 with

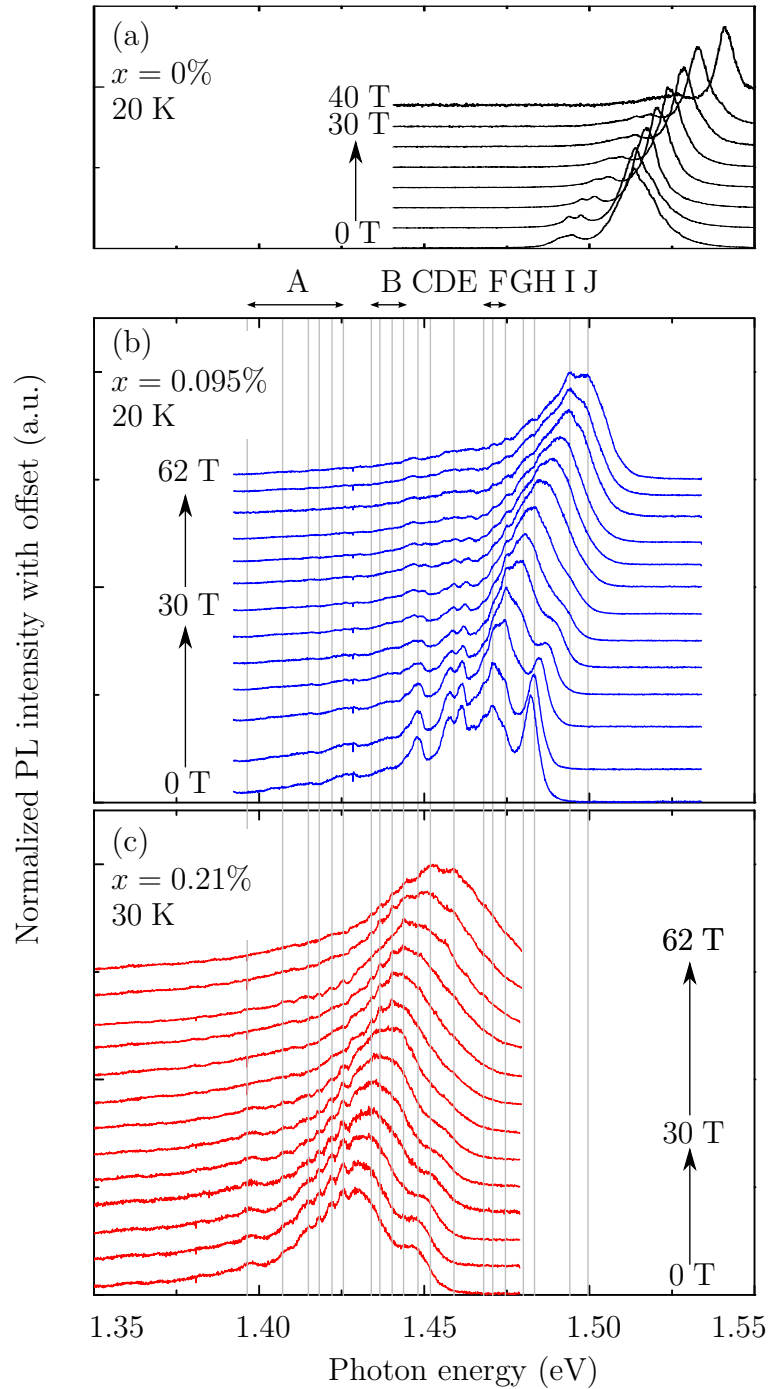


Figure 6.1.: Magneto-PL study of $\text{GaAs}_{1-x}\text{N}_x$ with (a) Si-doped reference, (b) $x = 0.095\%$ (K105) and (c) $x = 0.21\%$ (K106) at 20 – 30 K. The magnetic field increases from bottom to top in increments of 5 T. Common cluster features are highlighted with vertical lines in areas A - J.

$x = 0.095\%$ (area F at 0 T) clearly blue-shift with increasing magnetic field. This points to a partially delocalized character of these transitions. Our power-dependent PL investigation led to the same conclusion for LE-bands of intrinsic GaAsN in Sec. 5.2.2. The magneto-PL study supports this interpretation and shows that the envelope of distinct LEs of intrinsic GaAs_{1-x}N_x with $x = 0.095\%$ (K105) has a similar degree of delocalization as the LE-band of intrinsic GaAs_{1-x}N_x with $x = 0.21\%$ (K106). We noticed already in Sec. 5.2.1 that the population of high-energy side LEs of K105 is affected by the illumination power and proposed a possible model for interexcitonic population transfer in Sec. 5.2.1. As pointed out in Sec. 5.2.2, the efficiency of the population transfer gradually decreases with cluster state depth. This conclusion is supported by the behavior of LEs from area A in (b) - (c). They exhibit no measurable shift in the magnetic field in both N containing samples and can be classified as localized transitions. The magnetic field behavior of N containing samples can thus be explained in terms of the population transfer of LEs: The magnetic field reduces the Bohr radius of excitons. Consequently, LEs with the smallest wave function overlap decouple from the LE-band first. This applies to the low-energy tail and LEs from the low-energy side of the LE-band. Already a weak magnetic field and thus small decrease of the Bohr radius is sufficient to break up the interexcitonic transfer. When the magnetic field is elevated, more and more LEs decouple from the LE-band. This corresponds to LEs of the region B in Fig. 6.1 (b). Simultaneously, more and more of formerly hybridized cluster states are exposed just below the CB minimum when the CB blue-shifts. Excitons are trapped by these states and interact with LEs of the LE-band. Consequently, a blue-shift of the LE-band can be obtained in magnetic fields.

6.1.2. Interexcitonic population transfer and the impact of a higher thermal energy

The partially delocalized character of LE-bands is discussed in terms of an efficient interexcitonic transfer mechanism in Sec. 6.1.1. But how does a temperature increase influence this delocalized character? Magneto-PL investigations at higher temperatures can help us better understand the population transfer of LEs. The only

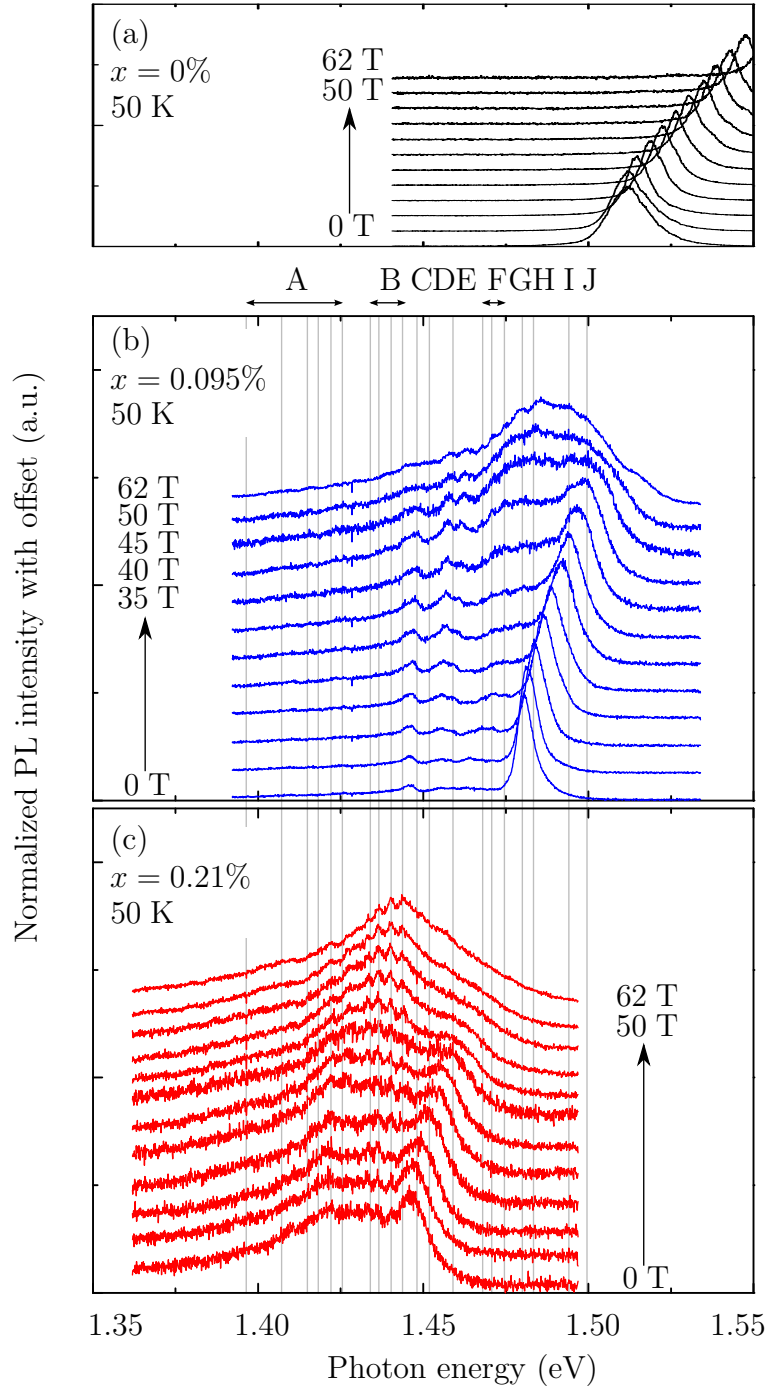


Figure 6.2.: Magneto-PL study of $\text{GaAs}_{1-x}\text{N}_x$ with (a) Si-doped reference, (b) $x = 0.095\%$ (K105) and (c) $x = 0.21\%$ (K106) at 50 K. The magnetic field increases from bottom to top in increments of 5 T. Common cluster features are highlighted with vertical lines in areas A - J.

comparable study on low-temperature PL in fields up to 57 T was done by Alberi et al. [2]. Fig. 6.2 shows magneto-PL of intrinsic GaAs_{1-x}N_x samples with (b) $x = 0.095\%$ (K105) and (c) $x = 0.21\%$ (K106) at 50 K. The reference sample GaAs:Si (VN463) is presented in (a) for comparison. In analogy to Fig. 6.1, the spectral weight of the PL slightly differs from the 50 K spectra, which are shown in Sec. 5.2.1. This is probably caused by higher illumination powers.

The FE/EHP transition of the reference sample exhibits the expected blue-shift in (a). Deeper lying peaks are less occupied in comparison to Fig. 6.1. Intrinsic GaAs_{1-x}N_x with $x = 0.095\%$ has a similar behavior in (b). As observed in Fig. 5.4, the intensity of the FE/EHP transition increases with temperature. Thus, FE/EHP is the most dominant peak and it blue-shifts continuously up to 45 T. At low magnetic fields, LEs below FE/EHP are diminished (region D - F) in Fig. 6.2 (b). They gain spectral weight with increasing magnetic field and appear as a broad LE-band for $B \geq 35$ T. In case of intrinsic GaAs_{1-x}N_x with $x = 0.21\%$ (K106), the FE/EHP transition is also pronounced in Fig. 6.2 (c) and it blue-shifts. Simultaneously, LEs contribute to the PL in regions A and B already at 0 T within a plateau.

In order to study the impact of a higher thermal energy on the population transfer of LEs, which affects both the occupation of LE states and the scattering via optical phonons, the field-induced blue-shift of the LE-band is also investigated at 50 K. In case of undoped GaAs_{1-x}N_x with $x = 0.21\%$ (K106), the blue-shift of the LE-band is very weak in Fig. 6.2 (c). Only a slight redistribution towards higher cluster states can be observed. The LE-band of intrinsic GaAs_{1-x}N_x with $x = 0.095\%$ (K105) can only be analyzed for $B > 35$ T in Fig. 6.2 (b). However, its blue-shift is similarly diminished in this field range. In particular, the maximum of the LE-band lies between I and J at 62 T in Fig. 6.1 (b) and at H in Fig. 6.2 (b). Consequently, the population transfer of LEs is significantly quenched at 50 K and thus the partially delocalized character of the LE-band. Our magneto-PL study illustrates that a higher thermal energy efficiently interferes with the population transfer of LEs. Consequently, the interexcitonic transfer mechanism only works below a critical temperature $20 \text{ K} < T < 50 \text{ K}$.

6.1.3. Magneto-PL of GaAsN:Si

While Si-doping has only a weak influence on the PL of GaAs, it strongly influences the PL spectra from GaAsN. All investigated GaAsN:Si samples have characteristic

spectral bands with an apparent higher localization character, as shown in Sec. 5.3. The actual localization character of the LE-band can be investigated with magneto-PL. It is shown exemplarily for $\text{GaAs}_{1-x}\text{N}_x:\text{Si}$ with $x = 0.2\%$ (VN460) at two different

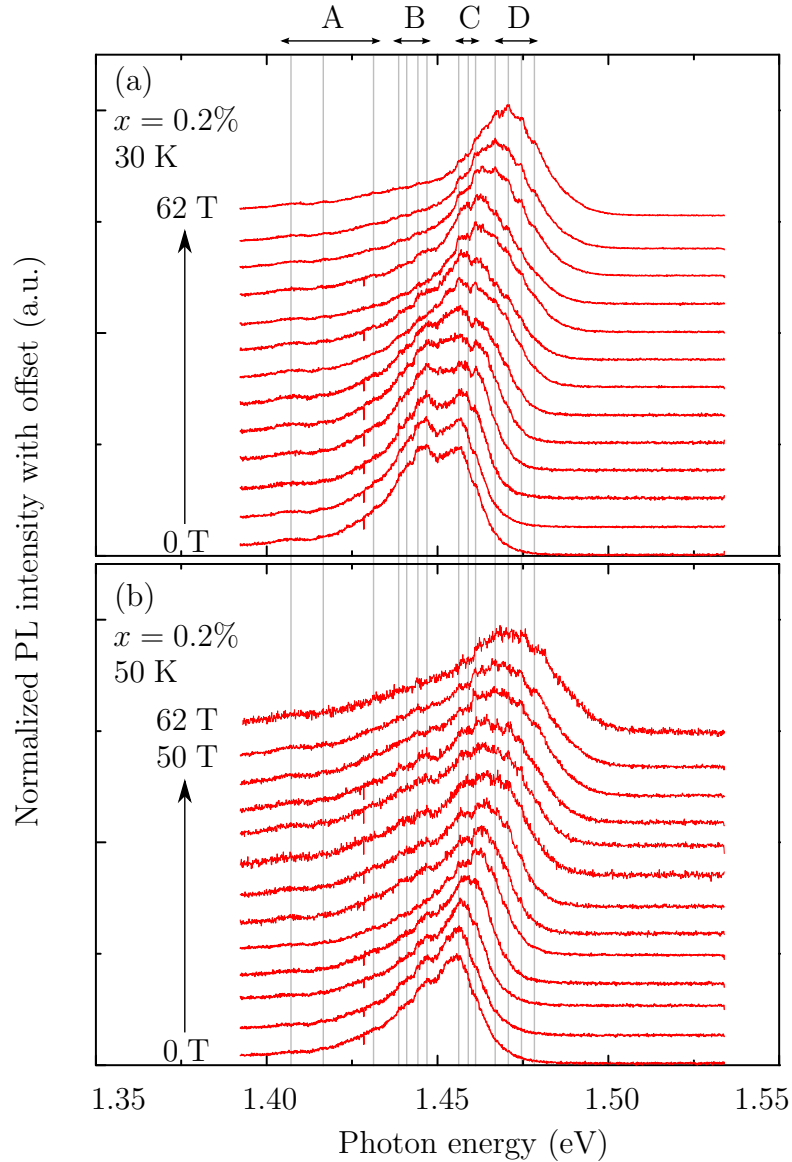


Figure 6.3.: Magneto-PL in $\text{GaAs}_{1-x}\text{N}_x:\text{Si}$ with $x = 0.2\%$ at (a) 30 K and (b) 50 K. The magnetic field increases from bottom to top in increments of 5 T. Common cluster features are highlighted with vertical lines A - D.

temperatures in Fig. 6.3. In comparison to Fig. 5.10, the spectral weight is shifted towards higher energies. Higher illumination powers are most probably responsible.

The broad spectral band is divided into two equal contributions at 0 T, as can be seen in Fig. 6.3 (a). The FE/EHP transition cannot be identified with sufficient certainty. It could be part of the high-energy shoulder of the LE-band in region C. Several subfeatures also appear in the spectrum (region B - C). They correspond to LEs and exhibit no blue-shift in the magnetic field on their own. However, the envelope of different LEs indeed blue-shifts. A similar behavior is visible in Fig. 6.3 (b) at 50 K. Even though the spectral distributions are slightly different in Fig. 6.3 (a) and Fig. 6.3 (b), the magnetic-field behavior is equivalent. In particular, the maxima of the LE-bands lie in the same region at 62 T. In contrast, the blue-shift of the LE-band is substantially quenched in intrinsic GaAsN at 50 K (see Fig. 6.2 (c)) in comparison to 30 K (see Fig. 6.1 (c)). Consequently, an increase of the thermal energy does not significantly influence the interexcitonic transfer and thus the partially delocalized character of the LE-band in GaAs_{1-x}N_x:Si with $x = 0.2\%$.

Fig. 6.4 illustrates magneto-PL spectra of all GaAsN:Si samples at 50 K. The FE/EHP transition of the reference sample exhibits the expected blue-shift in (a). In case of GaAs_{1-x}N_x:Si with $x = 0.1\%$ (VN459), only one broad PL peak appears in the spectrum of Fig. 6.4 (b). This peak represents merged FE/EHP and LE-band transitions (see also Fig. 5.10). The merged peak continuously blue-shifts up to 35 T. The corresponding PL profile is marked with an arrow. At higher fields, the spectral band broadens and only shows a small redistribution towards higher energies. Taking a closer look at the magnetic field response of GaAs_{1-x}N_x:Si with $x = 0.2\%$ (VN460) in Fig. 6.4 (c), a similar behavior can be found. The two magnetic field ranges of the magneto-PL in Fig. 6.4 (b) - (c) most probably originate from saturating FE/EHP transitions at $B > 35$ T. Since FE/EHP transitions are not observed in undoped GaAsN samples between 30 T and 45 T (see Figs. 6.1 - 6.2), the same saturation can be expected in GaAsN:Si. Consequently, the FE/EHP transition contributes to an enhanced blue-shift of the merged FE/EHP/LE-band PL below 35 T. The partially delocalized character is diminished for higher fields, where it most probably only corresponds to the LE-band (saturated FE/EHP transition).

6.1.4. Discussion on the interexcitonic transfer mechanism

The PL characteristics of intrinsic GaAsN and GaAsN:Si is affected by the N content,

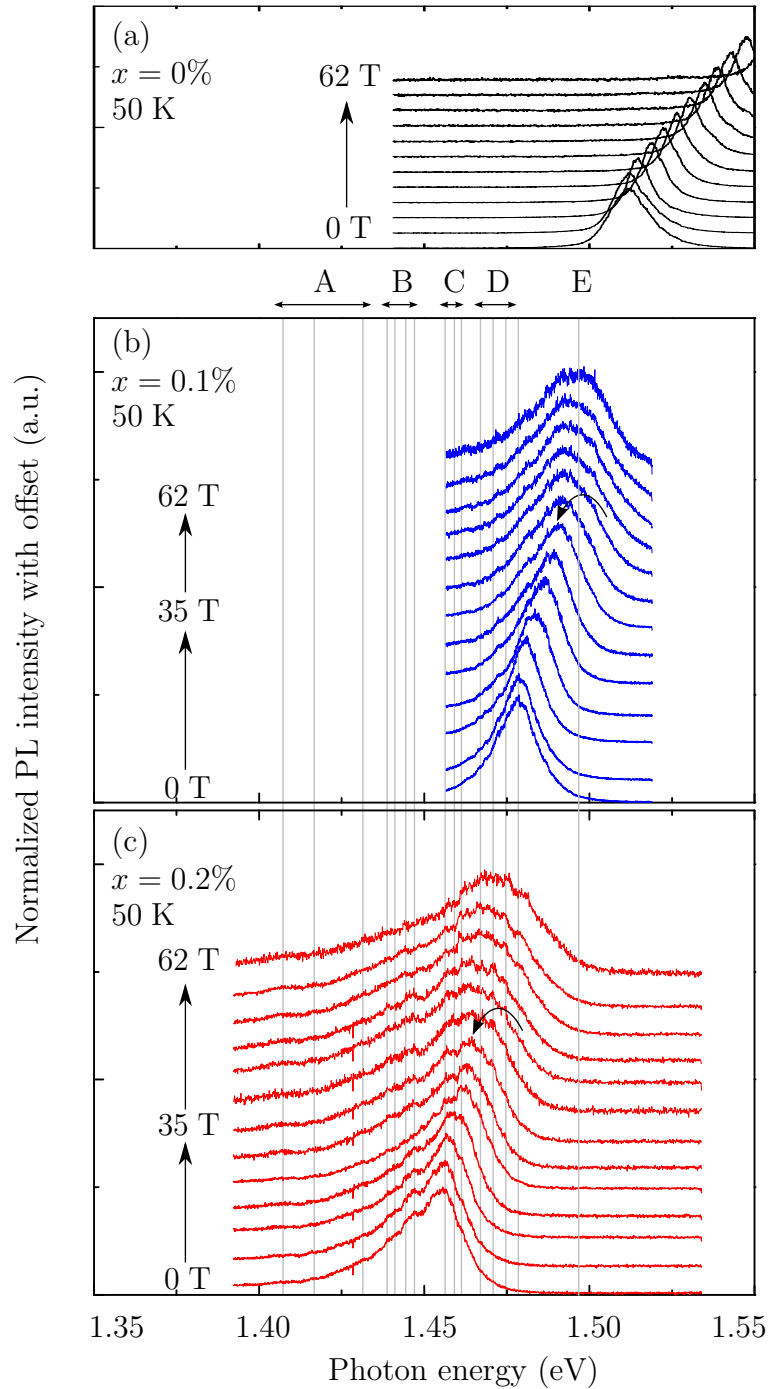


Figure 6.4.: Magneto-PL study of $\text{GaAs}_{1-x}\text{N}_x:\text{Si}$ with (a) $x = 0\%$ (VN463), (b) $x = 0.1\%$ (VN459) and (c) $x = 0.2\%$ (VN460) at 50 K. The magnetic field increases from bottom to top in increments of 5 T. Common cluster features are highlighted with vertical lines in areas A - E.

temperature, illumination power, resolution and incorporation of shallow dopants. Secs. 5.2 - 5.4 give a detailed overview of the most important PL properties of GaAsN and GaAsN:Si. Besides experimental conditions, like resolution, other aspects directly modify the interexcitonic population transfer of LEs. As discussed in Sec. 5.2.1, the interexcitonic transfer originates from overlapping cluster-exciton wave functions and can be explained e.g. within the model of hopping excitons [11]. According to this model, a trapped exciton can recombine radiatively, hop to the mobility edge E_m or hop to another localization center. At low temperatures, excitons preferentially hop several times to lower energies before they recombine. This interexcitonic transfer (e.g. via hopping) is responsible for the partially delocalized character of LEs envelopes and LE-bands in intrinsic GaAs_{1-x}N_x with $x = 0.095\%$ (K105) and $x = 0.21\%$ (K106), respectively.

As mentioned above, the population transfer can easily be affected. Increasing the temperature, for instance, diminishes the transfer in intrinsic GaAsN, as shown in Sec. 6.1.2. The incorporation of shallow dopants has a similar effect on the PL as the increase of the illumination power. In both cases, more cluster states are occupied simultaneously and the efficient interexcitonic population transfer is suppressed at lower energies. Thus, the FE/EHP transition and LEs with highest energies merge and dominate the PL in GaAsN:Si. Consequently, a blue-shift of GaAsN:Si LE-bands and shorter maximum decay times are observed in comparison to undoped samples (see Secs. 5.3 and 5.4) at low temperatures. Furthermore, a divided magnetic field response of the GaAsN:Si PL is obtained in Sec. 6.1.3. In particular, an enhanced blue-shift and thus delocalized character of the merged band is observed below 35 T in Fig. 6.4 in comparison to LE-bands of intrinsic GaAsN in Fig. 6.2. However, the blue-shift is reduced above this critical magnetic field. Furthermore, an increased thermal energy has a diminished impact on the interexcitonic transfer of GaAs_{1-x}N_x:Si, as shown in Fig. 6.3. In case of intrinsic GaAs_{1-x}N_x with $x = 0.095\%$ (K105) and $x = 0.21\%$ (K106), the partially delocalized character is strongly affected at 50 K (see Fig. 6.1 and Fig. 6.2). This indicates that the interexcitonic population transfer of Si-doped GaAsN is more complex than in undoped samples. Interactions with negative trions may be responsible.

The variety of shallow cluster states and the efficient interexcitonic population transfer is also responsible for the saturation of the FE/EHP peak intensity in high magnetic fields, as depicted in Fig. 6.1 - 6.4. The Coulomb interaction of Wannier

excitons can be neglected in the high-field limit. However, excitonic transitions are favored in comparison to (e–h) transitions. Thus, LEs predominantly appear on the high-energy side at $B \geq 45$ T in N containing samples. Because of a much smaller amount of localization centers in the reference, FE/EHP/(e–h) also dominates the high-field spectrum. FE/EHP already saturates for $B \geq 30$ T at 30 K. This behavior is promoted by a more efficient population transfer of LEs on the high-energy side at lower temperatures, as can be seen in Fig. 6.1.

6.2. Determination of the reduced effective mass of GaAsN via magneto-PL

Magneto-PL has been numerously applied in the past for electron effective mass determination. It is instructive to use this method for the same goal in order to get a deeper insight into this approach. As mentioned before, CR absorption spectroscopy is the most direct method for electron effective mass determination and was utilized by our group for the first time on GaAsN:Si. Our CR results were published in Ref. [45] and also presented more detailed in Chap. 4 of this thesis. Investigating the field-induced shift of a band-to-acceptor transition, like (e,C⁰) in GaAs also leads to the electron effective mass, as was shown for GaAs [133, 134, 172] and zinc telluride [34]. However, this method requires the precise identification of the band-to-acceptor transition. Nevertheless, it has been numerously applied to GaAsN in the past [101, 102]. We lack the confidence to identify this transition in GaAs_{1-x}N_x with $x > 0.095\%$ with certainty and use an alternative approach. The field-induced shift of the FE transition can theoretically be investigated for the same goal, as was shown by Refs. [2, 125, 127] on GaAsN. Due to a complicated and not fully understood field-induced shift of the valence band, we limit our study to the investigation of the reduced mass μ . The procedure is explained in the following.

6.2.1. Landau level approximation

External magnetic fields efficiently modulate energetic states of bulk semiconductors. In particular, they shift and quantize the energetic levels of all charged carriers. The ratio between the field strength and the electron-hole Coulomb interaction regulates

the modification of excitonic eigenstates [124], which are mostly relevant for PL studies. The effective exciton Rydberg

$$Ry [\text{eV}] = \frac{\mu e^4}{2(4\pi\epsilon_r\epsilon_0)^2 \hbar^2} = \frac{13.6}{\epsilon_r^2} \frac{\mu}{m_0} \quad (6.1)$$

defines the Coulomb energy scale with the exciton reduced mass

$$\frac{1}{\mu} = \frac{1}{m_e^*} + \frac{1}{m_h^*}. \quad (6.2)$$

It contains the electron and hole effective masses m_e^* and m_h^* , respectively. Furthermore, ϵ_0 and ϵ_r describe the dielectric constant of free space and of the material, respectively. As usual, \hbar , e and m_0 symbolize the Planck constant, the elementary charge and the electron rest mass. The characteristic energy scale of excitons in a magnetic field is the cyclotron energy

$$\hbar\omega_c [\text{eV}] = \frac{\hbar e B}{\mu} = 1.16 \cdot 10^{-4} \frac{m_0}{\mu} B [\text{T}] \quad (6.3)$$

with the magnetic field strength B and cyclotron frequency ω_c . The ratio

$$\gamma = \frac{\hbar\omega_c}{2Ry} \quad (6.4)$$

is a dimensionless parameter, which weights the magnetic field strength with respect to the electron-hole interaction. $\gamma \gg 1$ describes the high magnetic field limit, which corresponds to $B \gg 3.8$ T for GaAs with $Ry_{\text{GaAs}} = 4.2$ meV and $\mu_{\text{GaAs}} = 0.053m_0$ [124], and applies to our magneto-PL study. The energy dispersion of Bloch electrons and holes in magnetic fields can be calculated with the effective mass approximation [109, 124]. In the parabolic case, the energy is given by

$$E_c(k_z, n) = E_c^0 + \left(n + \frac{1}{2}\right) \frac{\hbar e B}{m_e} + \frac{\hbar^2 k_z^2}{2m_e} \quad (6.5)$$

$$E_v(k_z, n) = E_v^0 - \left(n + \frac{1}{2}\right) \frac{\hbar e B}{m_h} - \frac{\hbar^2 k_z^2}{2m_h}. \quad (6.6)$$

E_c^0 and E_v^0 describe the bottom and top of the conduction and valence band, respectively. Eqn. (6.5) - (6.6) illustrate how the magnetic field quantizes the bands

into so-called Landau levels with the characteristic quantum number $n = 0, 1, 2, \dots$. In the high-field limit, we observe a linear increase of the band gap energy with magnetic field B , which is known as Landau level approximation. We can determine the reduced mass μ by investigating the magnetic shift

$$\Delta E_{\text{FE}}(k, n = 0) = E_c(k_z, 0) - E_v(k_z, 0) = \frac{\hbar e}{2\mu} B \quad (6.7)$$

of the FE energy, which is indirectly proportional to the slope of ΔE_{FE} . Consequently, the electron effective mass can be directly determined if the hole mass is known. More details on behalf of the magnetic field behavior of electronic states can be found in Refs. [109, 124].

6.2.2. Reduced mass of GaAsN with low N content

Because of the merged character of FE/EHP and LE-band transitions in GaAsN:Si, only intrinsic GaAsN samples are studied in this section. Fig. 6.5 demonstrates the

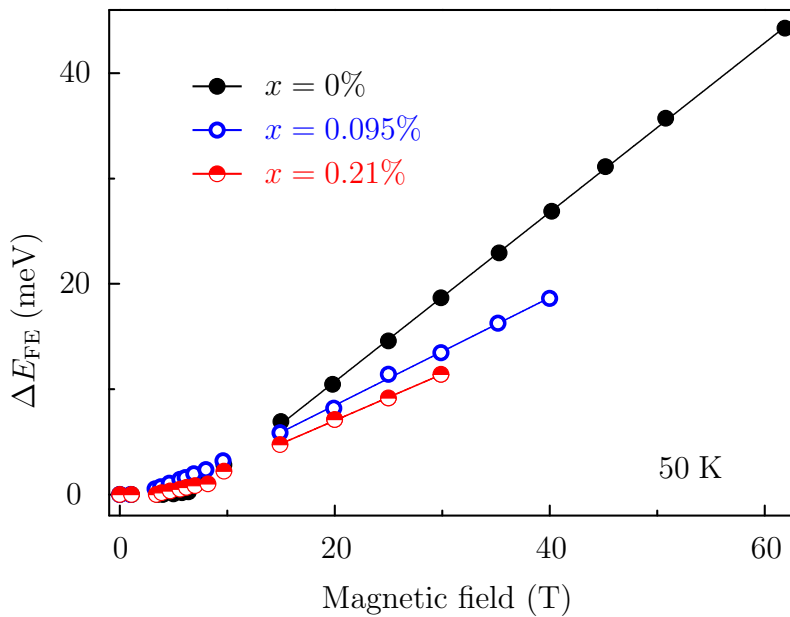


Figure 6.5.: Field-induced shift of the FE/EHP transition of $\text{GaAs}_{1-x}\text{N}_x$ with $x = 0\%$ (full circles), $x = 0.095\%$ (empty circles) and $x = 0.21\%$ (half-empty circles). Solid lines represent linear fits of the magnetic shift in the high-field limit.

field-induced shift of the FE transition ΔE_{FE} in GaAs $_{1-x}$ N $_x$:Si with $x = 0\%$ (VN459) and undoped GaAs $_{1-x}$ N $_x$ with $x = 0.095\%$ (K105) and $x = 0.21\%$ (K106) at 50 K. The corresponding magneto-PL spectra are shown in Fig. 6.2. Obviously, the FE transition is most dominant in all samples at 50 K and can easily be distinguished from other peaks. In the low-field limit, the FE transition shifts quadratically to higher energies when the magnetic field increases. This diamagnetic shift can be observed for approximately $0 \text{ T} \leq B \leq 6 \text{ T}$ in Fig. 6.5. The blue-shift is linear for $B \geq 15 \text{ T}$ and can be fitted with Eq. (6.7), as shown with solid lines in Fig. 6.5. Comparing the slopes ΔE_{FE} of the different samples, it is obvious that the magnetic blue-shift is significantly reduced by nitrogen incorporation. This observation is in agreement with previous magneto-PL results [102]. Using the arguments from Sec. 6.2.1, we expect an elevated reduced mass in N-containing samples. However, the slope of ΔE_{FE} is almost similar in both samples with $x > 0\%$. The same must be valid for the reduced masses. In order to get quantitative results, the slopes are linearly fitted with Eq. (6.7) in the high-field limit for $B \geq 15 \text{ T}$. The results are summarized in Tab. 6.1.

	VN463	K105	K106
N content	0%	0.095%	0.21%
Si-doping	yes	no	no
μ (kg)	$5.76 \cdot 10^{-32}$	$6.91 \cdot 10^{-32}$	$7.51 \cdot 10^{-32}$
μ (m_0)	0.072	0.113	0.131

Table 6.1.: Fit results for the reduced mass in VN463, K105 and K106 with Eq. (6.7).

The accepted value of the reduced mass in GaAs lies between $0.052 m_0$ and $0.058 m_0$ [123]. However, our enhanced reduced mass of $\mu = 0.072 m_0$ exactly corresponds to the published result of another study with Landau level approximation [129] on undoped GaAs. It was performed with magneto-PL in the range between 15 T and 30 T. Even though a perfectly linear shift of ΔE_{FE} was already obtained between 15 T and 30 T in Ref. [129], a better agreement with accepted reduced mass values was expected for higher magnetic fields by the author of that study. Our magneto-PL study suggests something else. Further investigations are necessary to clarify the discrepancy between the reduced masses. However, it is very unlikely that the perfect agreement between our result and Ref. [129] is accidental.

The reduced masses of the N containing samples are significantly enhanced in comparison to the reference sample. However, the difference is rather small between both N samples. Unfortunately, we cannot draw any conclusions concerning the electron effective mass from this result. The field-induced shift of the valence band is already very complicated in GaAs and not well-understood in GaAsN. Consequently, we only conclude that the reduced mass increases in GaAsN in comparison to GaAs.

6.3. Summary and outlook

A detailed magneto-photoluminescence (magneto-PL) study of GaAsN and GaAsN:Si is presented in this chapter. The magnetic field behavior of different transitions is investigated. The free exciton/electron-hole plasma (FE/EHP) transition is the most dominant peak of undoped GaAs_{1-x}N_x with $x \leq 0.2\%$ for $T > 50$ K. However, it exhibits a diminished blue-shift in the magnetic field compared to GaAs and vanishes above a critical field value. This critical field increases with the lattice temperature and lies between 30 T and 45 T in intrinsic GaAs_{1-x}N_x with $x = 0.095\%$ (K105) and $x = 0.21\%$ (K106). Since the coupling of Wannier excitons can be neglected in the high-field limit, excited carriers preferentially relax non-radiatively towards cluster states and form localized excitons (LEs). These LEs are the most dominant radiant transitions at high magnetic fields at all temperatures. In case of the Si-doped GaAsN samples, the FE/EHP merges with the LE-band. Both transitions cannot be investigated separately. Nevertheless, the merged spectral band exhibits a varying magnetic field response below and above 35 T. This indicates that the FE/EHP-part of the merged band also vanishes at 35 T in GaAsN:Si.

LE-bands of undoped GaAsN and GaAsN:Si exhibit a blue-shift in magnetic fields and consequently have a partially delocalized character. Their magnetic field response can be explained in terms of the interexcitonic population transfer. The magnetic field lifts the conduction band minimum and reveals formerly hybridized cluster states. Furthermore, it reduces the effective Bohr radius of excitons. Thus, LEs with the smallest wave function overlap decouple from the LE-band on the low-energy side of the spectrum for $B \geq 10$ T. Simultaneously, formerly hybridized cluster states are split off the conduction band just below the conduction band minimum and

trap excitons. Consequently, a blue-shift of the LE-band can be obtained when the magnetic field rises.

The blue-shift of the LE-band is diminished in intrinsic GaAsN at higher temperatures. An increased thermal energy reduces the partially delocalized character of LE-bands and thus the interexcitonic transfer mechanism. Consequently, the population transfer of LEs only works below a critical temperature $20 \text{ K} < T < 50 \text{ K}$. This temperature is not determined exactly within this thesis and could be part of a follow-up project. The merged spectral band of GaAsN:Si is not significantly affected by a temperature increase. This indicates that the interexcitonic transfer of Si-doped GaAsN is more complex than in the undoped case.

The reduced mass is determined in GaAs:Si and two undoped GaAs_{1-x}N_x samples with $x = 0.095\%$ and $x = 0.21\%$, using a field-induced shift of the FE/EHP transition. A Landau level approximation is applied in the high-field limit. The investigation of the reference sample GaAs:Si allows to test the functionality of our measuring technique and analysis procedure. An excellent agreement with Ref. [129] is obtained. In analogy to Ref. [129], the determined mass lies 20% above accepted mass values of GaAs. We conclude that the reduced mass is enhanced in the high-field limit. Furthermore, the determined GaAsN masses are 1.5 times larger than in the reference. The difference between both N containing samples however is very small. A similar enhancement of the electron effective mass was obtained in GaAsN in comparison to GaAs [101].

Magneto-PL has been numerously applied in the past for effective mass determination in GaAsN. However, the determined masses are inconsistent among different groups (e.g. [101, 2]). Our experience with magneto-PL for effective mass determination shows that this method is prone to errors. In particular, a precise identification of the band-to-acceptor or FE transition is necessary. In case of the FE transition investigation, the field-induced shift of the valence band is rather complicated. Consequently, it is difficult to get reliable electron effective mass values with incomplete knowledge of hole effective masses in GaAsN. Nevertheless, it would be interesting to have more studies of the valence band behavior of GaAsN in high magnetic fields. The same is valid for the investigation of pure GaAs in high magnetic fields. In particular more theoretical investigations on magneto-excitons in GaAs and GaAsN would be of interest.

7. Conclusions and outlook

The purpose of this thesis is a detailed magneto-optical study of GaAsN in high magnetic fields. We applied different spectroscopic methods to the dilute nitride in order to study its electronic and optical properties. The highlights of this thesis are summarized in this chapter. Possible future investigations are proposed.

The first direct determination of the electron effective mass of GaAsN is an essential part of this work. We performed detailed cyclotron resonance (CR) absorption spectroscopy investigations in bulk Si-doped GaAsN samples with a nitrogen content of up to 0.2%. We used the unique combination of the large-scale facilities free-electron laser FELBE and the Dresden High Magnetic Field Laboratory for the implementation of terahertz spectroscopy in pulsed magnetic fields up to 62 T. A slight increase of the CR electron effective mass with N content is obtained in excellent agreement with calculations based on the band anticrossing model [136, 165] and empirical tight-binding predictions [141]. Furthermore, we observe an increase of the band nonparabolicity with increasing N concentration. This experimental result is in agreement with our calculations of the energy dependent momentum effective mass [147, 170] based on the band anticrossing model [136]. We obtain a strong decrease of the electron mobility in GaAsN:Si with CR spectroscopy, which matches formerly determined Hall mobility values [119]. In summary, our investigation led to a complete and consistent understanding of the so far controversially discussed GaAsN effective mass. Further investigations of GaAs_{1-x}N_x:Si with $x < 0.1\%$, $0.1\% < x < 0.2\%$ and $0.2\% < x < 0.5\%$ with CR absorption spectroscopy can provide additional quantitative details.

In the second part of this thesis, we performed continuous-wave photoluminescence (PL) in GaAsN and GaAsN:Si and investigate the different transitions of the systems. Furthermore, we studied the PL dynamics of GaAsN:Si. GaAs-related transitions (e, C^0) and (D^0-A^0) are identified besides localized excitons (LEs) in the PL of intrinsic GaAs_{1-x}N_x with $x = 0.095\%$. The latter emerge in a LE-band at low temperatures

and also contribute to the low-energy tail with a lower interexcitonic population transfer. Increasing the N content red-shifts the PL because of a N-induced band gap reduction [162, 136]. Furthermore, distinct PL peaks broaden and smear out to a nearly featureless LE-band. This band exhibits a partially delocalized character because of overlapping exciton wave functions and an efficient interexcitonic transfer. A reduced lattice quality increases non-radiative relaxation processes and considerably decreases the radiation yield in comparison to the $x = 0.095\%$ sample. The PL of Si-doped $\text{GaAs}_{1-x}\text{N}_x$ is dominated by merged spectral bands. They have contributions of localized excitons (LEs), free excitons (FEs) and of the electron-hole plasma (EHP) on the high-energy side of the spectrum. In case of $\text{GaAs}_{0.998}\text{N}_{0.002}$, the LE/FE/EHP-band of the Si-doped sample is blue-shifted with respect to the one of intrinsic GaAsN. Similar to an illumination power increase, Si-incorporation leads to a higher occupation rate of different cluster states and thus to a partially suppressed LE transfer towards lower lying cluster states. Consequently, more high-energy LEs contribute to the spectral band of GaAsN:Si. This band is systematically studied with time-resolved PL in GaAsN:Si for the first time. The PL decay is predominantly monoexponential and has a strong energy dispersion. The determined maximum decay times of GaAsN:Si are significantly reduced in comparison to undoped GaAsN epilayers [29, 27]. Consequently, Si reduces the decay time of GaAsN to a greater extent as in GaAs. The determination of a quantitative relationship between the decay time reduction of GaAs:Si and GaAsN:Si could be part of a follow-up project. A GaAsN:Si sample series with a constant N content and varying Si-doping should be investigated for this purpose.

A detailed magneto-PL study of GaAsN and GaAsN:Si in pulsed magnetic fields up to 62 T is presented in the third part of this thesis. LE-bands dominate the PL at high magnetic fields in all samples. Because of their partially delocalized character, they exhibit a blue-shift in rising magnetic fields, which can be explained with the interexcitonic transfer mechanism. However, the blue-shift is diminished in intrinsic GaAsN at higher temperatures. Thus, the population transfer of LEs is only active below a critical temperature $20 \text{ K} < T < 50 \text{ K}$. The determination of the exact critical temperature could be part of a follow-up project. In case of GaAsN:Si, a temperature increase has no significant impact on the delocalized character of the merged LE/FE/EHP band. Consequently, the interexcitonic transfer of Si-doped GaAsN is more complex than in undoped GaAsN. The reduced mass of undoped

GaAsN and GaAs:Si is investigated by exploiting the observed field-induced shift of the FE/EHP transition in the high-field limit. In case of the reference sample, an excellent agreement with Ref. [129] is obtained. However, the determined mass lies 20% above accepted mass values of GaAs, in analogy to Ref. [129]. This exciting result should be investigated further in a follow-up project. In particular, the complicated field-induced shift of the valence band should be in the focus. The determined GaAsN masses are 1.5 times larger than in the reference. A similar increase of the electron effective mass of GaAsN was obtained before [101]. Our magneto-PL study shows that it is worth it to perform further investigations on GaAsN and pure GaAs in very high magnetic fields. More theoretical investigations on magneto-excitons in GaAs and GaAsN would also be of interest.

A. Appendix

A.1. Overview of the investigated samples

Different GaAsN samples are investigated in this thesis. The VN sample series consists of molecular beam epitaxy (MBE) grown, silicon n-doped $\text{GaAs}_{1-x}\text{N}_x\text{:Si}$ samples with $x = 0.1\% - 0.5\%$. The samples were grown by M. Hopkinson and coworkers at the University of Sheffield. In particular, the GaAsN layer was grown on a semi-insulating GaAs substrate at a lowered growing temperature of 500°C on top of a 20 nm GaAs buffer layer grown at 580°C . The thickness of the nitrogen containing layer is $1\ \mu\text{m}$ and the n-doping is nominally $1 \cdot 10^{17}\ \text{cm}^{-3}$. The N content was monitored by x-ray diffraction. In addition to these samples, two undoped $\text{GaAs}_{1-x}\text{N}_x$ samples K105 and K106 with a nitrogen content of $x = 0.095\%$ and $x = 0.21\%$, respectively, are investigated in our PL-studies. These samples were grown by metalorganic vapour phase epitaxy (MOVPE) by W. Stolz and coworkers at the Philipps-Universität Marburg [77]. They were deposited pseudomorphically on semi-insulating (100) GaAs substrates. The chosen GaAs substrates and buffer layers have a thickness of $500 \pm 25\ \mu\text{m}$ and 250 nm, respectively. For both samples, the GaAsN layer is 500 nm. The source materials were triethylgallium, 1,1-dimethylhydrazine, and tertiarybutyl arsine. Our CR spectroscopy study is only performed on samples of the VN series. Photoluminescence and magneto-photoluminescence is applied to both VN-series and K-series. Tab. A.1 shows an overview of all investigated samples.

Sample name	VN459	VN460	VN461	VN463	K105	K106
N content x (%)	0.1	0.2	0.5	0	0.095	0.21
Layer thickness (μm)	1	1	1	1	0.5	0.5
Growth technique	MBE	MBE	MBE	MBE	MOVPE	MOVPE

Table A.1.: Characteristics of the $\text{GaAs}_{1-x}\text{N}_x$ samples studied in this work.

A.2. Experimental parameters for magneto-PL in the HLD

Tab. A.2 gives an overview of the experimental details for the realization of magneto-PL experiments in pulsed magnetic fields of the HLD. In particular, it shows the coil voltages and acquisition times. The desired magnetic field strength is defined by

B (T)	1	3	4	5	6	7	8	9	10		
ΔB (T)	0.38	0.26	0.33	0.42	0.45	0.50	0.60	0.40	0.50		
V (kV)	0.78	0.78	1.30	1.70	2.00	2.20	2.50	2.85	3.38		
Modules	1	6,7,8	6,7,8	6,7,8	6,7,8	6,7,8	6,7,8	6,7,8	6,7,8		
t_1 (ms)	28.55	40.43	40.43	40.40	40.70	40.70	40.70	42.37	42.37		
t_2 (ms)	48.07	59.96	59.96	59.92	60.22	60.22	60.22	57.24	57.24		
t_L (ms)	20.55	32.43	32.43	32.40	32.70	32.70	32.70	34.37	34.37		
Δt_L (ms)	27.52	27.52	27.52	27.52	27.52	27.52	27.52	22.87	22.87		
t_S (ms)	28.55	40.43	40.43	40.40	40.70	40.70	40.70	42.37	42.37		
Δt_S (ms)	18.52	18.52	18.52	18.52	18.52	18.52	18.52	13.87	13.87		
Δt (ms)	19.52	19.52	19.52	19.52	19.52	19.52	19.52	14.87	14.87		
	15	20	25	30	35	40	45	50	55	60	
	0.56	0.75	0.70	0.80	0.80	0.80	0.73	0.80	0.89	1.00	
	5.20	6.90	8.70	10.40	12.30	14.00	15.80	17.80	19.60	22.00	
	6,7,8	6,7,8	6,7,8	6,7,8	6,7,8	6,7,8	6,7,8	6,7,8	6,7,8	6,7,8	
	43.23	42.91	43.97	44.35	44.44	44.61	44.99	44.85	44.55	44.10	
	56.52	56.2	55.46	54.83	54.46	53.98	53.43	53.30	53.00	52.55	
	35.23	34.91	35.97	36.35	36.44	36.61	36.99	36.85	36.55	36.10	
	21.29	21.29	19.49	18.49	18.02	17.37	16.44	16.45	16.45	16.45	
	43.23	42.91	43.97	44.35	44.44	44.61	44.99	44.85	44.55	44.10	
	12.29	12.29	10.49	9.49	9.02	8.37	7.44	7.45	7.45	7.45	
	13.29	13.29	11.49	10.49	10.02	9.37	8.44	8.45	8.45	8.45	

Table A.2.: Overview of the experimental details in regards to the magnetic field strength B , the required voltage values V , the chosen field variation ΔB and integration time $\Delta t = t_2 - t_1$ for certain capacitor modules. The times t_1 and t_2 were chosen symmetrically around the magnetic field maximum. A magnetic field delay of 5 ms after the trigger time t_{tr} had to be considered and resulted in new $t_{1,2} = t_{tr} + 5 \text{ ms} + t_{1,2}^{\text{old}}$ values. The delay times of the laser t_L , Δt_L and spectrometer t_S , Δt_S for the delay generator are defined as follows: $t_L = t_1 - 8 \text{ ms}$, $\Delta t_L = \Delta t + 8 \text{ ms}$, $t_S = t_1$, $\Delta t_S = \Delta t - 1 \text{ ms}$.

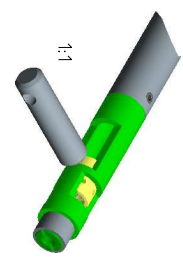
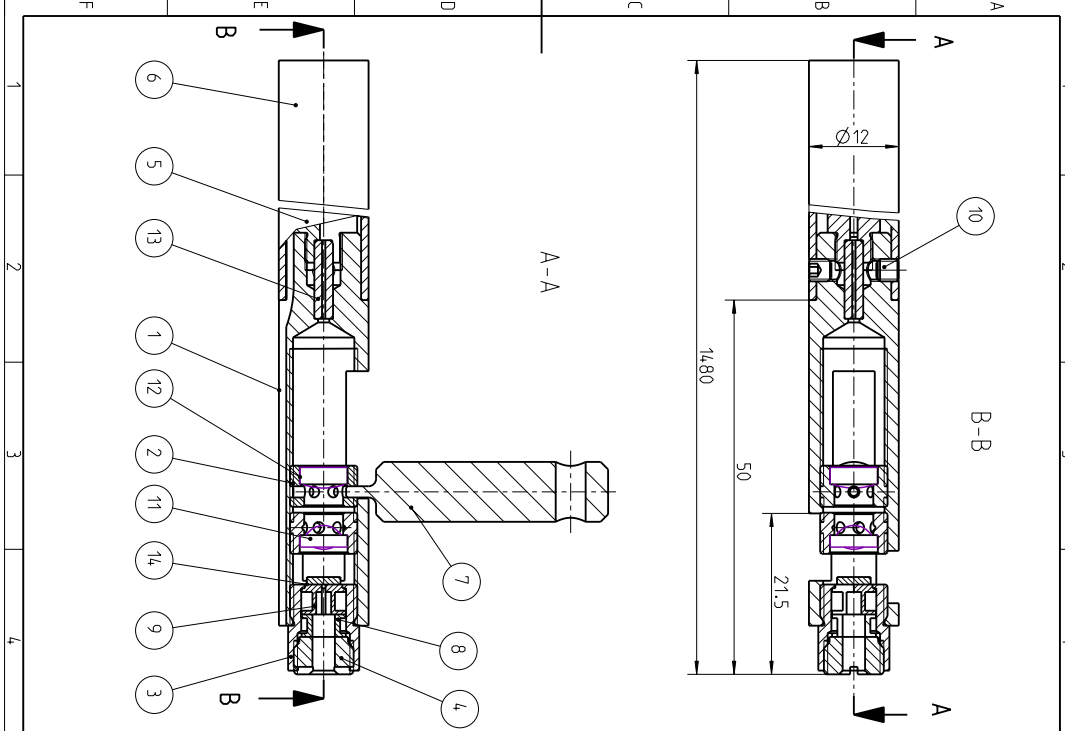
the applied voltage, but can vary with the actual coil temperature and is strongly dependent on the particular capacitor module. Thus, it is advisable to always use the same module set and constantly monitor the actual field strength with a pick-up coil. All experiments were performed with the modules 6, 7, 8, except of the 1 T pulses, which were realized with module 1.

A.3. Detailed drawings for the magneto-PL probe

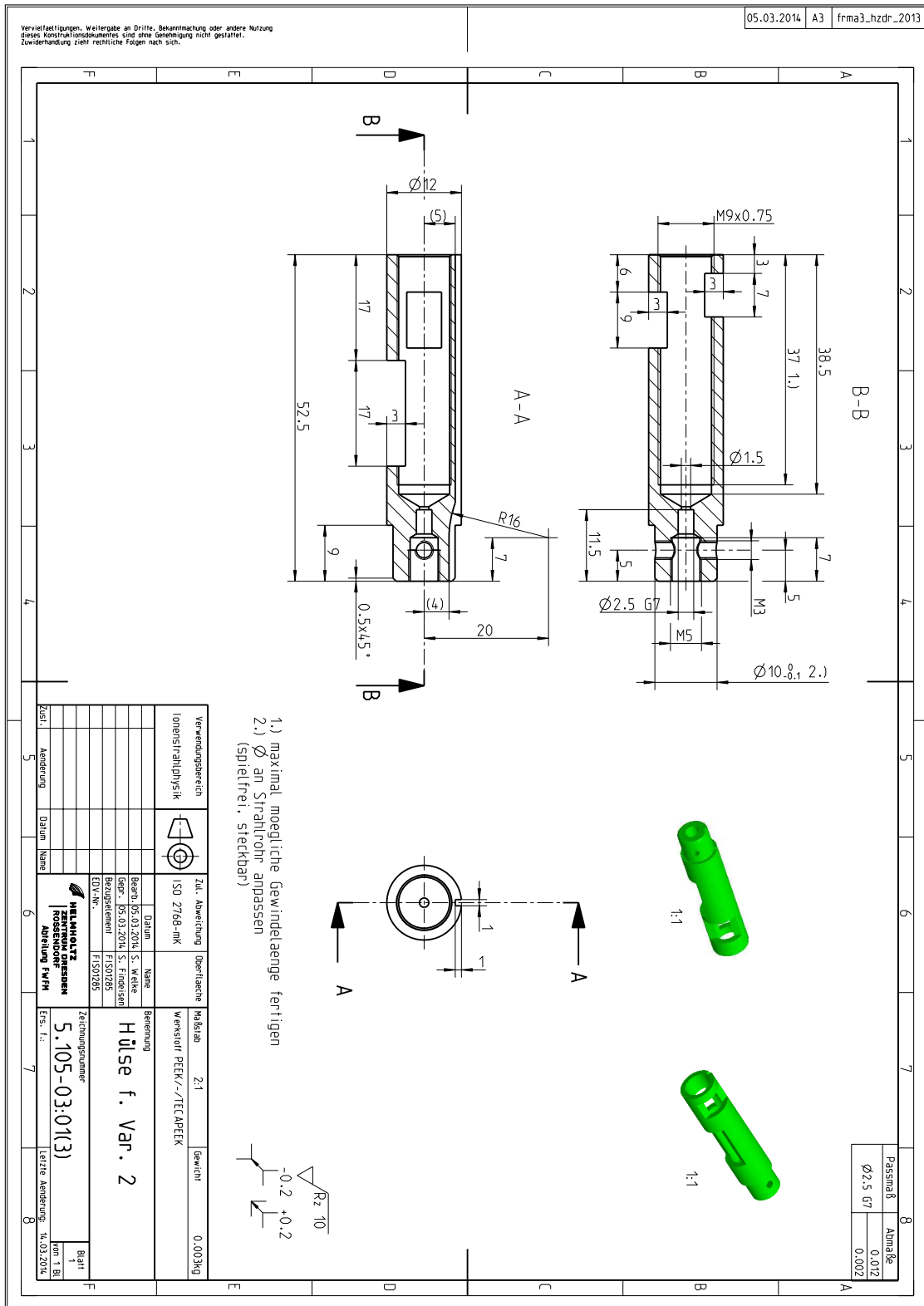
A new experimental setup was built for magneto-PL measurements in pulsed magnetic fields of the HLD in the framework of this PhD. This setup is described in detail in Sec. 3.3.1. In particular, a special measuring probe was constructed for this task, as discussed before. In this section, detailed drawings for the construction of this probe are shown. They were prepared in cooperation with Stefan Findeisen who is employed in the division of mechanical engineering (FWFM) of the HZDR. The actual production was carried out by the central workshop of the HZDR. The technical drawings are presented in the following.

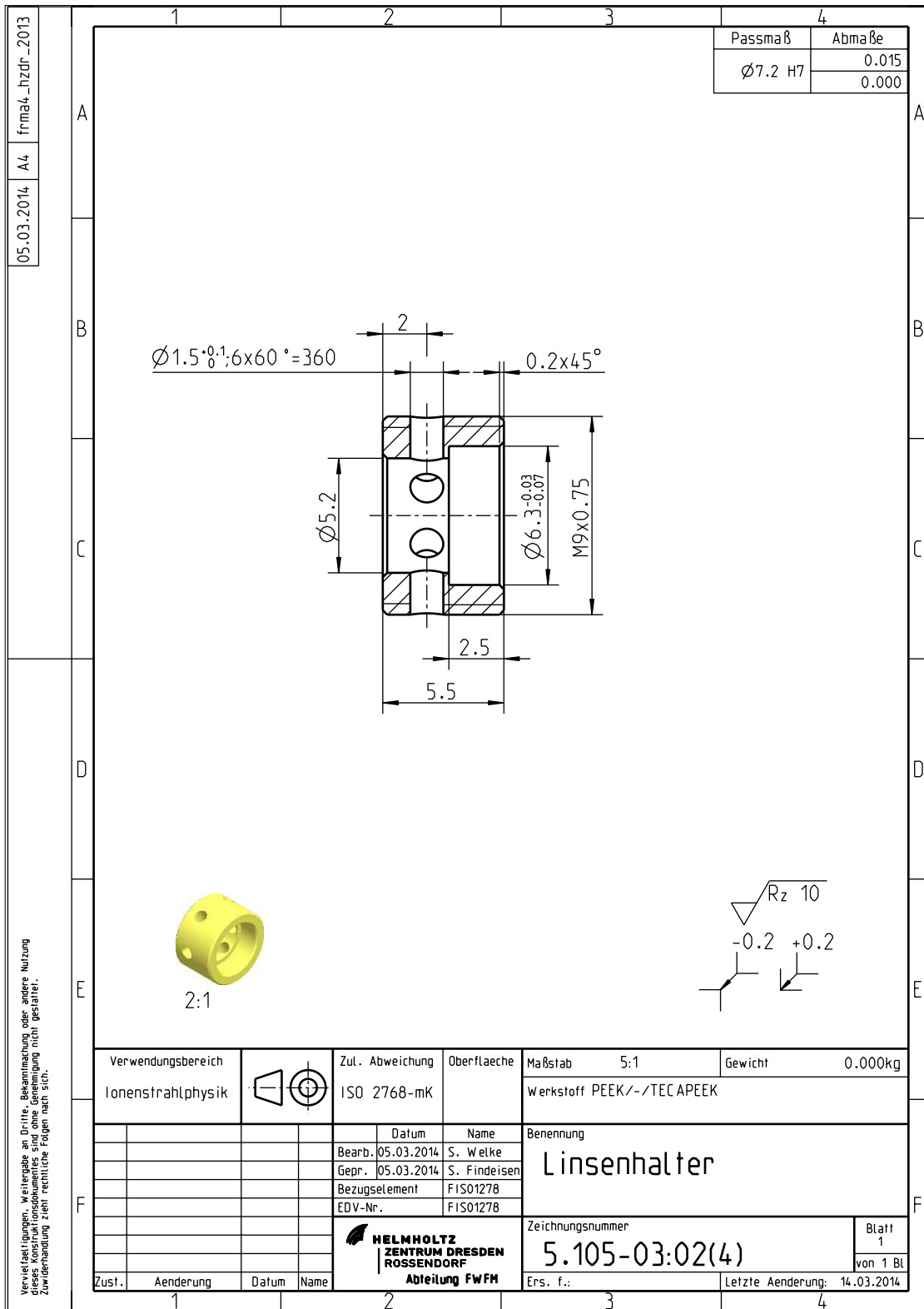
05.03.2014 A3 frma3_hzdr_2013

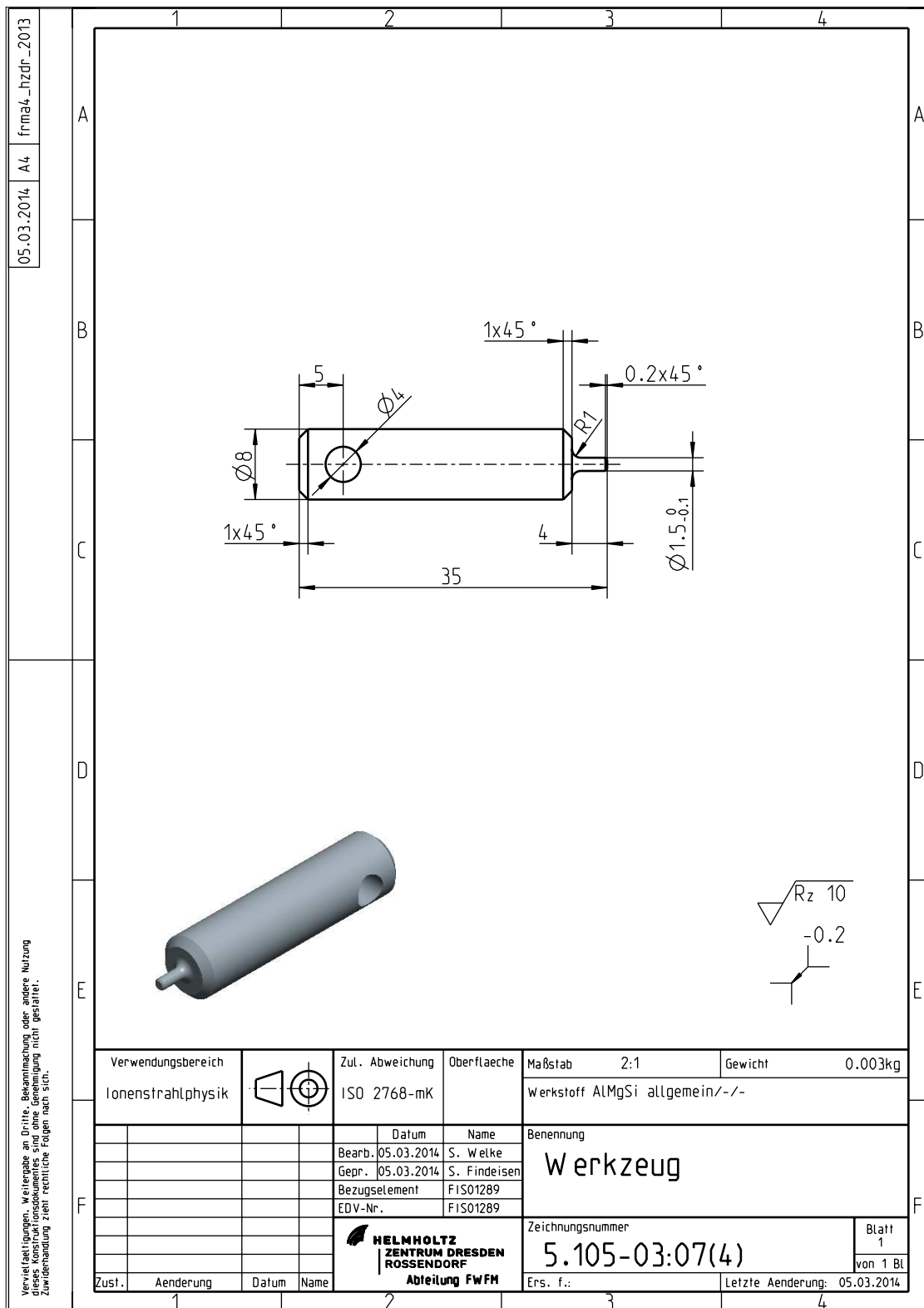
Vervielfältigungen, Weitergabe an Dritte, Bekanntmachung oder andere Nutzung dieses Konstruktionsdokumentes sind ohne Genehmigung nicht gestattet.
Zwischenhandlung zehrt rechtliche Folgen nach sich.



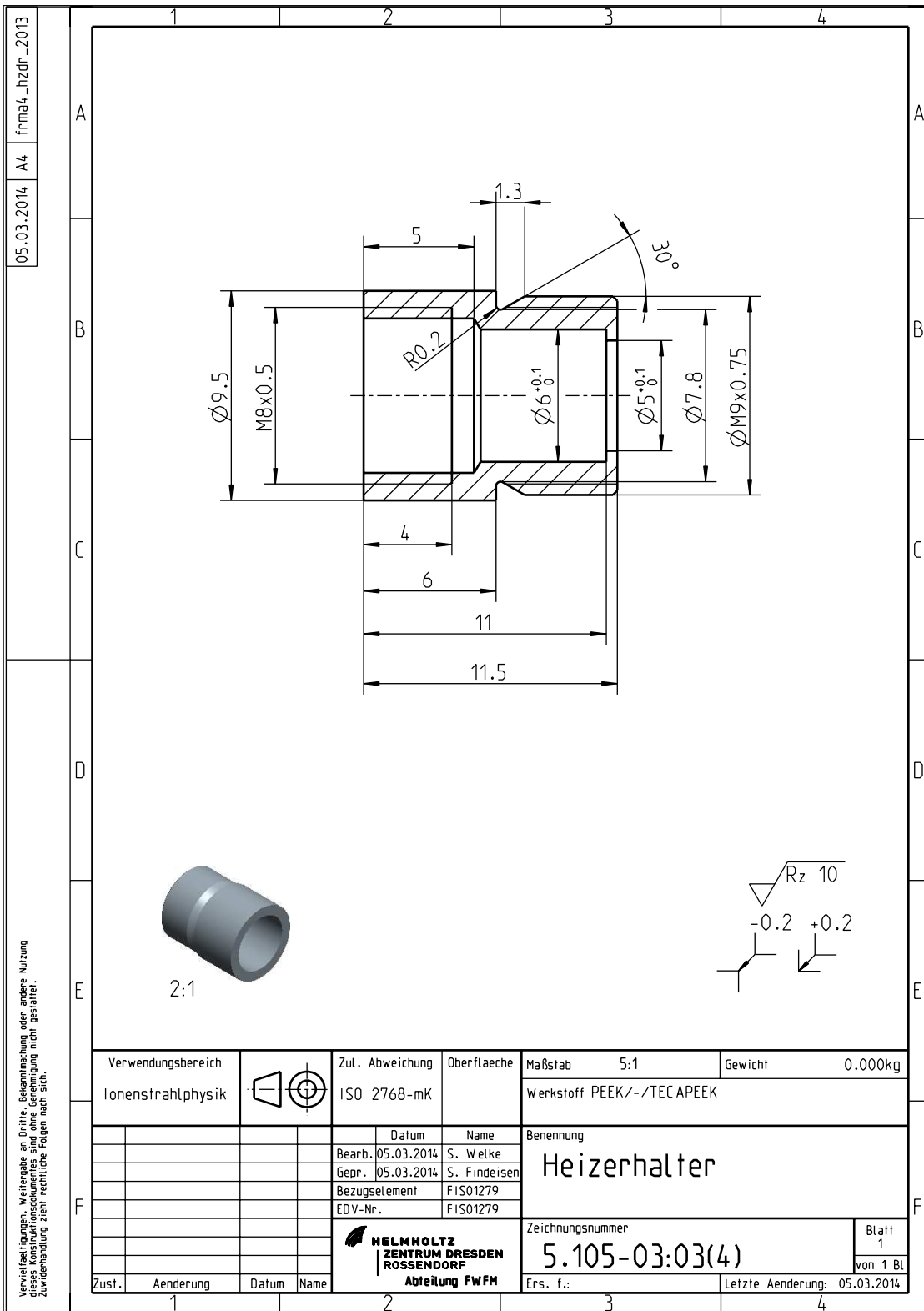
14	1	Probe									
13	1	FC/SC Multimode Ferrule	CF440-10						vorhanden		
12	1	Aspheric collimating lens	20369-E01						THORLABS		
11	1	Aspheric collimating lens	17805-E01						THORLABS		
10	2	Gewindestift	ISD 4026 M3x3-A2								
9	1	Heizer	5.105-01;04(4)								
8	1	pic-up-Spule	5.105-03;08(4)								
7	1	Werkzeug	5.105-03;07(4)						Montagehilfe		
6	1	Stahlrohr	5.105-03;06(4)								
5	1	Ferrulenschluss	5.105-03;05(4)								
4	1	Verschluss	5.105-03;04(4)								
3	1	Heizerhalter	5.105-03;03(4)								
2	2	Linsehalter	5.105-03;02(4)								
1	1	Hülse f. Var. 2	5.105-03;01(3)								
Pos. i.ME		Benennung	Sachnummer/kurzbezeichnung						Bemerkung		
1		Verwendungsreich									
2		Ionenstrahlphysik									
3		ISO 2768-mk									
4		Masstab	2:1								
5		Gewicht	0.400kg								
Datum: Bearb. 05.03.2014 St. Werke Genehm. 05.03.2014 St. Filialen Bezugszeichen: F501290 EDV-Nr.: F501290				HELIUMLABZ ЗЕТРОН ДИСТОН КОСМОСДОН ИОННЫЙ ПУЛТ				Benennung: Fotolumineszenz-Prob Variante 2 Zeichnungsnummer: 5.105-03(3)			
Zust.	Aenderung	Datum	Name	Ers.-f.		letzte Aenderung		Blatt			
5				1		4.03.2014		1 von 1 Bl			

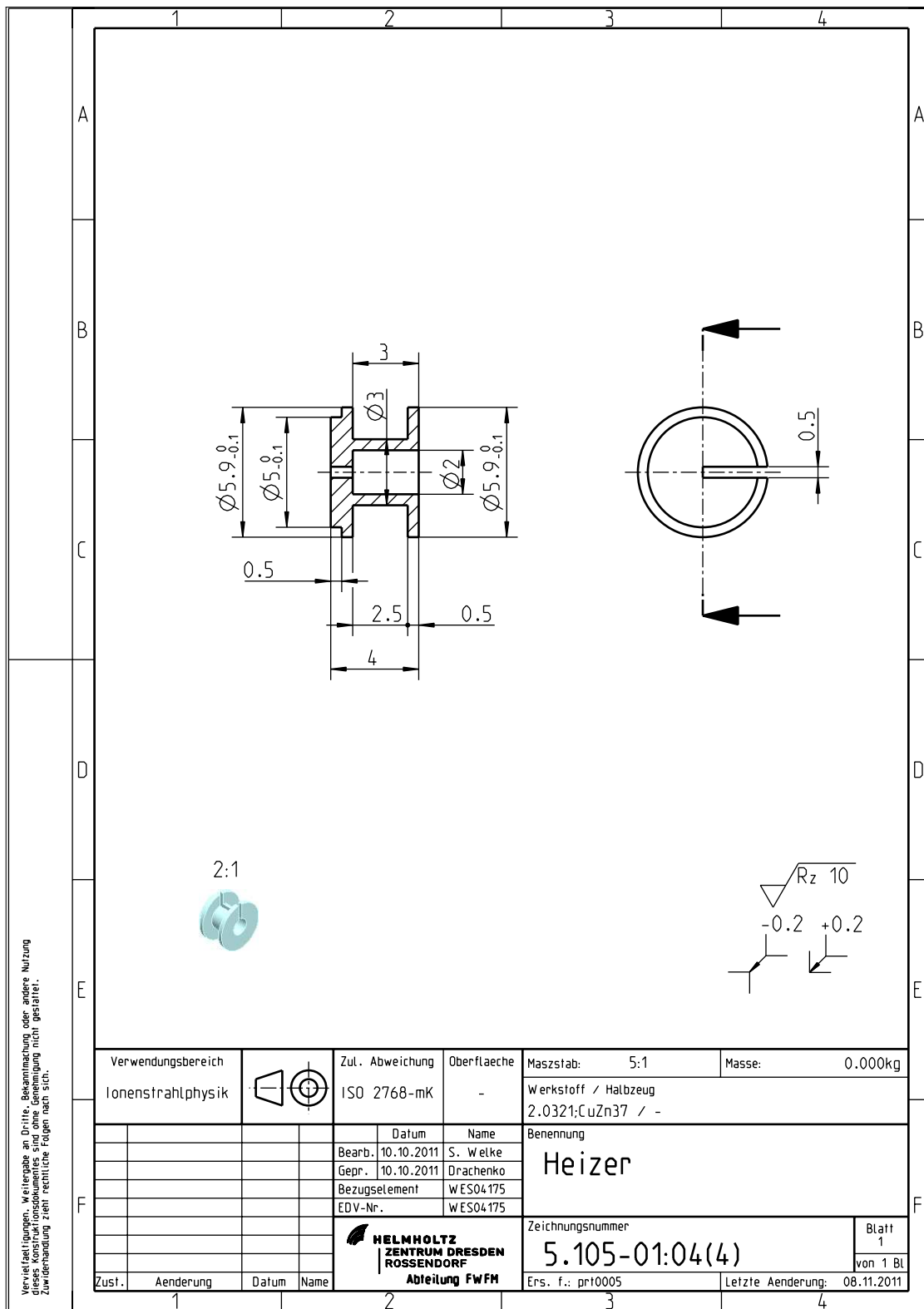




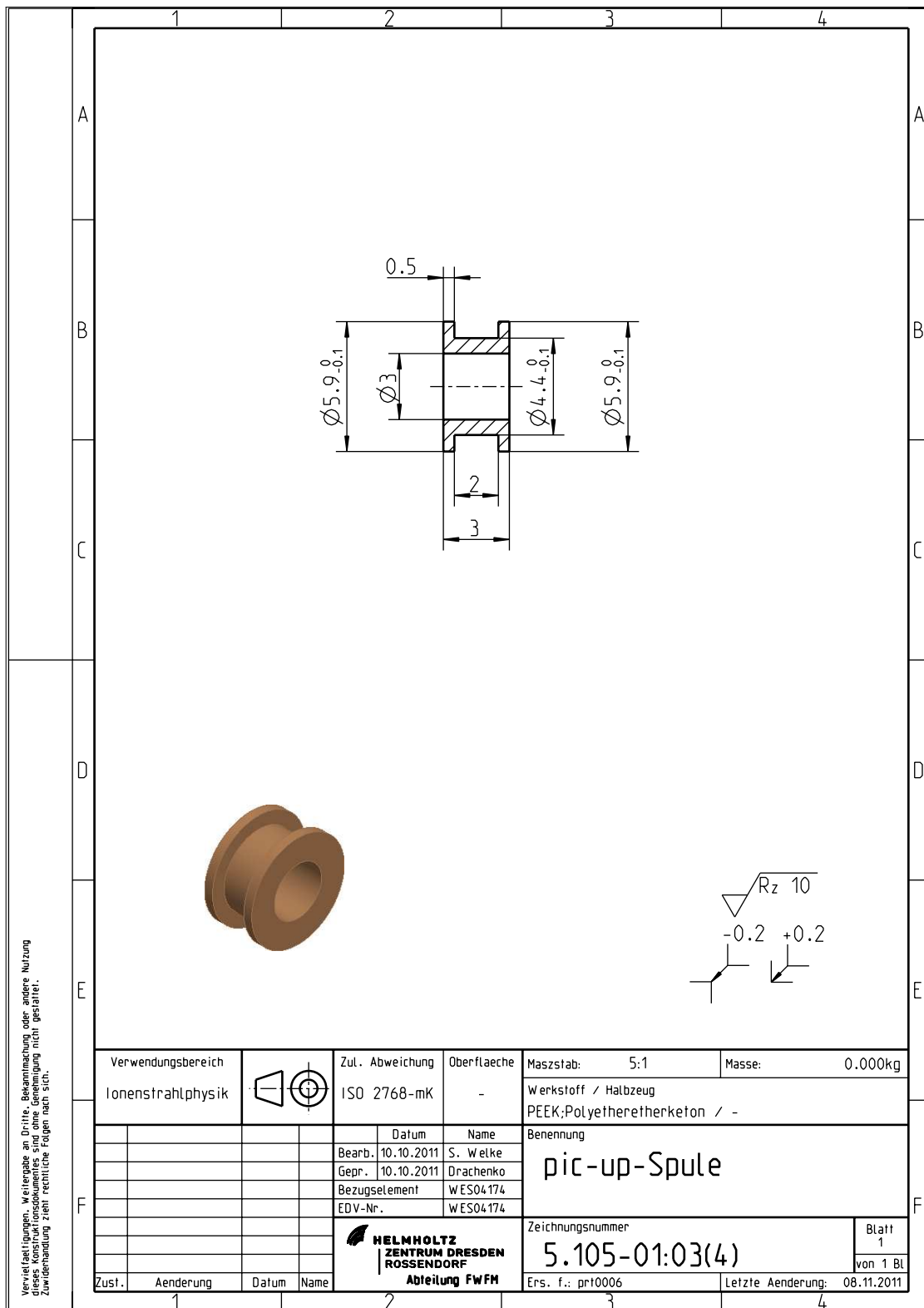


Vervielfaelligungen, Weitergabe an Dritte, Bekannmachung oder andere Nutzung
 dieses Konstruktionsdokumentes sind ohne Genehmigung nicht gestattet.
 Zuwiderhandlung zeh. rechtliche Folgen nach sich.

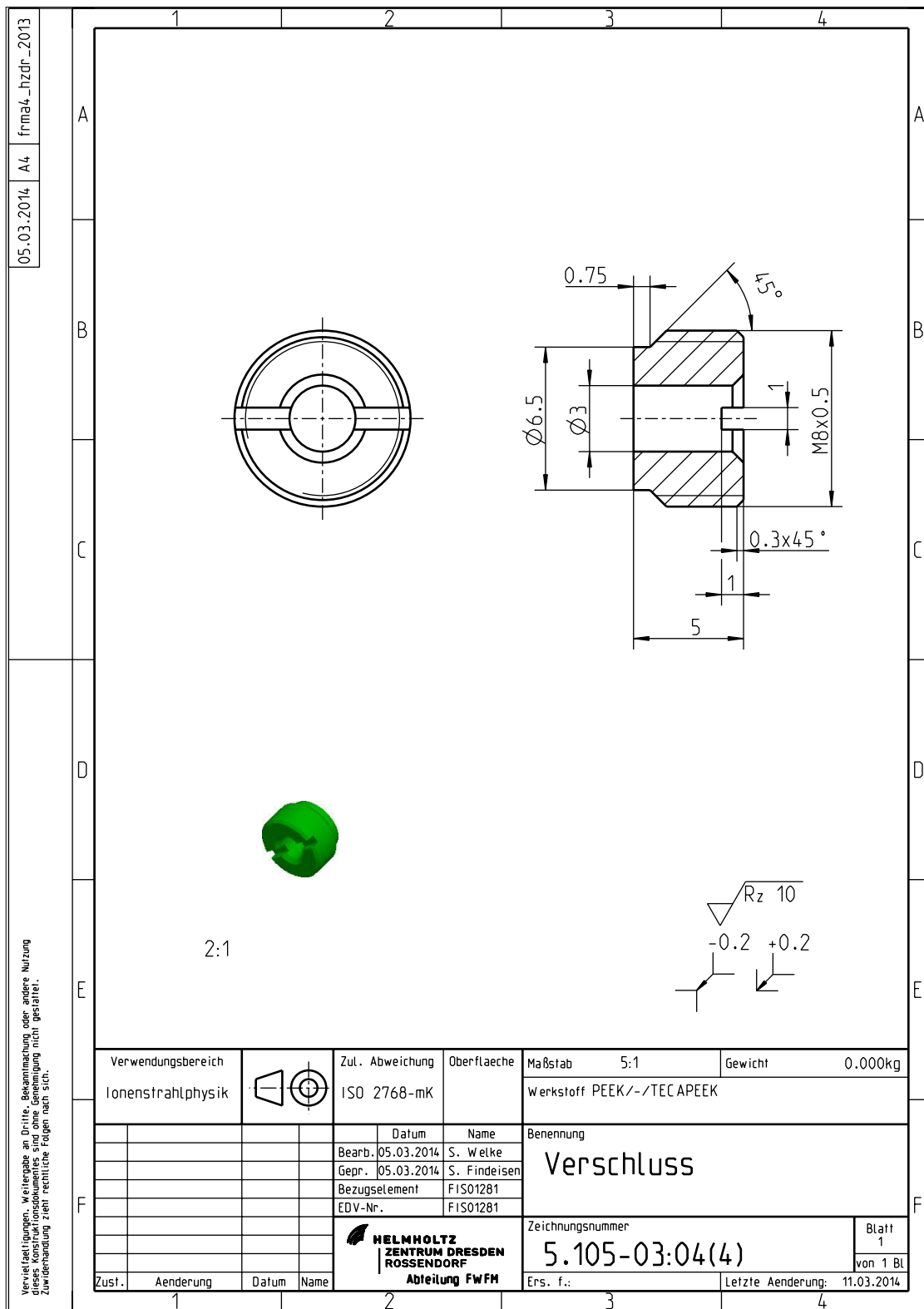




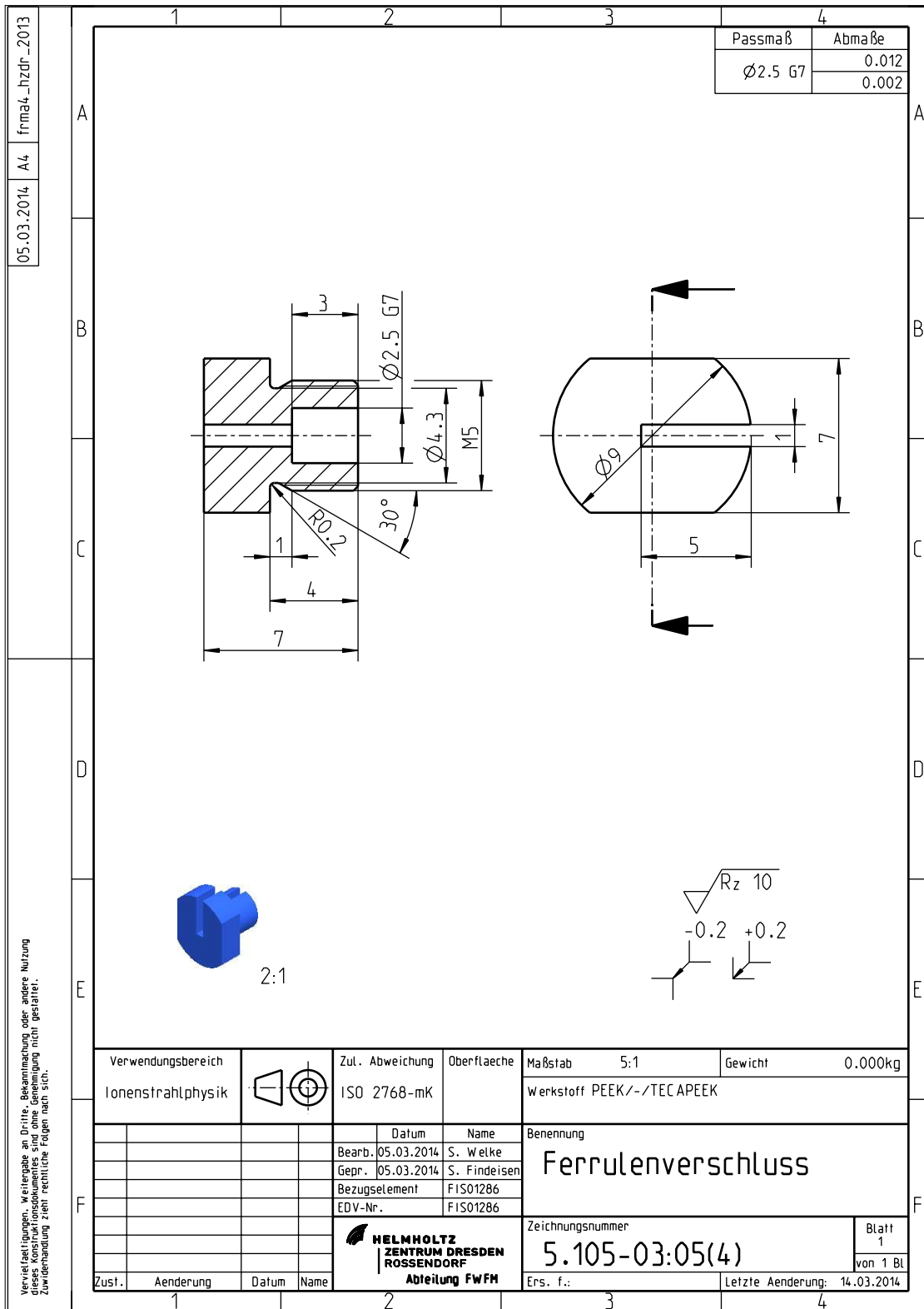
Vervielfaechigungen, Weitergabe an Dritte, Bekannmachung oder andere Nutzung
 dieses Konstruktionsdokumentes sind ohne Genehmigung nicht gestattet.
 Zuwiderhandlung zueh. rechtliche Folgen nach sich.



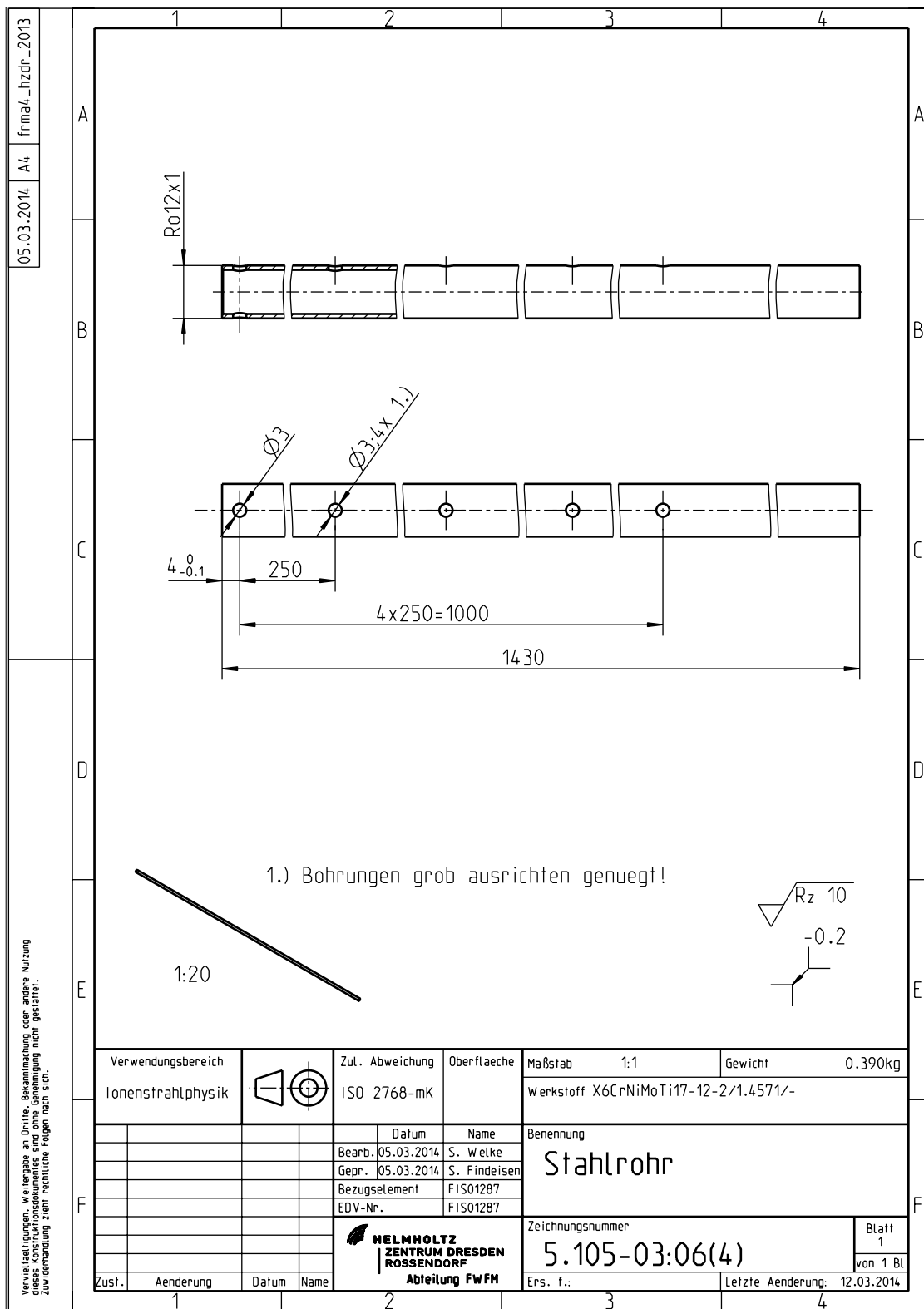
Vervielfaelligungen, Weitergabe an Dritte, Bekanntmachung oder andere Nutzung
 dieses Konstruktionsdokumentes sind ohne Genehmigung nicht gestattet.
 Zuwiderhandlung zueh. rechtliche Folgen nach sich.



Vervielfaechigungen, Weitergabe an Dritte, Bekanntmachung oder andere Nutzung
 dieses Konstruktionsdokumentes sind ohne Genehmigung nicht gestattet.
 Zuwiderhandlung zueh. rechtliche Folgen nach sich.



Vervielfaelligungen, Weitergabe an Dritte, Bekanntmachung oder andere Nutzung dieses Konstruktionsdokumentes sind ohne Genehmigung nicht gestattet. Zuwiderhandlung zeh. rechtliche Folgen nach sich.



Bibliography

- [1] S. Adachi. *Properties of semiconductor alloys: group-IV, III-V and II-VI semiconductors*. John Wiley & Sons, Ltd, 2009.
- [2] K. Alberi, S. A. Crooker, B. Fluegel, D. A. Beaton, A. J. Ptak, and A. Mascarenhas. Magnetic-field-induced delocalized to localized transformation in GaAs:N. *Phys. Rev. Lett.*, 110:156405, 2013.
- [3] K. Alberi, B. Fluegel, D. A. Beaton, A. J. Ptak, and A. Mascarenhas. Localization-delocalization transition of electrons at the percolation threshold of semiconductor GaAs_{1-x}N_x alloys: The appearance of a mobility edge. *Phys. Rev. B*, 86(4):041201(R), 2012.
- [4] F. Alexandre. Chapter 2 - Epitaxial growth of dilute nitrides by metal-organic vapour phase epitaxy. In M. Henini, editor, *Dilute nitride semiconductors*, pages 93 – 117. Elsevier, Amsterdam, 2005.
- [5] P. W. Anderson. Localized magnetic states in metals. *Phys. Rev.*, 124(1):41 – 53, 1961.
- [6] J. R. Apel, T. O. Poehler, C. R. Westgate, and R. I. Joseph. Study of the shape of cyclotron-resonance lines in indium antimonide using a far-infrared laser. *Phys. Rev. B*, 4:436 – 451, 1971.
- [7] D. J. Ashen, P. J. Dean, D. T. J. Hurle, J. B. Mullin, A. M. White, and P. D. Greene. The incorporation and characterisation of acceptors in epitaxial GaAs. *J. Phys. Chem. Solids*, 36(10):1041 – 1053, 1975.
- [8] S. R. Bank, H. P. Bae, H. B. Yuen, M. A. Wistey, L. L. Goddard, and J. S. Harris Jr. Room-temperature continuous-wave 1.5 μm GaInNAsSb laser on GaAs. *Electron. Lett.*, 42(3):156 – 157, 2006.

- [9] S. R. Bank, M. A. Wistey, L. L. Goddard, H. B. Yuen, V. Lordi, and J. S. Harris. Low-threshold continuous-wave 1.5 μm GaInNAsSb lasers grown on GaAs. *Quantum Electronics, IEEE*, 40(6):656 – 664, 2004.
- [10] M. Baranowski, R. Kudrawiec, M. Latkowska, M. Syperek, J. Misiewicz, and J. A. Gupta. Dynamics of localized excitons in $\text{Ga}_{0.69}\text{In}_{0.31}\text{N}_{0.015}\text{As}_{0.985}/\text{GaAs}$ quantum well: Experimental studies and Monte-Carlo simulations. *Appl. Phys. Lett.*, 100(20):202105, 2012.
- [11] M. Baranowski, M. Latkowska, R. Kudrawiec, and J. Misiewicz. Model of hopping excitons in GaInNAs: simulations of sharp lines in micro-photoluminescence spectra and their dependence on the excitation power and temperature. *J. Phys. Condens. Mat.*, 23(20):205804, 2011.
- [12] Bastard, G. *Wave mechanics applied to semiconductor heterostructures*. Wiley, New York, 1990.
- [13] C. Becker, C. Sirtori, O. Drachenko, V. Rylkov, D. Smirnov, and J. Leotin. GaAs quantum box cascade lasers. *Appl. Phys. Lett.*, 81(16):2941 – 2943, 2002.
- [14] L. Bellaiche, S.-H. Wei, and A. Zunger. Composition dependence of interband transition intensities in GaPN, GaAsN, and GaPAs alloys. *Phys. Rev. B*, 56:10233 – 10240, 1997.
- [15] H. Benaissa, A. Zaoui, and M. Ferhat. First principles calculations for dilute $\text{InAs}_{1-x}\text{N}_x$ alloys. *J. Appl. Phys.*, 102(11):113712, 2007.
- [16] G. Bentoumi, Z. Yaïche, R. Leonelli, J.-N. Beaudry, P. Desjardins, and R. A. Masut. Low-temperature emission in dilute GaAsN alloys grown by metalorganic vapor phase epitaxy. *J. Appl. Phys.*, 103(6):063526, 2008.
- [17] J. Bhattacharyya, M. Wagner, M. Helm, M. Hopkinson, L. R. Wilson, and H. Schneider. Terahertz activated luminescence of trapped carriers in In-GaAs/GaAs quantum dots. *Appl. Phys. Lett.*, 97(3), 2010.
- [18] W. G. Bi and C. W. Tu. Bowing parameter of the band-gap energy of $\text{GaN}_x\text{As}_{1-x}$. *Appl. Phys. Lett.*, 70(12):1608 – 1610, 1997.

-
- [19] J. S. Blakemore. Semiconducting and other major properties of gallium arsenide. *J. Appl. Phys.*, 53(10):R123 – R181, 1982.
- [20] L. Van Bockstal, G. Heremans, and F. Herlach. Coils with fibre composite reinforcement for pulsed magnetic fields in the 50-70 T range. *Meas. Sci. Technol.*, 2(12):1159 – 1164, 1999.
- [21] C. A. Brau. Free-electron lasers. *Science*, 239(4844):1115 – 1121, 1988.
- [22] F. Briones and D. M. Collins. Low temperature photoluminescence of lightly Si-doped and undoped MBE GaAs. *J. Electron. Mater.*, 11(4):847 – 866, 1982.
- [23] C. A. Broderick, M. Usman, S. J. Sweeney, and E. P. O'Reilly. Band engineering in dilute nitride and bismide semiconductor lasers. *Semicond. Sci. Tech.*, 27(9):094011, 2012.
- [24] I. A. Buyanova and W. M. Chen. Chapter 9 - Recombination processes in dilute nitrides. In I. A. Buyanova and W. M. Chen, editors, *Physics and applications of dilute nitrides*, pages 255 – 280. Taylor & Francis Books, Inc., New York, NY, 2004.
- [25] I. A. Buyanova and W. M. Chen, editors. *Physics and applications of dilute nitrides*, volume 21. Taylor & Francis Books, Inc., New York, NY, 2004.
- [26] I. A. Buyanova, W. M. Chen, G. Pozina, J. P. Bergman, B. Monemar, H. P. Xin, and C. W. Tu. Mechanism for low-temperature photoluminescence in GaNAs/GaAs structures grown by molecular-beam epitaxy. *Appl. Phys. Lett.*, 75(4):501 – 503, 1999.
- [27] I. A. Buyanova, W. M. Chen, and C. W. Tu. Magneto-optical and light-emission properties of III-As-N semiconductors. *Semicond. Sci. Tech.*, 17(8):815 – 822, 2002.
- [28] I. A. Buyanova, M. Izadifard, W. M. Chen, A. Polimeni, M. Capizzi, H. P. Xin, and C. W. Tu. Hydrogen-induced improvements in optical quality of GaNAs alloys. *Appl. Phys. Lett.*, 82(21):3662 – 3664, 2003.

- [29] I. A. Buyanova, G. Pozina, P. N. Hai, N. Q. Thinh, J. P. Bergman, W. M. Chen, H. P. Xin, and C. W. Tu. Mechanism for rapid thermal annealing improvements in undoped $\text{GaN}_x\text{As}_{1-x}/\text{GaAs}$ structures grown by molecular beam epitaxy. *Appl. Phys. Lett.*, 77(15):2325, 2000.
- [30] H. C. Casey, B. I. Miller, and E. Pinkas. Variation of minority carrier diffusion length with carrier concentration in GaAs liquid phase epitaxial layers. *J. Appl. Phys.*, 44(3):1281 – 1287, 1973.
- [31] T. Chakraborty and V. M. Apalkov. Quantum cascade transitions in nanostructures. *Adv. Phys.*, 52(5):455 – 521, 2003.
- [32] A. Y. Cho and I. Hayashi. Epitaxy of silicon doped gallium arsenide by molecular beam method. *Metall. Trans.*, 2(3):777 – 780, 1971.
- [33] J. J. Coleman. Chapter 8 - Strained layer quantum well heterostructure lasers. In P. S. Zory, editor, *Quantum well lasers*, pages 367 – 413. Academic Press, San Diego, 1993.
- [34] P. J. Dean, H. Venghaus, and P. E. Simmonds. Conduction-band-to-acceptor magnetoluminescence in zinc telluride. *Phys. Rev. B*, 18:6813 – 6823, 1978.
- [35] O. Drachenko and M. Helm. Chapter 10 - Cyclotron resonance spectroscopy. In A. Patané and N. Balkan, editors, *Semiconductor research*, volume 150, pages 283 – 307. Springer, Berlin Heidelberg, 2012.
- [36] O. Drachenko, D. V. Kozlov, V. Ya. Aleshkin, V. I. Gavrilenko, K. V. Maremyanin, A. V. Ikonnikov, B. N. Zvonkov, M. Goiran, J. Leotin, G. Fasching, S. Winnerl, H. Schneider, J. Wosnitza, and M. Helm. High-field splitting of the cyclotron resonance absorption in strained $p\text{-InGaAs}/\text{GaAs}$ quantum wells. *Phys. Rev. B*, 79:073301, 2009.
- [37] O. Drachenko, H. Schneider, M. Helm, D. Kozlov, V. Gavrilenko, J. Wosnitza, and J. Leotin. Modification to the central-cell correction of germanium acceptors. *Phys. Rev. B*, 84:245207, 2011.
- [38] O. Drachenko, S. Winnerl, H. Schneider, M. Helm, J. Wosnitza, and J. Leotin. Compact magnetospectrometer for pulsed magnets based on infrared quantum cascade lasers. *Rev. Sci. Instrum.*, 82(3):033108, 2011.

-
- [39] G. Dresselhaus, A. F. Kip, and C. Kittel. Observation of cyclotron resonance in germanium crystals. *Phys. Rev.*, 92(3):827, 1953.
- [40] G. Dresselhaus, A. F. Kip, and C. Kittel. Cyclotron resonance of electrons and holes in silicon and germanium crystals. *Phys. Rev.*, 98(2):368 – 384, 1955.
- [41] Harry Rieck Edelstahl. Nahtlose Edelstahlrohre aus dem Werkstoff 1.4571. <http://www.riECK-edelstahl.de/>, May 2016.
- [42] A. L. Éfros. Electron localization in disordered systems (the Anderson transition). *Sov. Phys. Uspekhi*, 21(9):746 – 760, 1978.
- [43] R. J. Elliott, J. A. Krumhansl, and P. L. Leath. The theory and properties of randomly disordered crystals and related physical systems. *Rev. Mod. Phys.*, 46(3):465 – 543, 1974.
- [44] A. Erol, editor. *Dilute III-V nitride semiconductors and material systems*, volume 105 of *Springer Series in Materials Science*. Springer, Berlin Heidelberg, 2008.
- [45] F. Eßer, O. Drachenko, A. Patané, M. Ozerov, S. Winnerl, H. Schneider, and M. Helm. Direct determination of the electron effective mass of GaAsN by terahertz cyclotron resonance spectroscopy. *Appl. Phys. Lett.*, 107(6):062103, 2015.
- [46] S. Fahy, A. Lindsay, H. Ouerdane, and E. P. O’Reilly. Alloy scattering of n -type carriers in $\text{GaN}_x\text{As}_{1-x}$. *Phys. Rev. B*, 74:035203, 2006.
- [47] J. Faist, F. Capasso, D. L. Sivco, C. Sirtori, A. L. Hutchinson, and A. Y. Cho. Quantum cascade laser. *Science*, 264(5158):553 – 556, 1994.
- [48] H. Y. Fan. Valence Semiconductors, Germanium and Silicon. In F. Seitz and D. Turnbull, editors, *Solid state physics*, volume 1, pages 283 – 365. Academic Press, New York, 1955.
- [49] B. Fluegel, K. Alberi, D. A. Beaton, S. A. Crooker, A. J. Ptak, and A. Mascarenhas. Evolution of superclusters and delocalized states in $\text{GaAs}_{1-x}\text{N}_x$. *Phys. Rev. B*, 86(20):205203, 2012.

-
- [50] S. Francoeur, S. A. Nikishin, C. Jin, Y. Qiu, and H. Temkin. Excitons bound to nitrogen clusters in GaAsN. *Appl. Phys. Lett.*, 75(11):1538 – 1540, 1999.
- [51] S. Francoeur, G. Sivaraman, Y. Qiu, S. Nikishin, and H. Temkin. Luminescence of as-grown and thermally annealed GaAsN/GaAs. *Appl. Phys. Lett.*, 72(15):1857 – 1859, 1998.
- [52] J. E. Geusic, H. M. Marcos, and L. G. Van Uitert. Laser oscillations in Nd-doped yttrium aluminum, yttrium gallium and gadolinium garnets. *Appl. Phys. Lett.*, 4(10):182 – 184, 1964.
- [53] C. Gmachl, F. Capasso, D. L. Sivco, and A. Y. Cho. Recent progress in quantum cascade lasers and applications. *Rep. Prog. Phys.*, 64(11):1533 – 1601, 2001.
- [54] S. Gupta, M. Y. Frankel, J. A. Valdmanis, J. F. Whitaker, G. A. Mourou, F. W. Smith, and A. R. Calawa. Subpicosecond carrier lifetime in GaAs grown by molecular beam epitaxy at low temperatures. *Appl. Phys. Lett.*, 59(25):3276 – 3278, 1991.
- [55] P. N. Hai, W. M. Chen, I. A. Buyanova, H. P. Xin, and C. W. Tu. Direct determination of electron effective mass in GaNAs/GaAs quantum wells. *Appl. Phys. Lett.*, 77(12):1843 – 1845, 2000.
- [56] J.S. Harris Jr., H. Yuen, S. Bank, M. Wistey, V. Lordi, T. Gugov, H. Bae, and L. Goddard. Chapter 1 - MBE growth and characterization of long wavelength dilute nitride III-V alloys. In M. Henini, editor, *Dilute nitride semiconductors*, pages 1 – 92. Elsevier, Amsterdam, 2005.
- [57] J. R. Haynes and H. B. Briggs. Radiation produced in germanium and silicon by electron-hole recombination. *P.Am. Phys. Soc.*, 86:647 – 649, 1952.
- [58] M. Henini, editor. *Dilute nitride semiconductors*. Elsevier, Amsterdam, 2005.
- [59] T. Herrmannsdörfer, H. Krug, F. Pobell, S. Zherlitsyn, H. Eschrig, J. Freudenberger, K.H. Müller, and L. Schultz. The high field project at Dresden/Rossendorf: A Pulsed 100 T/10 ms laboratory at an infrared free-electron laser facility. *J. Low Temp. Phys.*, 133(1-2):41 – 59, 2003.

-
- [60] J. J. Hopfield, D. G. Thomas, and R. T. Lynch. Isoelectronic donors and acceptors. *Phys. Rev. Lett.*, 17:312 – 315, 1966.
- [61] J. E. Huffman, A. G. Crouse, B. L. Halleck, T. V. Downes, and T. L. Herter. Si:Sb blocked impurity band detectors for infrared astronomy. *J. Appl. Phys.*, 72(1):273 – 275, 1992.
- [62] C. J. Hwang. Doping dependence of hole lifetime in n-type GaAs. *J. Appl. Phys.*, 42(11):4408 – 4413, 1971.
- [63] J. C. M. Hwang, H. Temkin, T. M. Brennan, and R. E. Frahm. Growth of high-purity GaAs layers by molecular beam epitaxy. *Appl. Phys. Lett.*, 42(1):66 – 68, 1983.
- [64] J. Ibàñez, R. Cuscó, E. Alarcón-Lladó, L. Artús, A. Patanè, D. Fowler, L. Eaves, K. Uesugi, and I. Suemune. Electron effective mass and mobility in heavily doped n-GaAsN probed by Raman scattering. *J. Appl. Phys.*, 103(10):103528, 2008.
- [65] K. Iga and S. Uchiyama. GaInAsP/InP surface-emitting laser diode. *Opt. Quant. Electron.*, 18(6):403 – 422, 1986.
- [66] Princeton Instruments. Acton SpectraPro monochromators and spectrographs. <http://www.princetoninstruments.com/products/spec/actonseries/>, May 2016.
- [67] M. A. Ivanov and Y. G. Pogorelov. Electron properties of two-parameter long-range impurity states. *Sov. Phys. JETP*, 61:1033, 1985.
- [68] N. C. Jarosik, B. D. McCombe, B. V. Shanabrook, J. Comas, John Ralston, and G. Wicks. Binding of shallow donor impurities in quantum-well structures. *Phys. Rev. Lett.*, 54:1283 – 1286, 1985.
- [69] E. D. Jones, N. A. Modine, A. A. Allerman, S. R. Kurtz, A. F. Wright, S. T. Tozer, and X. Wei. Band structure of $\text{In}_x\text{Ga}_{1-x}\text{As}_{1-y}\text{N}_y$ alloys and effects of pressure. *Phys. Rev. B*, 60:4430 – 4433, 1999.

- [70] A. Kaschner, T. Lüttgert, H. Born, A. Hoffmann, A. Yu. Egorov, and H. Riechert. Recombination mechanisms in GaInNAs/GaAs multiple quantum wells. *Appl. Phys. Lett.*, 78(10):1391 – 1393, 2001.
- [71] R. F. Kazarinov and R. A. Suris. Possibility of the amplification of electromagnetic waves in a semiconductor with a superlattice. *Sov. Phys. Semicond.*, 5:707, 1971.
- [72] P. N. Keating. Effect of invariance requirements on the elastic strain energy of crystals with application to the diamond structure. *Phys. Rev.*, 145:637 – 645, 1966.
- [73] U. Keller. Recent developments in compact ultrafast lasers. *Nature*, 424:831 – 838, 2003.
- [74] P. R. C. Kent and A. Zunger. Evolution of III-V nitride alloy electronic structure: The localized to delocalized transition. *Phys. Rev. Lett.*, 86:2613 – 2616, 2001.
- [75] P. R. C. Kent and A. Zunger. Theory of electronic structure evolution in GaAsN and GaPN alloys. *Phys. Rev. B*, 64:115208, 2001.
- [76] K.-J. Kim and A. Sessler. Free-electron lasers: present status and future prospects. *Science*, 250(4977):88 – 93, 1990.
- [77] P. J. Klar, H. Grüning, W. Heimbrodt, J. Koch, F. Höhnsdorf, W. Stolz, P. M. A. Vicente, and J. Camassel. From N isoelectronic impurities to N-induced bands in the GaN_xAs_{1-x} alloy. *Appl. Phys. Lett.*, 76(23):3439 – 3441, 2000.
- [78] F. K. Kneubühl and M. W. Sigrist. *Laser*. Vieweg+Teubner, Wiesbaden, 7. edition, 2008.
- [79] A. N. Kocharyan. Changes in the valence of rare-earth semiconductors in the many-impurity Anderson model. *Sov. Phys. Solid State*, 28:6 – 10, 1986.
- [80] R. Köhler, A. Tredicucci, F. Beltram, H. E. Beere, E. H. Linfield, A. G. Davies, D. A. Ritchie, R. C. Iotti, and F. Rossi. Terahertz semiconductor-heterostructure laser. *Nature*, 417(6885):156 – 159, 2002.

- [81] M. Kondow, K. Uomi, A. Niwa, Kitatani T., S. Watahiki, and Y. Yazawa. GaInNAs: A novel material for long-wavelength-range laser diodes with excellent high-temperature performance. *Jpn. J. of Appl. Phys.*, 35(2S):1273 – 1275, 1996.
- [82] R. Kudrawiec, M. Latkowska, M. Baranowski, J. Misiewicz, L. H. Li, and J. C. Harmand. Photorefectance, photoluminescence, and microphotoluminescence study of optical transitions between delocalized and localized states in GaN_{0.02}As_{0.98}, Ga_{0.95}In_{0.05}N_{0.02}As_{0.98}, and GaN_{0.02}As_{0.90}Sb_{0.08} layers. *Phys. Rev. B*, 88(12):125201, 2013.
- [83] R. Kudrawiec, M. Motyka, M. Gladysiewicz, J. Misiewicz, J.A. Gupta, and G.C. Aers. Contactless electroreflectance of GaN_yAs_{1-y}/GaAs multi quantum wells: The conduction band offset and electron effective mass issues. *Solid State Commun.*, 138(77):365 – 370, 2006.
- [84] R. Kudrawiec, G. Sęk, J. Misiewicz, F. Ishikawa, A. Trampert, and K. H. Ploog. Localized and delocalized states in GaNAs studied by microphotoluminescence and photorefectance. *Appl. Phys. Lett.*, 94(1):011907, 2009.
- [85] S. R. Kurtz, A. A. Allerman, C. H. Seager, R. M. Sieg, and E. D. Jones. Minority carrier diffusion, defects, and localization in InGaAsN, with 2% nitrogen. *Appl. Phys. Lett.*, 77(3):400 – 402, 2000.
- [86] W. D. Laidig, P. J. Caldwell, Y. F. Lin, and C. K. Peng. Strained-layer quantum-well injection laser. *Appl. Phys. Lett.*, 44(7):653 – 655, 1984.
- [87] R. M. Lammert, P. V. Mena, D. V. Forbes, M. L. Osowski, S. M. Kang, and J. J. Coleman. Strained-layer InGaAs-GaAs-AlGaAs lasers with monolithically integrated photodiodes by selective-area MOCVD. *Photonics Techn. Lett., IEEE*, 7(3):247 – 250, 1995.
- [88] Landölt-Börnstein. *Numerical data and functional relationships in science and technology, group III*, volume 17. Springer, Berlin, 1982.
- [89] M. Latkowska, R. Kudrawiec, G. Sęk, J. Misiewicz, J. Ibàñez, M. Henini, and M. Hopkinson. Thermal quenching of single localized excitons in GaInNAs layers. *Appl. Phys. Lett.*, 98(13):1 – 4, 2011.

- [90] J. P. Laurenti, P. Roentgen, K. Wolter, K. Seibert, H. Kurz, and J. Camassel. Indium-doped GaAs: A very dilute alloy system. *Phys. Rev. B*, 37(8):4155 – 4163, 1988.
- [91] B. Lax, H. J. Zeiger, R. N. Dexter, and E. S. Rosenblum. Directional properties of the cyclotron resonance in germanium. *Phys. Rev.*, 93:1418 – 1420, 1954.
- [92] A. Lindsay and E. P. O’Reilly. Theory of enhanced bandgap non-parabolicity in $\text{GaN}_x\text{As}_{1-x}$ and related alloys. *Solid State Commun.*, 112(8):443 – 447, 1999.
- [93] A. Lindsay and E. P. O’Reilly. Influence of nitrogen resonant states on the electronic structure of $\text{GaN}_x\text{As}_{1-x}$. *Solid State Commun.*, 118(6):313 – 317, 2001.
- [94] A. Lindsay and E. P. O’Reilly. Unification of the band anticrossing and cluster-state models of dilute nitride semiconductor alloys. *Phys. Rev. Lett.*, 93(19):196402, 2004.
- [95] X. Liu, M. E. Pistol, and L. Samuelson. Excitons bound to nitrogen pairs in GaAs. *Phys. Rev. B*, 42(12):7504 – 7512, 1990.
- [96] D. A. Livshits, A. Yu. Egorov, and H. Riechert. 8 W continuous wave operation of InGaAsN lasers at 1.3 μm . *Electron. Lett.*, 36(16):1381 – 1382, 2000.
- [97] G. B. Lush, H. F. MacMillan, B. M. Keyes, D. H. Levi, M. R. Melloch, R. K. Ahrenkiel, and M. S. Lundstrom. A study of minority carrier lifetime versus doping concentration in n-type GaAs grown by metalorganic chemical vapor deposition. *J. Appl. Phys.*, 72(4):1436 – 1442, 1992.
- [98] R. A. Mair, J. Y. Lin, H. X. Jiang, E. D. Jones, A. A. Allerman, and S. R. Kurtz. Time-resolved photoluminescence studies of $\text{In}_x\text{Ga}_{1-x}\text{As}_{1-y}\text{N}_y$. *Appl. Phys. Lett.*, 76(2):188 – 190, 2000.
- [99] T. Makimoto, H. Saito, T. Nishida, and N. Kobayashi. Excitonic luminescence and absorption in dilute $\text{GaAs}_{1-x}\text{N}_x$ alloy ($x < 0.3\%$). *Appl. Phys. Lett.*, 70(22):2984 – 2986, 1997.
- [100] R. M. Martin. Elastic properties of ZnS structure semiconductors. *Phys. Rev. B*, 1(10):4005 – 4011, 1970.

-
- [101] F. Masia, G. Pettinari, A. Polimeni, M. Felici, A. Miriametro, M. Capizzi, A. Lindsay, S. B. Healy, E. P. O'Reilly, A. Cristofoli, G. Bais, M. Piccin, S. Rubini, F. Martelli, A. Franciosi, P. J. Klar, K. Volz, and W. Stolz. Interaction between conduction band edge and nitrogen states probed by carrier effective-mass measurements in $\text{GaAs}_x\text{N}_{1-x}$. *Phys. Rev. B*, 73:073201, 2006.
- [102] F. Masia, A. Polimeni, G. B. H. Von Högersthal, M. Bissiri, M. Capizzi, P. J. Klar, and W. Stolz. Early manifestation of localization effects in diluted $\text{Ga}(\text{AsN})$. *Appl. Phys. Lett.*, 82(2003):4474 – 4476, 2003.
- [103] K. Matsuda, T. Saiki, M. Takahashi, A. Moto, and S. Takagishi. Near-field photoluminescence study of GaNAs alloy epilayer at room and cryogenic temperature. *Appl. Phys. Lett.*, 78(11):1508 – 1510, 2001.
- [104] J. W. Matthews and A. E. Blakeslee. Defects in epitaxial multilayers: I. Misfit dislocations. *J. Cryst. Growth*, 27:118 – 125, 1974.
- [105] T. Mattila, S.-H. Wei, and A. Zunger. Localization and anticrossing of electron levels in $\text{GaAs}_{1-x}\text{N}_x$ alloys. *Phys. Rev. B*, 60:R11245 – R11248, 1999.
- [106] B. D. McCombe, R. Kaplan, R. J. Wagner, E. Gornik, and W. Müller. Absorption and emission studies of the quantum-limit cyclotron resonance linewidth in $n - \text{InSb}$. *Phys. Rev. B*, 13:2536 – 2539, 1976.
- [107] J. C. Mikkelsen and J. B. Boyce. Extended x-ray-absorption fine-structure study of $\text{Ga}_{1-x}\text{In}_x\text{As}$ random solid solutions. *Phys. Rev. B*, 28(12):7130 – 7140, 1983.
- [108] A. Mintairov, T. Kosel, J. Merz, P. Blagnov, A. Vlasov, V. Ustinov, and R. Cook. Near-Field Magnetophotoluminescence Spectroscopy of Composition Fluctuations in InGaAsN . *Phys. Rev. Lett.*, 87(27):277401, 2001.
- [109] N. Miura. *Physics of semiconductors in high magnetic fields*, volume 15 of *Series on semiconductor science and technology*. Oxford University Press, Oxford, 2007.
- [110] R. Mouillet, L.-A. de Vaulchier, E. Deleporte, Y. Guldner, L. Travers, and J.-C. Harmand. Role of nitrogen in the mobility drop of electrons in modulation-doped $\text{GaAsN}/\text{AlGaAs}$ heterostructures. *Solid State Comm.*, 126(6):333 – 337, 2003.

-
- [111] J. H. Neave, P. J. Dobson, J. J. Harris, P. Dawson, and B. A. Joyce. Silicon doping of MBE-grown GaAs films. *Appl. Phys. A*, 32(4):195 – 200, 1983.
- [112] A. Neumann, A. Patanè, L. Eaves, A.E. Belyaev, D. Gollub, A. Forchel, and M. Kamp. Magneto-tunnelling spectroscopy of nitrogen clusters in Ga(AsN) alloys. *Optoelectronics, IEE Proceedings*, 150(1):49 – 51, 2003.
- [113] L. Nordheim. Zur Elektronentheorie der Metalle. I. *Annalen der Physik*, 401(5):607 – 640, 1931.
- [114] E. P. O’Reilly, A. Lindsay, and S. Fahy. Theory of the electronic structure of dilute nitride alloys: beyond the band-anti-crossing model. *J. Phys. Condens. Mat.*, 16(31):S3257 – S3276, 2004.
- [115] E. P. O’Reilly, A. Lindsay, S. Tomić, and M. Kamal-Saadi. Tight-binding and $k \cdot p$ models for the electronic structure of Ga(In)NAs and related alloys. *Semicond. Sci. Tech.*, 17(8):870 – 879, 2002.
- [116] P. G. O’Shea. Free-electron lasers: status and applications. *Science*, 292(5523):1853 – 1858, 2001.
- [117] M. Oueslati, C. Benoit, and M. Zouaghi. Resonant Raman scattering on localized states due to disorder in GaAs_{1-x}P_x alloys. *Phys. Rev. B*, 37(6):3037 – 3041, 1988.
- [118] M. Ozerov, J. Romhányi, M. Belesi, H. Berger, J.-Ph. Ansermet, J. van den Brink, J. Wosnitza, S. A. Zvyagin, and I. Rousochatzakis. Establishing the fundamental magnetic interactions in the Chiral Skyrmionic Mott insulator Cu₂OSeO₃ by terahertz electron spin resonance. *Phys. Rev. Lett.*, 113:157205, 2014.
- [119] A. Patanè, G. Allison, L. Eaves, N. V. Kozlova, Q. D. Zhuang, A. Krier, M. Hopkinson, and G. Hill. Electron coherence length and mobility in highly mismatched III-N-V alloys. *Appl. Phys. Lett.*, 93(25):252106, 2008.
- [120] A. Patanè and L. Eaves. Chapter 8 - Probing the “unusual” band structure of dilute Ga(AsN) quantum wells by magneto-tunnelling spectroscopy and other

- techniques. In M. Henini, editor, *Dilute nitride semiconductors*, pages 253 – 277. Elsevier, Amsterdam, 2005.
- [121] I. Pelant and J. Valenta. *Luminescence Spectroscopy of Semiconductors*. Oxford University Press, 2012.
- [122] P. Perlin, S. G. Subramanya, D. E. Mars, J. Kruger, N. A. Shapiro, H. Siegle, and E. R. Weber. Pressure and temperature dependence of the absorption edge of a thick $\text{Ga}_{0.92}\text{In}_{0.08}\text{As}_{0.985}\text{N}_{0.015}$ layer. *Appl. Phys. Lett.*, 73(25):3703 – 3705, 1998.
- [123] G. Pettinari, A. Polimeni, J. H. Blokland, R. Trotta, P. C. M. Christianen, M. Capizzi, J. C. Maan, X. Lu, E. C. Young, and T. Tiedje. Compositional dependence of the exciton reduced mass in $\text{GaAs}_{1-x}\text{Bi}_x$ ($x = 0 - 10\%$). *Phys. Rev. B*, 81:235211, 2010.
- [124] G. Pettinari, A. Polimeni, and M. Capizzi. Chapter 5 - Photoluminescence: a tool for investigating optical, electronic, and structural properties of semiconductors. In A. Patanè and N. Balkan, editors, *Semiconductor research*, volume 150, pages 125 – 170. Springer, Berlin Heidelberg, 2012.
- [125] G. Pettinari, A. Polimeni, F. Masia, R. Trotta, M. Felici, M. Capizzi, T. Niebling, W. Stolz, and P. J. Klar. Electron mass in dilute nitrides and its anomalous dependence on hydrostatic pressure. *Phys. Rev. Lett.*, 98(14):4 – 7, 2007.
- [126] K. Ploog, A. Fischer, and H. Künzel. The use of Si and Be impurities for novel periodic doping structures in GaAs grown by molecular beam epitaxy. *J. Electrochem. Soc.*, 128:400 – 410, 1981.
- [127] A. Polimeni, G. Baldassarri Höger von Högersthal, F. Masia, A. Frova, M. Capizzi, S. Sanna, V. Fiorentini, P. J. Klar, and W. Stolz. Tunable variation of the electron effective mass and exciton radius in hydrogenated $\text{GaAs}_{1-x}\text{N}_x$. *Phys. Rev. B*, 69(4):1 – 4, 2004.
- [128] A. Polimeni, M. Capizzi, M. Geddo, M. Fischer, M. Reinhardt, and A. Forchel. Effect of temperature on the optical properties of $(\text{InGa})(\text{AsN})/\text{GaAs}$ single quantum wells. *Appl. Phys. Lett.*, 77(18):2870 – 2872, 2000.

- [129] A. Polimeni, F. Masia, G. Baldassarri Höger von Högersthal, and M. Capizzi. Chapter 7 - Measurement of carrier localization degree, electron effective mass, and excitation size in $\text{In}_x\text{Ga}_{1-x}\text{As}_{1-y}\text{N}_y$ alloys. In M. Henini, editor, *Dilute nitride semiconductors*, pages 223 – 251. Elsevier, Amsterdam, 2005.
- [130] A. Polimeni, G. Pettinari, R. Trotta, F. Masia, M. Felici, M. Capizzi, a. Lindsay, E. P. O'Reilly, T. Niebling, W. Stolz, P. J. Klar, F. Martelli, and S. Rubini. Photoluminescence under magnetic field and hydrostatic pressure for probing the electronic properties of GaAsN. *Phys. Status Solidi A*, 205(1):107 – 113, 2008.
- [131] P. Rauter, T. Fromherz, S. Winnerl, M. Zier, A. Kolitsch, M. Helm, and G. Bauer. Terahertz Si:B blocked-impurity-band detectors defined by nonepitaxial methods. *Appl. Phys. Lett.*, 93(26):261104, 2008.
- [132] H. Riechert, A. Ramakrishnan, and G. Steinle. Development of InGaAsN-based 1.3 μm VCSELs. *Semicond. Sci. Tech.*, 17(8):892 – 897, 2002.
- [133] J. A. Rossi, C. M. Wolfe, and J. O. Dimmock. Acceptor luminescence in high-purity n -type GaAs. *Phys. Rev. Lett.*, 25(23):1614 – 1617, 1970.
- [134] W. Rühle and E. Göbel. New aspects of the magnetoluminescence of a band to acceptor transition in GaAs. *Phys. Status Solidi B*, 78(311):311 – 317, 1976.
- [135] H. Saito, T. Makimoto, and N. Kobayashi. Photoluminescence characteristics of nitrogen atomic-layer-doped GaAs grown by MOVPE. *J. Cryst. Growth*, 170(1-4):372 – 376, 1997.
- [136] W. Shan, W. Walukiewicz, J. W. Ager, E. E. Haller, J. F. Geisz, D. J. Friedman, J. M. Olson, and S. R. Kurtz. Band anticrossing in GaInNAs alloys. *Phys. Rev. Lett.*, 82:1221 – 1224, 1999.
- [137] W. Shan, W. Walukiewicz, J. W. Ager, E. E. Haller, J. F. Geisz, D. J. Friedman, J. M. Olson, and S. R. Kurtz. Effect of nitrogen on the band structure of GaInNAs alloys. *J. Appl. Phys.*, 86(4):2349 – 2351, 1999.
- [138] W. Shan, W. Walukiewicz, K. M. Yu, J. W. III Ager, E. E. Haller, J. F. Geisz, D. J. Friedman, J. M. Olson, S. R. Kurtz, and C. Nauka. Effect of nitrogen on

- the electronic band structure of group III-N-V alloys. *Phys. Rev. B*, 62(7):4211 – 4214, 2000.
- [139] T. Shima, Y. Makita, S. Kimura, T. Iida, H. Sanpei, M. Yamaguchi, K. Kudo, K. Tanaka, N. Kobayashi, A. Sandhu, and Y. Hoshino. Optical characterization of low-energy nitrogen-ion doped GaAs. *Nucl. Instrum. Meth. B*, 127-128:437 – 441, 1997.
- [140] T. Shimano, T. Murotani, M. Nakatani, M. Otsubo, and S. Mitsui. High quality Si-doped GaAs layers grown by molecular beam epitaxy. *Surf. Sci.*, 86:126 – 136, 1979.
- [141] N. Shtinkov, P. Desjardins, and R. A. Masut. Empirical tight-binding model for the electronic structure of dilute GaNAs alloys. *Phys. Rev. B*, 67:081202, 2003.
- [142] C. Skierbiszewski, I. Gorczyca, S.P. Lepkowski, J. Lusakowski, J. Borysiuk, and J. Toivonen. The electron effective mass at the bottom of the GaNAs conduction band. *Semicond. Sci. Technol.*, 19:1189 – 1195, 2004.
- [143] D. Smirnov, C. Becker, O. Drachenko, V. Rylkov, H. Page, J. Leotin, and C. Sirtori. Control of electron-optical-phonon scattering rates in quantum box cascade lasers. *Phys. Rev. B*, 66(12):121305(R), 2002.
- [144] D. Smirnov, O. Drachenko, J. Leotin, H. Page, C. Becker, C. Sirtori, V. Apalkov, and T. Chakraborty. Intersubband magnetophonon resonances in quantum cascade structures. *Phys. Rev. B*, 66(12):125317, 2002.
- [145] Spectra-Physics. Millennia: high power cw DPSS lasers. <http://www.spectra-physics.com/products/cw-lasers/millennia-ev#overview>, May 2016.
- [146] Spectra-Physics. Tsunami: flexible, high performance ultrafast TiSa oscillators. <http://www.spectra-physics.com/products/ultrafast-lasers/tsunami?cat=scientific&subcat=oscillators#overview>, May 2016.
- [147] W. G. Spitzer and H. Y. Fan. Determination of optical constants and carrier effective mass of semiconductors. *Phys. Rev.*, 106:882 – 890, 1957.

- [148] G. Steinle, F. Mederer, M. Kicherer, R. Michalzik, G. Kristen, A.Y. Egorov, H. Riechert, H.D. Wolf, and K. J. Ebeling. Data transmission up to 10 Gbit/s with 1.3 μm wavelength InGaAsN VCSELs. *Electron. Lett.*, 37(10):632 – 634, 2001.
- [149] G. E. Stillman, C. M. Wolfe, and J. O. Dimmock. Hall coefficient factor for polar mode scattering in n-type GaAs. *J. Phys. Chem. Solids*, 31(6):1199 – 1204, 1970.
- [150] H. Temkin and J. C. M. Hwang. Undoped, semi-insulating GaAs layers grown by molecular beam epitaxy. *Appl. Phys. Lett.*, 42(2):178 – 180, 1983.
- [151] J. Teubert, P. J. Klar, W. Heimbrod, K. Volz, W. Stolz, P. Thomas, G. Leibiger, and V. Gottschalch. Enhanced weak Anderson localization phenomena in the magnetoresistance of n-type (Ga,In)(N,As). *Appl. Phys. Lett.*, 84(5):747 – 749, 2004.
- [152] J. J. Tietjen and L. R. Weisberg. Electron mobility in $\text{GaAs}_{1-x}\text{P}_x$ alloys. *Appl. Phys. Lett.*, 7(10):261 – 263, 1965.
- [153] K. Utaka, S. Akiba, K. Sakai, and Y. Matsushima. Room-temperature CW operation of distributed-feedback buried-heterostructure InGaAsP/InP lasers emitting at 1.57 μm . *Electron. Lett.*, 17(25-26):961 – 963, 1981.
- [154] Y.P. Varshni. Temperature dependence of the energy gap in semiconductors. *Physica*, 34(1):149 – 154, 1967.
- [155] M. P. Vaughan and B. K. Ridley. Electron-nitrogen scattering in dilute nitrides. *Phys. Rev. B*, 75:195205, 2007.
- [156] A. Wade, G. Fedorov, D. Smirnov, S. Kumar, B. S. Williams, Q. Hu, and J. L. Reno. Magnetic-field-assisted terahertz quantum cascade laser operating up to 225 K. *Nat. Photonics*, 3(1):41 – 45, 2009.
- [157] W. Walukiewicz, W. Shan, J. W. Ager, D. R. Chamberlin, E. E. Haller, J. F. Geisz, D. J. Friedman, J. M. Olson, and S. R. Kurtz. Nitrogen-induced modification of the electronic structure of group III-N-V alloys. In *ECS Proc.*, volume 99 - 11, page 190, 1999.

-
- [158] W. Walukiewicz, W. Shan, K. M. Yu, J. W. Ager, E. E. Haller, I. Miotkowski, M. J. Seong, H. Alawadhi, and A. K. Ramdas. Interaction of localized electronic states with the conduction band: band anticrossing in II-VI semiconductor ternaries. *Phys. Rev. Lett.*, 85(7):1552 – 1555, 2000.
- [159] L.-W. Wang, L. Bellaiche, S.-H. Wei, and A. Zunger. “Majority Representation” of alloy electronic states. *Phys. Rev. Lett.*, 80(21):4725 – 4728, 1998.
- [160] Lin-Wang Wang. Large-scale local-density-approximation band gap-corrected GaAsN calculations. *Appl. Phys. Lett.*, 78(11):1565 – 1567, 2001.
- [161] Y. J. Wang, X. Wei, Y. Zhang, A. Mascarenhas, H. P. Xin, Y. G. Hong, and C. W. Tu. Evolution of the electron localization in a nonconventional alloy system GaAs_{1-x}N_x probed by high-magnetic-field photoluminescence. *Appl. Phys. Lett.*, 82(2003):4453 – 4455, 2003.
- [162] M. Weyers, M. Sato, and H. Ando. Red shift of photoluminescence and absorption in dilute GaAsN alloy layers. *Jpn. J. Appl. Phys.*, 31(Part 2, No. 7A):L853 – L855, 1992.
- [163] B. S. Williams. Terahertz quantum-cascade lasers. *Nat. Photonics*, 1(9):517 – 525, 2007.
- [164] D. J. Wolford, J. A. Bradley, K. Fry, and J. Thompson. The nitrogen isoelectronic trap in GaAs. In *Proceedings of the 17th International Conference on the Physics of Semiconductors*, pages 627 – 630. Springer New York, New York, NY, 1984.
- [165] J. Wu, W. Shan, W. Walukiewicz, K. M. Yu, J. W. III Ager, E. E. Haller, H. P. Xin, and C. W. Tu. Effect of band anticrossing on the optical transitions in GaAs_{1-x}N_x/GaAs multiple quantum wells. *Phys. Rev. B*, 64(8):1 – 4, 2001.
- [166] J. Wu, W. Walukiewicz, and E. Haller. Band structure of highly mismatched semiconductor alloys: Coherent potential approximation. *Phys. Rev. B*, 65(23):233210, 2002.
- [167] L. Yang, M. C. Wu, K. Tai, T. Tanbun-Ek, and R. A. Logan. InGaAsP(1.3 μm)/InP vertical-cavity surface-emitting laser grown by metalorganic vapor phase epitaxy. *Appl. Phys. Lett.*, 56(10):889 – 891, 1990.

-
- [168] F. Yonezawa and K. Morigaki. Coherent potential approximation. *Prog. Theor. Phys. Supp.*, 53:1 – 76, 1973.
- [169] D. L. Young, J. F. Geisz, and T. J. Coutts. Nitrogen-induced decrease of the electron effective mass in $\text{GaAs}_{1-x}\text{N}_x$ thin films measured by thermomagnetic transport phenomena. *Appl. Phys. Lett.*, 82(8):1236 – 1238, 2003.
- [170] W. Zawadzki. Electron transport phenomena in small-gap semiconductors. *Adv. Phys.*, 23(3):435 – 522, 1974.
- [171] W. Zawadzki, P. Pfeffer, S. P. Najda, H. Yokoi, S. Takeyama, and N. Miura. Experimental and theoretical study of magnetodons in GaAs and InP at megagauss fields. *Phys. Rev. B*, 49:1705 – 1710, 1994.
- [172] S. Zemon, P. Norris, E. S. Koteles, and G. Lambert. Studies of free-to-bound acceptor photoluminescence in an applied magnetic field for undoped GaAs grown by metalorganic vapor-phase epitaxy and molecular-beam epitaxy. *J. Appl. Phys.*, 59(8):2828 – 2832, 1986.
- [173] S. Zherlitsyn, T. Herrmannsdörfer, Y. Skourski, A. Sytcheva, and J. Wosnitza. Design of non-destructive pulsed magnets at the HLD. *J. Low Temp. Phys.*, 146(5-6):719 – 732, 2007.
- [174] S. A. Zvyagin, M. Ozerov, E. Čížmár, D. Kamenskyi, S. Zherlitsyn, T. Herrmannsdörfer, J. Wosnitza, R. Wünsch, and W. Seidel. Terahertz-range free-electron laser electron spin resonance spectroscopy: Techniques and applications in high magnetic fields. *Rev. Sci. Instrum.*, 80(7):073102, 2009.

List of Figures

2.1. Relationship between band gap energy and lattice parameter	6
2.2. Simplified crystal structure and energy dispersion of InGaAs	7
2.3. Simplified crystal structure and energy dispersion of GaAsN	8
2.4. BAC model of the conduction bands of GaAsN	9
2.5. BAC electron effective mass of GaAsN	14
2.6. Nitrogen localization for cluster states and perturbed host states of GaAsN	16
2.7. Distribution of N cluster state energies in the LCINS model	20
2.8. LCINS and BAC electron effective masses	21
3.1. Methods for high magnetic field generation	26
3.2. Driving circuit for HLD pulsed magnets with field profiles	27
3.3. Schematic view of a free-electron laser	29
3.4. Operating principle of a quantum cascade laser	31
3.5. Compact magnetospectrometer based on infrared QCLs and THz-range ESR spectrometer	33
3.6. Comparison of CR transmission spectroscopy results using different experimental setups	35
3.7. Time resolved PL spectroscopy setup	36
3.8. Operating principle of a Titanium-Sapphire laser	37
3.9. Operating principle of a Nd:YAG laser	38
3.10. Part one of the experimental setup for magneto-PL at the HLD	40
3.11. Probe for magneto-PL measurements in pulsed magnetic fields at the HLD	41
3.12. Part two of the experimental setup for magneto-PL at the HLD	42
3.13. Temporal profile of the magnetic field and the trigger signals of the laser and spectrometer for magneto-PL measurements at the HLD	43

4.1. Overview of different indirect experimental and theoretical results of the electron effective mass m^* in $\text{GaAs}_{1-x}\text{N}_x$	46
4.2. Difference between cyclotron resonance and impurity-shifted cyclotron resonance and the influence of mechanical artifacts	48
4.3. Transmission spectra with a FEL photon energy of 41.4 ± 0.5 meV	50
4.4. FTIR spectroscopy reflection spectra of GaAsN with different N content	51
4.5. CR transmission spectra of $\text{GaAs}_{1-x}\text{N}_x$ with a QCL photon energy of 17.7 ± 0.5 meV and a FEL photon energy of 26.7 ± 0.5 meV	52
4.6. Energy dependence of the electron effective mass of $\text{GaAs}_{1-x}\text{N}_x$	54
4.7. Mobility decrease of GaAsN with increasing N content	56
4.8. Effective mass results compared with theory and former indirect experiments	57
5.1. Overview of luminescence processes in crystalline semiconductors	60
5.2. Low-temperature PL of GaAs:Si	62
5.3. Low-temperature PL of (a) the Si-doped and (b) undoped GaAsN sample series	63
5.4. Temperature series of intrinsic $\text{GaAs}_{1-x}\text{N}_x$ with $x = 0.095\%$	65
5.5. Power dependence of the 1.48 eV peak in intrinsic $\text{GaAs}_{1-x}\text{N}_x$ with $x = 0.095\%$ (K105) at 50 K	66
5.6. Schematic representation of localized excitonic states and recombination processes of GaAsN	67
5.7. Power series of intrinsic $\text{GaAs}_{1-x}\text{N}_x$ with 0.095% and 0.21% at 4.5 K	70
5.8. Temperature series of intrinsic $\text{GaAs}_{1-x}\text{N}_x$ with $x = 0.21\%$	71
5.9. Temperature series of Si-doped $\text{GaAs}_{1-x}\text{N}_x$ with $x = 0.1\%$ compared to intrinsic $\text{GaAs}_{1-x}\text{N}_x$ with $x = 0.095\%$	74
5.10. Temperature series of Si-doped $\text{GaAs}_{1-x}\text{N}_x$ with $x = 0.2\%$ compared to intrinsic $\text{GaAs}_{1-x}\text{N}_x$ with $x = 0.21\%$	76
5.11. Streak camera images of Si-doped GaAsN samples with an average power density of 9.5 W/cm^2 at 10 K	78
5.12. Streak camera images of the Si-doped $\text{GaAs}_{1-x}\text{N}_x$ with $x = 0.1\%$ at different temperatures	79
5.13. Temperature dependence of the PL decay time dispersion in Si-doped $\text{GaAs}_{1-x}\text{N}_x$ with $x = 0.1\%$	80

5.14. Energy dispersion of the decay time in Si-doped GaAsN	83
6.1. Magneto-PL study of undoped GaAs _{1-x} N _x at 20 – 30 K	89
6.2. Magneto-PL study of intrinsic GaAs _{1-x} N _x at 50 K	91
6.3. Temperature dependence of the magneto-PL in GaAs _{1-x} N _x :Si with $x = 0.2\%$	93
6.4. Magneto-PL study of Si-doped GaAs _{1-x} N _x at 50 K	95
6.5. Field-induced shift of the FE/EHP transition of GaAs _{1-x} N _x with $x = 0\%0.21\%$	99

List of Tables

4.1. Fit results for CR electron effective masses m^* , relaxation times τ and mobilities μ	53
5.1. Fit results for the decay time dispersion with Eq. (5.2)	82
6.1. Fit results for the reduced mass using Eq. (6.7)	100
A.1. Overview of the investigated samples	107
A.2. Overview of important experimental parameters for certain capacitor modules of the HLD	108

Publications

Journals

- F. Eßer, S. Winnerl, A. Patanè, M. Helm, and H. Schneider. Excitonic mobility edge and ultra-short photoluminescence decay time in n-type GaAsN. *Appl. Phys. Lett.*, (under review).
- F. Eßer, O. Drachenko, A. Patanè, M. Ozerov, S. Winnerl, H. Schneider, and M. Helm. Direct determination of the electron effective mass of GaAsN by terahertz cyclotron resonance spectroscopy. *Appl. Phys. Lett.*, 107(6):062103, 2015.
- S. Zybell, J. Bhattacharyya, S. Winnerl, F. Eßer, M. Helm, H. Schneider, L. Schneebeili, C. N. Böttge, M. Kira, S. W. Koch, A. Andrews, and G. Strasser. Characterizing intra-exciton Coulomb scattering in terahertz excitations. *Appl. Phys. Lett.*, 105(20):201109, 2014.
- J. Bhattacharyya, S. Zybell, F. Eßer, M. Helm, H. Schneider, L. Schneebeili, C. N. Böttge, B. Breddermann, M. Kira, S. W. Koch, A. Andrews, and G. Strasser. Magnetic control of Coulomb scattering and terahertz transitions among excitons. *Phys. Rev. B.*, 89(12): 125313, 2014.
- V. Lechner, L. E. Golub, F. Lomakina, V. V. Bel'kov, P. Olbrich, S. Stachel, I. Caspers, M. Griesbeck, M. Kugler, M. J. Hirmer, T. Korn, C. Schüller, D. Schuh, W. Wegscheider, and S. D. Ganichev. Spin and orbital mechanisms of the magnetogyrotropic photogalvanic effects in GaAs/Al_xGa_{1-x}As quantum well structures. *Phys. Rev. B.*, 83(15): 155313, 2011.

Conferences: Oral presentations

- F. Eßer, H. Schneider, S. Winnerl, O. Drachenko, A. Patanè, and M. Helm. Mass of GaAsN in Pulsed Magnetic Fields up to 60 T with Free-Electron Laser IR Radiation. *RHMF 2015; International Conference on Research in High Magnetic Fields 2015*, April 01 - 04, 2015, Grenoble, France.
- F. Eßer, H. Schneider, S. Winnerl, O. Drachenko, A. Patanè, G. Pettinari, and M. Helm. Cyclotron Resonance Spectroscopy of GaAsN in Pulsed Magnetic Fields up to 60 T with Free-Electron Laser IR Radiation. *EDiSON'19: 19th International Conference on Electron Dynamics in Semiconductors, Optoelectronics and Nanostructures*, June 29 - July 02, 2015, Salamanca, Spain.
- F. Eßer, H. Schneider, S. Winnerl, O. Drachenko, A. Patanè, and M. Helm. Pulsed magnetic field spectroscopy up to 70 T on the dilute nitride GaAsN. *DPG-Frühjahrstagung der Sektion Kondensierte Materie*, March 15 - 20, 2015, Berlin, Germany.
- F. Eßer, O. Drachenko, H. Schneider, A. Patanè, M. Hopkinson, and M. Helm. Spectroscopic investigation in high magnetic fields of the dilute nitride GaAsN. *ICPS 2014; International conference on the physics of semiconductors*, August 10 - 15, 2014, Austin, TX, USA.
- F. Eßer, O. Drachenko, H. Schneider, A. Patanè, M. Hopkinson, and M. Helm. Investigation of the effective mass in GaAsN, *DPG-Frühjahrstagung der Sektion Kondensierte Materie*, March 30 - April 04, 2014, Dresden, Germany.

Conferences: Posters

- F. Eßer, H. Schneider, S. Winnerl, O. Drachenko, A. Patanè, and M. Helm. THz free-electron laser investigation of GaAsN in pulsed magnetic fields up to 60 T, *German THz Conference*, June 08 - 10, 2015, Dresden, Germany.
- F. Eßer, O. Drachenko, H. Schneider, A. Patanè, M. Hopkinson, and M. Helm. Optical investigations of GaAsN in high magnetic fields. *Workshop on Optical Properties of Individual Nanowires and Quantum Dots in High Magnetic Field*, September 24 - 26, Toulouse, France.

- F. Lomakina, O. Drachenko, H. Schneider, A. Patanè, M. Hopkinson, and M. Helm. Investigation of the effective mass in GaAsN. *20th International Conference on Electronic Properties of Two-Dimensional Systems (EP2DS-20) and 16th International Conference on Modulated Semiconductor Structures (MSS-16)*, July 01 - 05, 2013, Wroclaw, Poland.
- F. Lomakina, O. Drachenko, H. Schneider, A. Patanè, M. Hopkinson, and M. Helm. Investigation of the effective mass in dilute nitride semiconductors. *DPG-Frühjahrstagung der Sektion Kondensierte Materie*, March 10 - 15, 2013, Regensburg, Germany.

Acknowledgments

I would like to thank various people for their support over the last four years. The work was carried out at the Helmholtz-Zentrum Dresden-Rossendorf in the spectroscopy division. I express my deep gratitude to my thesis supervisor Manfred Helm for giving me the opportunity to prepare this dissertation and for his guidance, encouragement and valuable feedback. Many thanks go to my group leader Harald Schneider for creating a pleasant and creative working environment, for fruitful discussions and his support. I am also very grateful to my colleague, mentor and friend Stephan Winnerl. His continuous encouragement, enthusiasm and support are inspiring.

My grateful thanks are extended to our collaborator Amalia Patanè from the University of Nottingham. I have been amazingly fortunate to benefit from her expertise, enthusiasm and support. Special thanks also go to our collaborators Giorgio Pettinari from the Italian National Research Council, Rome and Antonio Polimeni from the Sapienza University of Rome for stimulating discussions and valuable advice. I am also thankful to Mark Hopkinson and his team from the University of Sheffield and Wolfgang Stolz and coworkers from the Philipps-Universität Marburg for growing our samples.

I am thankful to all of my past and present colleagues from the spectroscopy department: Alexej Pashkin, Jayeeta Bhattacharyya, Manos Dimakis, Johannes Schmidt, Markus Fehrenbacher, Sabine Zybell, Carsten Franke, Daniel Stephan, Martin Mittendorff, Martin Teich, Leila Balaghi, Tina Tauchnitz, Jacob König-Otto, Johannes Braun, Denny Lang, Jingyue Jia, Jiajun Zhu, Xu Ming, Abhishek Singh, Rakesh Rana, Christoph Böttger, Markus Hänel, Riko Kießling, Uta Lucchesi, and Joachim Wagner for their support, the great time together and lots of laughter.

My special thanks go to Peter Michel, Wolfgang Seidel and the whole FELBE team for a great support during our beam time. I am particularly grateful for the assistance given by Oleksiy Drachenko, Erik Kampert, Mike Ozerov, Oliksey Ponomaryov, Sergei Zvyagin and the whole HLD team during our magnet time. The HLD and HZDR

workshops did a great job with the manufacturing of the magneto-PL probe. Stefan Findeisen provided great support during the construction phase.

Finally, I wish to thank my parents, family, friends and especially my husband Benjamin for their love and unconditional support throughout the ups and downs of this thesis. We've made it!

Versicherung

Die vorliegende Arbeit entstand am Helmholtz-Zentrum Dresden-Rossendorf unter wissenschaftlicher Betreuung durch Prof. Dr. Manfred Helm, Professor am Institut für Angewandte Physik der Fakultät Mathematik und Naturwissenschaften der Technischen Universität Dresden.

Hiermit versichere ich, dass ich die vorliegende Arbeit ohne unzulässige Hilfe Dritter und ohne Benutzung anderer als der angegebenen Hilfsmittel angefertigt habe; die aus fremden Quellen direkt oder indirekt übernommenen Gedanken sind als solche kenntlich gemacht. Die Arbeit wurde bisher weder im Inland noch im Ausland in gleicher oder ähnlicher Form einer anderen Prüfungsbehörde vorgelegt.

Ich erkenne die Promotionsordnung der Fakultät Mathematik und Naturwissenschaften der Technischen Universität Dresden in der aktuell gültigen Fassung vom 23.02.2011 an.

Dresden, den 11.05.2016

Faina Eßer



Bautzner Landstr. 400
01328 Dresden, Germany
Tel. +49 351 260-2880
Fax +49 351 260-12880
h.schneider@hzdr.de
<http://www.hzdr.de>